

AD-A041 268

MASSACHUSETTS INST OF TECH CAMBRIDGE ACOUSTICS AND V--ETC F/G 20/11
THE MEAN FLOW EFFECT ON THE ACOUSTIC IMPEDANCE OF A RECTANGULAR--ETC(U)
FEB 77 Y M CHANG
A/V-82464-1
N00014-75-C-0509
NL

UNCLASSIFIED

1 OF 2
ADA
041268



AD A 041 268

THE MEAN FLOW EFFECT ON THE ACOUSTIC IMPEDANCE OF A RECTANGULAR PANEL

by
Yi Mason Chang
Report No. 82464-1

(12)

February 1977

This research was carried out under the
sponsorship of the Sensor Technology Program,
Code 222, Office of Naval Research,
Contract No. N00014-75-C-0509.

Approved for public release; distribution unlimited.

ACOUSTICS AND VIBRATION LABORATORY

Massachusetts Institute of Technology
Cambridge, Massachusetts 02139



DDC FILE COPY

THE MEAN FLOW EFFECT ON THE ACOUSTIC IMPEDANCE
OF A RECTANGULAR PANEL

by

Yi Mason Chang

Report No. 82464-1

February 1977

This research was carried out under
the sponsorship of the Sensor Technology Program,
Code 222, Office of Naval Research,
Contract No. N00014-75-C-0509. *new*

Approved for public release; distribution unlimited.

Acoustics and Vibration Laboratory
Massachusetts Institute of Technology
Cambridge, Massachusetts 02139

UNCLASSIFIED

SECURITY CLASSIFICATION OF THIS PAGE (When Data Entered)

REPORT DOCUMENTATION PAGE		READ INSTRUCTIONS BEFORE COMPLETING FORM
1. REPORT NUMBER Acoustics & Vibration Lab. 82464-1	2. GOVT ACCESSION NO.	3. RECIPIENT'S CATALOG NUMBER
4. TITLE (and Subtitle) The Mean Flow Effect on the Acoustic Impedance of a Rectangular Panel.	5. TYPE OF REPORT & PERIOD COVERED Technical Rept.	
7. AUTHOR(s) Yi Mason Chang	6. PERFORMING ORG. REPORT NUMBER	
9. PERFORMING ORGANIZATION NAME AND ADDRESS Office of Naval Research	8. CONTRACT OR GRANT NUMBER(s)	
11. CONTROLLING OFFICE NAME AND ADDRESS	10. PROGRAM ELEMENT, PROJECT, TASK AREA & WORK UNIT NUMBERS	
12. REPORT DATE February 1977	13. NUMBER OF PAGES	
14. MONITORING AGENCY NAME & ADDRESS (if different from Controlling Office) 135p.	15. SECURITY CLASS. (of this report) Unclassified	
15a. DECLASSIFICATION/DOWNGRADING SCHEDULE		
16. DISTRIBUTION STATEMENT (of this Report) Approved for public release; distribution unlimited.		
17. DISTRIBUTION STATEMENT (of the abstract entered in Block 20, if different from Report) N01714-75-C-4509		
18. SUPPLEMENTARY NOTES		
19. KEY WORDS (Continue on reverse side if necessary and identify by block number) Panel Vibration Acoustic Radiation Added Mass		
20. ABSTRACT (Continue on reverse side if necessary and identify by block number) In better understanding the coupling between a vibrating panel and its surrounding acoustic medium, a precise knowledge of both the real and the imaginary parts of the radiation impedance is of critical value. (over)		

DD FORM 1 JAN 73 1473

EDITION OF 1 NOV 65 IS OBSOLETE
S/N 0102-014-6601

405028

SECURITY CLASSIFICATION OF THIS PAGE (When Data Entered)

The modal radiation impedance of a rectangular panel simply supported in an infinite baffle in the presence of an inviscid, uniform, subsonic flow is studied. The analysis is based on an expansion in normal modes of the transverse vibration displacement field of transforms. These are used to formulate the expressions for the modal radiation impedance, and the cross modal coupling impedance.

A computer program was formulated to evaluate the modal radiation impedances. A modified Chebychev quadrature served as a major ingredient. Experiments performed were compared with the analytical results. Some experiments showed larger increases in the panel radiation resistance due to flow speed than would be predicted by the present linear theory.

✓

APPROVED BY	DATE
NO	DATE
REVIEWED	DATE
REVISION/ANALYSIS DATE	DATE
DATE	DATE

11

THE MEAN FLOW EFFECT ON THE ACOUSTIC IMPEDANCE OF A
RECTANGULAR PANEL

by

Yi Mason Chang

ABSTRACT

In better understanding the coupling between a vibrating panel and its surrounding acoustic medium, a precise knowledge of both the real and the imaginary parts of the radiation impedance is of critical value.

The modal radiation impedance of a rectangular panel simply supported in an infinite baffle in the presence of an inviscid, uniform, subsonic flow is studied. The analysis is based on an expansion in normal modes of the transverse vibration displacement field of the panel and the use of the wave number frequency transforms. These are used to formulate the expressions for the modal radiation impedance, and the cross modal coupling impedance.

A computer program was formulated to evaluate the modal radiation impedances. A modified Chebychev quadrature served as a major ingredient. Experiments performed were compared with the analytical results. Some experiments showed larger increases in the panel radiation resistance due to flow speed than would be predicted by the present linear theory.

TABLE OF CONTENTS

	<u>Page</u>
Title Page	1
Abstract	2
Acknowledgement	3
Table of Contents	4
List of Tables	7
List of Figures	8
List of Symbols	10
1. Introduction	13
2. Modal Coupling Impedance	18
2.1 Modal Expansions of Panel Displacement Field and Acoustic Pressure Field at Panel Surface	19
2.2 The Acoustic Wave Equation	23
2.3 The Boundary Condition	25
2.4 The Modal Coupling Impedance	27
2.5 The Non-Dimensional Form of the Modal Coupling Impedance	33
3. Numerical Evaluation of the Modal Coupling Impedance	38
3.1 The General Approach	39
3.2 The Romberg Quadrature	41
3.3 The Chebychev Quadrature	42
3.4 The Optimum Size of the Interval Over Which the l'Hopitals's Rule Should Be Applied	46

	<u>Page</u>
3.5 The Truncation Errors	48
3.6 The Numerical Procedures	51
3.7 An Upper Bound for χ_{mn} at Large Acoustic Wave Numbers	53
3.8 The Behavior of χ_{mn}^M at Small Acoustics Wave Numbers	54
4. Experimental Methods For Modal Radiation Impedance Determination	56
4.1 Equipment and Procedures for Modal Resonant Frequency and Total Damping Measurements	57
4.2 Membrane Construction	58
4.3 The Wind Tunnel Facility	59
4.4 The Measured Modal Radiation Damping of the Membrane	61
4.5 The Measured Added Mass Surface Density	64
5. The Experimental Program For the Radiation Resistance Measurements of a Rectangular Steel Plate	67
5.1 Equipment and Procedures For the Radiation Resistance Measurements	67
5.2 Plate Construction	71
5.3 Experimentally Determined Panel Radiation Resistance	72
5.4 Discussion	79
6. Conclusions and Recommendations	83
6.1 Conclusions Regarding the Computer Program For the Radiation Impedance	83
6.2 Conclusions Regarding the Modal Virtual Mass Surface Density	83

	<u>Page</u>
6.3 Conclusions Regarding the Modal Radiation Resistance	84
6.4 Recommendations	85
Tables	87
Figures	93
References	114
Appendices	117
I The Branch Cuts on the β -Plane	117
II Numerical Procedures	119

LIST OF TABLES

		<u>Page</u>
4.1	Comparison of Measured and Calculated Changes in Loss Factors Due to Flow.	87
4.2	Digitally Computed Non-Dimensional Modal Radiation Resistance for the Membrane Modes at Their Measured Resonant Frequencies.	88
4.3	Comparison of Measured and Calculated Values of Modal Radiation Reactance χ_{mn} for the Present Membrane.	89
4.4	Comparison of Experimentally and Analytically Determined Modal Radiation Reactance χ_{mn} for Sledjeski's Membrane.	90
5.1	Reverberation Time T_R Measurements for the Reverberant Chamber Enclosing the Test Section	91
5.2	Measured Plate Loss Factors.	92

LIST OF FIGURES

		<u>Page</u>
2.1	Panel with Coordinate System.	93
2.2	Sketch of I_{mn} for Large Mode Numbers m .	94
2.3	A Typical Sketch of I_{mp} .	95
2.4	Sketchs of I_{mn} for $m = 1, 2$.	96
3.1	The Modal Radiation Resistance for the Fundamental (1,1) Mode of a Square Panel at $M = 0$.	97
3.2	The Modal Radiation Reactance for the Fundamental (1,1) Mode of a Square Panel at $M = 0$.	98
3.3	Digitally Computed Non-Dimensional Modal Radiation Reactance for a (5,1) Mode with an Aspect Ratio $R = 10.875$.	99
4.1	Experimental Setup for Modal Resonant Frequency and Damping Measurements on the Membrane.	100
4.2	The Test Section Box Inserts in the Wind Tunnel.	101
4.3	Velocity Profile.	102
4.4	The Law of the Wall.	103
4.5	Digitally Computed Non-Dimensional Modal Radiation Resistance for a (5,1) Mode with an Aspect Ratio $R = 10.875$.	104
4.6	Wave Speed Data of Sledjeski's Membrane	105
4.7	Membrane Wave Speed Data.	106
5.1	Experimental Setup for Panel Vibration and Radiation Measurements.	107
5.2	Steel Plate Construction.	108

	<u>Page</u>
5.3 Average Radiation Resistance for Resonantly Excited Plate Modes at $M = 0$.	109
5.4 Average Radiation Resistance for Resonantly Excited Plate Modes at $M = 0.23$.	110
5.5 Computed Average Radiation Resistance for Resonantly Excited Plate Modes.	111
5.6 Velocity Profiles.	112
I.1 The Branch Cuts on the β -Plane	113

LIST OF SYMBOLS

A	Area of panel, $A = \ell_1 \times \ell_3$
a	$= 1 - M\beta_1/k$
B_1, B_3	Non-dimensional wave number variables $B_1 = \beta_1 \ell_1$, $B_3 = \beta_3 \ell_1$.
\tilde{B}_1, \tilde{B}_3 , etc.	See Eq. (2.38).
c_{mn}	Fluid loaded panel wave speed for the (m,n) mode.
c	Acoustic wave speed
D	Flexural rigidity $= Eh^3/12(1-\nu^2)$
E	Young's modulus.
f_{mn}^M	Natural frequency (Hz) of the (m,n) mode. Superscripts denotes Mach number.
h	Thickness of panel.
H_n, H_q	See Eq. (2.36).
k	Acoustic wave number.
K	$= k \ell_1$
k_m, k_p	Structure modal wave number in the x_1 -direction, $k_m = m\pi/\ell_1$, $k_p = p\pi/\ell_1$.
k_n, k_q	Structure modal wave number in the x_3 -direction, $k_n = n\pi/\ell_3$, $k_q = q\pi/\ell_3$.
k_{mn}	$= (k_m^2 + k_n^2)^{1/2}$
K_m, K_p , etc.	See Eq. (2.36).
ℓ_1	Panel dimension in the direction of flow.
ℓ_3	Panel dimension perpendicular to the direction of flow.
M	Mach number, $M = U/c$.

m	Panel modal index in x_1 -direction.
m_p	Panel mass surface density.
m_{mn}^M	Added mass surface density $m_{mn}^M = \frac{\rho C}{\omega} [\chi_{mn}^M + \chi_{mn}^O].$ Superscript denotes Mach number.
n	Panel modal index in x_3 -direction.
p	Panel modal index in x_1 -direction.
P	Sound pressure field.
q	Panel modal index in x_3 -direction.
R	Panel aspect ratio $R = \ell_1/\ell_3$.
R_{ij}^M	$= \rho c A \sigma_{ij}^M$
T	Membrane tension.
T_R	Reverberation time.
t	Time variable.
U	Free stream velocity.
x_1	Distance variable in the flow direction.
x_2	Distance variable perpendicular to the panel.
x_3	Distance variable perpendicular to the flow and parallel to the panel.
\underline{x}	$\underline{x} = (x_1, x_3)$
β_1	Wave number variable in the x_1 -direction.
β_3	Wave number variable in the x_3 -direction.
$\underline{\beta}$	Wave number vector, $\underline{\beta} \equiv (\beta_1, \beta_3)$
β	$\beta \equiv \sqrt{\beta_1^2 + \beta_3^2}$

γ	$\gamma = (\beta^2 - k^2 a^2)^{1/2}$
δ^*	Boundary layer displacement thickness.
ζ	Normal vibration displacement field of the rectangular panel
η	Radiation loss factor.
η	Structural loss factor ($= \eta_T - \eta_R$)
η	Total loss factor. Defined in terms of the complex stiffness $Dk_{mn}^4 (1 + i\eta_T)$
ρ	Fluid density.
σ_{mn}^M	Modal radiation resistance for the (m,n) mode, $\sigma_{mn} = \sigma_{mnmn}$. Subscript denotes Mach number.
σ_{mnpq}^M	Real part of the radiation coupling coefficient between the (m,n) and the (p,q) mode. Superscript denotes Mach number.
χ_{mn}^M	Modal radiation reactance for the (m,n) mode, $\chi_{mn} = \chi_{mnmn}$. Superscript denotes Mach number.
χ_{mnpq}^M	Imaginary part of the modal coupling coefficient between the (m,n) and the (p,q) modes. Superscript denotes Mach number.
ψ_{mn}	Two-dimensional normal mode shape for the (m,n) mode.
ω	Radian frequency.

1. INTRODUCTION

The primary motivation for investigating the radiation impedance of a rectangular panel is to better understand the coupling between the acoustic medium and the panel. This is of fundamental importance in the analysis of such phenomena as structural vibration response to a noise field or the wall pressure fluctuations created by the turbulent boundary layer, acoustic radiation due to structural vibration, fluid loading on vibrating structures, and sound transmission through structures.

In any structural vibration problem where fluid loading is significant, such as ship hull and sonar domes, a precise knowledge of both the real and the imaginary parts of the radiation impedance is of critical value. The real part of the radiation impedance is the radiation resistance. The imaginary part of the radiation impedance is the radiation reactance. Since the radiation reactance is mostly mass-like, it is related to the quantity usually called added mass surface density.

In the case of airplanes and automobiles, the vibration of the vehicle's skin panels due to turbulent boundary layer excitation may be a

substantial source of noise in the passenger compartment as well as in the neighboring community close to the vehicle path. Currently being planned are high speed ground transportation systems, suspended by an air cushion or an electromagnetic field. These vehicles are propelled by linear turbine or electromagnetic forces. While the engine noise may not be much a problem for these vehicles, many transportation experts have foreseen the possibility that the turbulent boundary layer excited frame noise may become an annoyance of major concern.

Several studies of the radiation impedance exhibited by normal modes of a rectangular panel have been made in the past [1, 2, 3]. A complete analytical solution, including fluid loading effect, is available for the vibratory response and acoustic radiation problem associated with an infinite thin panel [4, 5]. However, the vibratory response and acoustic radiation exhibited by finite and infinite panels may differ considerably [6, 7].

Finite panel problems have sometimes been attacked without transforming the spatial variables [8, 9]. That approach is analytically complex and not well suited to including the effect of radiation into an unbounded medium. Alternatively, Davies [3]

and Leehey [2], among others [10, 11], used the wave number-frequency approach in modal analysis of panel vibration and radiation. By using the wave number-frequency transforms, the problem can be reduced immediately to algebraic form.

Experimental results [12, 13] have shown a dependence of damping upon mean flow speed which may result from increased tensioning of the test panel due to the pressure difference across the panel, or may involve an interaction of panel vibration with the flow.

In this present research, the modal radiation impedance of a rectangular panel simply supported in an infinite baffle in the presence of an inviscid, uniform, subsonic flow is of primary concern. The analysis is based on an expansion in normal modes of the transverse vibration displacement field of the panel and the use of the wave number frequency transforms. These are used to formulate the expressions for the modal radiation impedance, and the cross-modal coupling impedance.

Davies [15] studied the special case of no flow. He also attempted to estimate the value of the modal radiation impedance at small acoustic wave number. For large wave number, it is well known

that the modal radiation resistance approaches 1 and and that the modal radiation reactance, as well as the cross-modal coupling impedance, approach 0.

The solution for the radiation impedance in the intermediate wave number range involves an integral with a square root singularity in it. A few attempts have been made to solve this integral in closed form. None of them have been very satisfactory.

Thus, part of the present research endeavor is directed towards the generation of an efficient computer program for evaluating the modal radiation impedance with good accuracy. A modified Gaussian-Chebyshev quadrature serves as the major ingredient in this procedure. Several people have formulated numerical techniques to compute some special cases of the modal radiation impedance. Their results are compared with the present work. They all noted the difficulty of the numerical procedures and the large amount of computer time needed.

Most experiments performed at the Massachusetts Institute of Technology, Cambridge, tended to support the present analysis and numerical results. Some of the experiments performed by the author showed larger increases in the panel radiation resistance due to flow speed than would be predicted by the

present linear theory. This probably was due to the extremely strong panel flow interaction caused by excess panel vibration levels, and the effect of Mach number.

The presentation of the research divides itself naturally into three parts. Chapter two deals in detail with the derivation of the modal radiation impedance of a rectangular panel. Chapter three illustrates the numerical procedures formulated to solve the improper integral representing the modal radiation impedance. Chapters four and five discuss the experiments performed and the comparison between the experiments and the theory.

2. MODAL COUPLING IMPEDANCE

We consider a simply supported rectangular panel of length ℓ_1 in the direction of mean flow and of width ℓ_3 in the transverse direction inserted in a flat infinite rigid baffle (see Figure 2.1). The normal vibration displacement field of the panel is expanded in terms of the *in vacuo* normal modes, or characteristic functions, of the panel. Next, the acoustic pressure field generated at the surface of the panel due to the vibration of the plate is also expanded by the *in vacuo* normal modes of the panel. These expansions, together with the wave number-frequency transforms of the acoustic wave equation and the flow-panel boundary conditions, lead to expressions relating the modal pressures at the panel surface to the modal panel velocity.

The coefficient in these expressions are defined by improper integrals. Some of these coefficients have been evaluated by Maidanik [1] and also by Davies [3] in the special case of no flow. We will continue to refer to those discussed by Maidanik as modal radiation impedances as they are a measure of how efficiently a particular modal shape radiates when no other modes are excited. However, we also require the modal

coupling impedances connecting the vibration of one panel mode with that of other panel modes because of the panel-fluid interaction. The previously determined modal radiation impedances can obviously be obtained as special cases of the modal coupling impedances. The real parts of these coefficients are associated with a radiation damping effect on the plate response. The imaginary parts lead to a virtual mass area density, the so called added mass, to be added to the mass area density of the panel, causing a decrease in the modal resonant frequencies.

2.1 Modal Expansions of Panel Displacement Field and Acoustic Pressure Field at Panel Surface

A simply supported rectangular panel of length ℓ_1 in the direction of mean flow and of width ℓ_3 in the transverse direction is inserted in a flat infinite rigid baffle (see Figure 2.1). The acoustic field radiated into the inviscid uniform subsonic flow is considered.

Rectangular coordinates $(x_1, x_2, x_3) \equiv (\underline{x}, x_2)$ are defined, with x_2 being normal to the plate and the origin being at one corner of the plate. The flow is in the region $x_2 > 0$ and is in the positive x_1 - direction.

We can expand the normal vibration displacement field of the panel in terms of the orthonormal *in vacuo* characteristic functions of the panel

$$\psi_{mn}(\underline{x}) = (2/\sqrt{A}) \sin k_m x_1 \sin k_n x_3, \quad (2.1)$$

where $A = \ell_1 \times \ell_3$ is the area of the panel, $k_m = m\pi/\ell_1$, $k_n = n\pi/\ell_3$.

The expansion of the panel displacement field, $\zeta(\underline{x}, t)$, can be expressed in the following form

$$\zeta(\underline{x}, t) = \sum_{m,n=1}^{\infty} \zeta_{mn}(t) \psi_{mn}(\underline{x}) [H(x_1) - H(x_1 - \ell_1)] [H(x_3) - H(x_3 - \ell_3)] \quad (2.2)$$

$$\text{with } \zeta_{mn}(t) = \int_0^{\ell_3} \int_0^{\ell_1} \zeta(\underline{x}, t) \psi_{mn}(\underline{x}) d\underline{x}, \quad (2.3)$$

where $H(x)$ is the Heaviside unit step function

$$H(x) = \begin{cases} 1 & (x > 0), \\ 0 & (x < 0). \end{cases}$$

The inclusion of the Heaviside step functions is necessary, since $\zeta(\underline{x}, t)$ is zero everywhere outside the panel boundaries while $\psi_{mn}(\underline{x})$ is non-zero.

The frequency Fourier transform of the panel displacement field, $\zeta(\underline{x}, t)$, is

$$\zeta(\underline{x}, \omega) = \int_{-\infty}^{\infty} \zeta(\underline{x}, t) e^{i\omega t} dt \quad (2.4)$$

or

$$\zeta(\underline{x}, \omega) = \sum_{m,n=1}^{\infty} z_{mn}(\omega) \psi_{mn}(\underline{x}) [H(x_1) - H(x_1 - \ell_1)] [H(x_3) - H(x_3 - \ell_3)] \quad (2.4a)$$

$$\text{with } z_{mn}(\omega) = \int_{-\infty}^{\infty} \zeta_{mn}(t) e^{i\omega t} dt \quad (2.4b)$$

This gives us an $e^{-i\omega t}$ time dependence for (\underline{x}, t) . We will define $z_{mn}(\omega)$ as the modal displacement of the panel associated with the (m, n) mode. Accordingly,

$$v_{mn}(\omega) = -i\omega z_{mn}(\omega) \quad (2.5)$$

is the corresponding modal velocity of the panel. For convenience, let us define

$$\zeta_0(\underline{x}, \omega) = \sum_{m,n=1}^{\infty} z_{mn}(\omega) \psi_{mn}(\underline{x}), \quad (2.4c)$$

such that

$$\zeta(\underline{x}, \omega) = \zeta_0(\underline{x}, \omega) [H(x_1) - H(x_1 - \ell_1)] [H(x_3) - H(x_3 - \ell_3)]. \quad (2.4d)$$

The wave number Fourier transform of $\zeta(\underline{x}, \omega)$ is

$$\begin{aligned} \zeta(\underline{\beta}, \omega) &= \int_{-\infty}^{\infty} \int_{-\infty}^{\infty} \zeta(\underline{x}, \omega) e^{-i\underline{\beta} \cdot \underline{x}} d\underline{x} \\ &= \int_0^{\ell_3} \int_0^{\ell_1} \zeta_0(\underline{x}, \omega) e^{-i\underline{\beta} \cdot \underline{x}} d\underline{x} \end{aligned} \quad (2.6)$$

Especially noteworthy is the fact that while $\zeta(\underline{x}, t)$, $\zeta(\underline{x}, \omega)$, $\psi_{mn}(\underline{x})$, $\zeta_0(\underline{x}, \omega)$ and all the spatial derivatives of $\psi_{mn}(\underline{x})$ and $\zeta_0(\underline{x}, \omega)$ are continuous functions of \underline{x} over the whole \underline{x} space, the first order spatial partial derivatives of $\zeta(\underline{x}, t)$ and $\zeta(\underline{x}, \omega)$ have discontinuities along the boundaries of the panel.

Now, let us denote the acoustic pressure field by $P(x_1, x_2, x_3, t) \equiv P(\underline{x}, x_2, t)$. The frequency Fourier transform of the acoustic pressure is then

$$P(\underline{x}, x_2, \omega) = \int_{-\infty}^{\infty} P(\underline{x}, x_2, t) e^{i\omega t} dt \quad (2.7)$$

Again, after a process similar to that used in Equations (2.3) and (2.4b), we can find the modal acoustic pressure at the panel surface as

$$P_{mn}(\omega) = \int_0^{\ell_3} \int_0^{\ell_1} P(\underline{x}, 0, \omega) \psi_{mn}(\underline{x}) d\underline{x} \quad (2.8)$$

$$\text{with } P(\underline{x}, 0, \omega) = \sum_{m,n=1}^{\infty} P_{mn}(\omega) \psi_{mn}(\underline{x}) \quad (2.8a)$$

The coefficient relating to modal pressure associated with the (m, n) mode, $P_{mn}(\omega)$, to the modal velocity associated with the same mode $v_{mn}(\omega)$, is called the modal radiation impedance. The coefficient relating the modal pressure associated with the (m, n) mode, $P_{mn}(\omega)$, to the modal velocity

associated with a different mode, $v_{pq}(\omega)$, is called the modal coupling impedance.

The expressions for these coefficients will be derived in the following sections through the coupling of the acoustic wave equation with the panel-flow boundary conditions.

2.2 The Acoustic Wave Equation

If the velocity of the moving medium is U , the speed of sound c , and the corresponding Mach Number $M = U/c$, the acoustic pressure field $P(x_1, x_2, x_3, t) \equiv P(\underline{x}, x_2, t)$ satisfies the well known acoustic wave equations

$$(1 - M^2) \frac{\partial^2 P}{\partial x_1^2} + \frac{\partial^2 P}{\partial x_2^2} + \frac{\partial^2 P}{\partial x_3^2} - \frac{2M}{c} \frac{\partial^2 P}{\partial x_1 \partial t} - \frac{1}{c^2} \frac{\partial^2 P}{\partial t^2} = 0 \quad (2.9)$$

Applying the frequency Fourier transform,

$$\int_{-\infty}^{\infty} (\dots) e^{i\omega t} dt,$$

to both sides of the wave equation, we will have

$$[(1-M^2) \frac{\partial^2}{\partial x_1^2} + \frac{\partial^2}{\partial x_2^2} + \frac{\partial^2}{\partial x_3^2} + k^2 + i2kM \frac{\partial}{\partial x_1}] P(\underline{x}, x_2, \omega) = 0, \quad (2.10)$$

where $k = \omega/c$ is the acoustic wave number. Further applications of the wave number

Fourier transforms,

$$\int_{-\infty}^{\infty} \int_{-\infty}^{\infty} (\dots) e^{-i\beta_1 x_1} dx_1 e^{-i\beta_3 x_3} dx_3,$$

to both sides of the above equation lead to

$$[-(1-M^2)\beta_1^2 + \frac{\partial^2}{\partial x_2^2} - \beta_3^2 + k^2 - 2kM\beta_1] P(\underline{\beta}, x_2, \omega) = 0 \quad (2.11)$$

where $\underline{\beta} \equiv (\beta_1, \beta_3)$ and $\beta^2 \equiv \beta_1^2 + \beta_3^2$. This can be rearranged in the following form

$$[\frac{\partial^2}{\partial x_2^2} - \beta^2 + k^2 a^2] P(\underline{\beta}, x_2, \omega) = 0. \quad (2.12)$$

where $a = 1 - M\beta_1/k$.

Since $P(\underline{\beta}, x_2, \omega)$ must be bounded as x_2 approaches $+\infty$, the solution to the above equation is

$$P(\underline{\beta}, x_2, \omega) = P(\underline{\beta}, 0, \omega) e^{-(\beta^2 - k^2 a^2)^{1/2} x_2} \quad (2.13)$$

In order to have $\gamma = (\beta^2 - k^2 a^2)^{1/2}$ approach $+\infty$ as $|\beta|$ goes to $+\infty$, it is necessary to adopt $(\beta^2 - k^2 a^2)^{1/2} = -i\sqrt{k^2 a^2 - \beta^2}$ for $\beta^2 < k^2 a^2$ and $(\beta^2 - k^2 a^2)^{1/2} = \sqrt{\beta^2 - k^2 a^2}$ for $\beta^2 \geq k^2 a^2$ (see Appendix I).

Note that this agrees with our previous choice of the time dependence in the form of $e^{-i\omega t}$ (see the lines prior to the Eq. (2.4)), if we want $P(\underline{\beta}, x_2, \omega) e^{-i\omega t}$ be

a radiation propagating towards the positive x_2 -direction. Also note that it will propagate, if $\beta^2 < k^2 a^2$ and that it will not propagate, if $\beta^2 \geq k^2 a^2$. The propagating wave is associated with the radiation. The non-propagating disturbance is associated with the added mass effect. This will become clearer later.

2.3 The Boundary Condition

The boundary condition existing at the interface of the moving medium and the panel is the continuity of the normal displacement

$$\xi(\underline{x}, t) = \zeta(\underline{x}, t), \quad (2.14)$$

where $\zeta(\underline{x}, t)$ is the normal displacement of the panel and $\xi(\underline{x}, t)$ is the normal component of the displacement of the fluid particle at location \underline{x} , and at time t .

The normal component of the fluid particle velocity, $v(\underline{x}, t)$, is

$$v(\underline{x}, t) = \left(\frac{\partial}{\partial t} + Mc \frac{\partial}{\partial x_1} \right) \xi(\underline{x}, t). \quad (2.15)$$

The momentum balance equation at the interface is

$$-\frac{\partial P(\underline{x}, 0, t)}{\partial x_2} = \rho \left(\frac{\partial}{\partial t} + Mc \frac{\partial}{\partial x_1} \right) v(\underline{x}, t), \quad (2.16)$$

where $P(\underline{x}, 0, t)$ is the acoustic pressure field at the panel surface, and ρ is the density of the fluid.

Combination of the equations (2.14), (2.15), and (2.16) leads to

$$-\frac{\partial P(\underline{x}, 0, t)}{\partial x_2} = \rho \left(\frac{\partial}{\partial t} + Mc \frac{\partial}{\partial x_1} \right)^2 \zeta(\underline{x}, t) \quad (2.17)$$

The frequency Fourier transform of the above equation is

$$-\frac{\partial P(\underline{x}, 0, \omega)}{\partial x_2} = \rho \left\{ -\omega^2 - i 2Mc \omega \frac{\partial}{\partial x_1} + M^2 c^2 \frac{\partial^2}{\partial x_1^2} \right\} \zeta(\underline{x}, \omega) \quad (2.18)$$

Next let us find the Fourier transform of $g'(x)$

with

$$g(x) = f(x) H(x)$$

$$g'(x) = f'(x) H(x) + f(0) \delta(x)$$

and $\lim_{x \rightarrow \infty} f(x) = 0$

where $H(x)$ is the Heaviside unit step function, and $\delta(x) = d/dx H(x)$ is the Dirac delta function. The Fourier transform of $g(x)$ can be written in the form

$$F(g) = \int_{-\infty}^{\infty} g(x) e^{-i\alpha x} dx$$

The Fourier transform of $g'(x)$ can be shown to be

$$F(g') = i\alpha F(g), \quad (2.19)$$

since

$$\begin{aligned}
 & \int_{-\infty}^{\infty} g'(x) e^{-i\alpha x} dx \\
 &= \int_{-\infty}^{\infty} f'(x) e^{i\alpha x} dx + f(0) \\
 &= f(x) e^{-i\alpha x} \Big|_0^{\infty} + i\alpha \int_0^{\infty} f(x) e^{-i\alpha x} dx + f(0) \\
 &= -f(0) + i\alpha \int_0^{\infty} f(x) e^{-i\alpha x} dx + f(0) \\
 &= i\alpha \int_{-\infty}^{\infty} f(x) H(x) e^{-i\alpha x} dx \\
 &= i\alpha F(g)
 \end{aligned}$$

Similarly, if the wave number Fourier transforms are applied to Eq. (2.18), we will have the following

$$\frac{\partial P(\underline{\beta}, 0, \omega)}{\partial x_2} = \rho a^2 \omega^2 \zeta(\underline{\beta}, \omega) \quad (2.20)$$

2.4 The Modal Coupling Impedance

The preparations made in the previous sections will now lead us to the expressions for the modal coupling impedance and the modal radiation impedance. As we pointed out earlier, the modal radiation impedance

can be obtained as a special case of the modal coupling impedance.

Substituting the expression for $P(\underline{\beta}, x_2, \omega)$ given in Eq. (2.13) into Eq. (2.20), we obtain

$$-\gamma P(\underline{\beta}, 0, \omega) = \rho a^2 \omega^2 \zeta(\underline{\beta}, \omega) \quad (2.21)$$

$$\text{where } \gamma = (\beta^2 - k^2 a^2)^{1/2}. \quad (2.22)$$

Now we have a relation connecting the acoustic pressure field at the panel surface and the panel displacement field in the wave number-frequency space.

Now, let us transform $P(\underline{\beta}, 0, \omega)$ back to $P(\underline{x}, 0, \omega)$

$$P(\underline{x}, 0, \omega) = \frac{-1}{(2\pi)^2} \int_{-\infty}^{\infty} \int_{-\infty}^{\infty} \frac{\rho a^2 \omega^2}{\gamma} \zeta(\underline{\beta}, \omega) e^{i\underline{\beta} \cdot \underline{x}} d\underline{\beta} \quad (2.23)$$

Further substitutions from Eqs. (2.6) and (2.4c) lead us to

$$P(\underline{x}, 0, \omega) = \sum_{p,q=1}^{\infty} \frac{-\rho \omega^2}{(2\pi)^2} z_{pq}(\omega) \int_{-\infty}^{\infty} \int_{-\infty}^{\infty} s_{pq}(\underline{\beta}) e^{i\underline{\beta} \cdot \underline{x}} \frac{a^2 d\underline{\beta}}{\gamma} \quad (2.24)$$

where $s_{pq}(\underline{\beta})$ is a shape function defined by

$$s_{pq}(\underline{\beta}) = \int_0^{\ell_3} \int_0^{\ell_1} \psi_{pq}(\underline{x}) e^{-i\underline{\beta} \cdot \underline{x}} d\underline{x}. \quad (2.25)$$

Substituting Eq. (2.24) into Eq. (2.8), we will have the modal acoustic pressure at the panel surface as

$$P_{mn}(\omega) = \sum_{p,q=1}^{\infty} \frac{-i\rho\omega}{(2\pi)^2} v_{pq}(\omega) \int_{-\infty}^{\infty} \int_{-\infty}^{\infty} S_{pq}(\underline{\beta}) S_{mn}^*(\underline{\beta}) \frac{a^2 d\underline{\beta}}{\gamma} \quad (2.26)$$

where $S_{mn}^*(\underline{\beta})$ is the complex conjugate of $S_{mn}(\underline{\beta})$, and $v_{pq}(\omega)$ is the modal velocity of the panel as defined in Eq. (2.5).

Eq. (2.26) can be written in the more compact form

$$P_{mn}(\omega) = \sum_{p,q=1}^{\infty} v_{pq}(\omega) R_{mnpq}^M \quad (2.27)$$

where

$$R_{mnpq}^M = \frac{-i\rho\omega}{(2\pi)^2} \int_{-\infty}^{\infty} \int_{-\infty}^{\infty} S_{pq}(\underline{\beta}) S_{mn}^*(\underline{\beta}) \frac{a^2 d\underline{\beta}}{\gamma} \quad (2.28)$$

is the modal coupling impedance; the superscript M denotes the Mach number of the moving medium. R_{mnmn}^M is the modal radiation impedance, a special case of the modal coupling impedance.

If we non-dimensionalize the modal coupling impedance by ρc , we will obtain the quantity

$$\sigma_{mnpq}^M + i\chi_{mnpq}^M = \frac{R_{mnpq}^M}{\rho c} = \frac{-ik}{(2\pi)^2} \int_{-\infty}^{\infty} \int_{-\infty}^{\infty} S_{pq}(\underline{\beta}) S_{mn}^*(\underline{\beta}) \frac{a^2 d\underline{\beta}}{\gamma} \quad (2.29)$$

Similarly, $\sigma_{mnmn}^M + i\chi_{mnmn}^M$ is a special case of the quantity defined above.

We will call σ_{mnpq}^M and σ_{mnmn}^M the non-dimensional modal coupling resistance and radiation resistance, respectively. And we will call χ_{mnpq}^M and χ_{mnmn}^M the non-dimensional modal coupling reactance and radiation reactance, respectively.

Let us evaluate the integral defining $S_{pq}(\underline{\beta})$, Eq. (2.25), in an explicit form

$$\begin{aligned} S_{pq}(\underline{\beta}) &= \int_0^{\ell_3} \int_0^{\ell_1} \psi_{pq}(\underline{x}) e^{-i\underline{\beta} \cdot \underline{x}} d\underline{x} \\ &= \frac{2}{\sqrt{A}} \int_0^{\ell_3} \int_0^{\ell_1} \sin k_p x_1 \sin k_q x_3 e^{-i\underline{\beta} \cdot \underline{x}} d\underline{x} \\ &= \frac{2k_p k_q [-1 + (-1)^p e^{-i\beta_1 \ell_1} - 1 + (-1)^q e^{-i\beta_3 \ell_3}]}{\sqrt{A} (\beta_1^2 - k_p^2) (\beta_3^2 - k_q^2)} \end{aligned}$$

Finally, for $S_{pq}(\underline{\beta}) S_{mn}^*(\underline{\beta})$, we will have

$$\begin{aligned} S_{pq}(\underline{\beta}) S_{mn}^*(\underline{\beta}) &= \frac{4k_m k_n k_p k_q}{A} \frac{1 + (-1)^{m+p} (-1)^p e^{-i\beta_1 \ell_1} - (-1)^m e^{i\beta_1 \ell_1}}{(\beta_1^2 - k_m^2) (\beta_1^2 - k_p^2)} \cdot \\ &\quad \frac{1 + (-1)^{n+q} (-1)^q e^{-i\beta_3 \ell_3} - (-1)^n e^{i\beta_3 \ell_3}}{(\beta_3^2 - k_n^2) (\beta_3^2 - k_q^2)} \end{aligned} \quad (2.31)$$

If $(n + q)$ is an even (odd) number, $S_{pq}(\underline{\beta})$ becomes an even (odd) function of β_3 . The rest of the integrand in Eq. (2.29)

$$\frac{a^2}{\gamma} = \frac{(1 - M\beta_1/k)^2}{(\beta^2 - k^2 a^2)^{1/2}}$$

is an even function of β_3 . This leads to the conclusion that $\sigma_{mnpq}^M = \chi_{mnpq}^M = 0$, if $(n + q)$ is an odd number.

If $(m + p)$ is an even (odd) number, $S_{pq}(\underline{\beta}) S_{mn}^*(\underline{\beta})$ becomes an even (odd) function of β_3 . We note that a^2/γ is neither an even nor an odd function of β_1 . At zero Mach number, a^2/γ is an even function of β_1 . Hence $\sigma_{mnpq}^M = \chi_{mnpq}^M = 0$, if $(m + p)$ is odd, and $M = 0$. At low Mach number and high acoustic wave number, if $(m + p)$ is odd, σ_{mnpq}^M and χ_{mnpq}^M are negligibly small.

Thus, we have

1. If $(m + p)$ is even and $(n + q)$ is even,

$$\begin{aligned} \sigma_{mnpq}^M + i\chi_{mnpq}^M &= \\ &= i \frac{4k k_m k_n k_p k_q}{\pi^2 A} \int_{-\infty}^{\infty} \int_{-\infty}^{\infty} \frac{1 - (-1)^m \cos \beta_1 \ell_1}{(\beta_1^2 - k_m^2)(\beta_1^2 - k_p^2)} \frac{1 - (-1)^n \cos \beta_3 \ell_3}{(\beta_1^2 - k_n^2)(\beta_1^2 - k_q^2)} \frac{a^2 d\beta}{\gamma} \end{aligned} \quad (2.32)$$

2. If $(m + p)$ is odd, $(n + q)$ even, and $M \neq 0$,

$$\begin{aligned} \sigma_{mnpq}^M + i\chi_{mnpq}^M &= \\ &= \frac{(-1)^m 4k k_m k_n k_p k_q}{\pi^2 A} \int_{-\infty}^{\infty} \int_{-\infty}^{\infty} \frac{\sin \beta_1 \ell_1}{(\beta_1^2 - k_m^2)(\beta_1^2 - k_p^2)} \frac{1 - (-1)^n \cos \beta_3 \ell_3}{(\beta_3^2 - k_n^2)(\beta_3^2 - k_q^2)} \frac{a^2 d\beta}{\gamma} \end{aligned} \quad (2.33)$$

3. If $(m + p)$ is odd, and $M = 0$,

$$\sigma_{mnpq}^0 = \chi_{mnpq}^0 = 0 \quad (2.34)$$

4. If $(n + q)$ is odd,

$$\sigma_{mnpq}^M = \chi_{mnpq}^M = 0. \quad (2.35)$$

At Mach number, M , equal to zero, the above reduce to Davies' result (see p. 13 of Reference [15]),

$$\sigma_{mnpq}^0 + i\chi_{mnpq}^0 = \begin{cases} i \frac{16k k_m k_n k_p k_q}{\pi^2 A} \int_{-\infty}^{\infty} \int_{-\infty}^{\infty} \frac{1 - (-1)^m \cos \beta_1 \ell_1}{(\beta_1^2 - k_m^2)(\beta_1^2 - k_p^2)} \frac{1 - (-1)^n \cos \beta_3 \ell_3}{(\beta_1^2 - k_n^2)(\beta_1^2 - k_q^2)} \frac{d\beta}{\gamma} , \\ 0, \text{ otherwise} \end{cases}$$

If $m + p = \text{even}$ and $n + q = \text{even}$,

We note that the only singularity in the integrand of Eqs. (2.32), (2.33) and (2.32a) is the square root singularity. The expression

$$\gamma = (\beta^2 - k^2 a^2)^{1/2} = 0$$

represents an ellipse which can be better described by the equivalent form

$$\left(\frac{\beta_1 + \frac{Mk}{1-M^2}}{\frac{k}{1-M^2}} \right)^2 + \left(\frac{\frac{\beta_3}{k}}{\frac{1}{\sqrt{1-M^2}}} \right)^2 = 0$$

The ellipse is centered at

$$\left(-\frac{Mk}{1-M^2}, 0 \right),$$

with $\frac{k}{1-M^2}$ being the semimajor axis, and $\frac{k}{\sqrt{1-M^2}}$ being the semiminor axis. This ellipse becomes a circle of radius k centered at the origin when $M = 0$.

2.5 The Non-Dimensional Form of the Modal Coupling Impedance

To reduce the number of independent variables involved and to facilitate an efficient numerical computation procedure, we non-dimensionalize the expressions for $\sigma_{mnpq}^M + i \chi_{mnpq}^M$, which itself is a non-dimensional quantity. We will first make the panel dimensions and the wave number quantities non-dimensional using ℓ_1 , the dimension of the panel in the flow direction. Accordingly,

$$R = \ell_1 / \ell_3$$

$$K = k \ell_1$$

$$B_1 = \beta_1 \ell_1 \quad B_3 = \beta_3 \ell_1 = \beta_3 \ell_3 R$$

$$B^2 = B_1^2 + B_3^2 = \beta^2 \ell_1^2$$

$$K_m = k_m \ell_1 = m\pi \quad K_n = k_n \ell_1 = n\pi R$$

$$K_p = k_p \ell_1 = p\pi \quad K_q = k_q \ell_1 = q\pi R$$

$$K_{mn}^2 = K_m^2 + K_n^2 = k_{mn}^2 \ell_1^2 = (k_m^2 + k_n^2) \ell_1^2 = (m^2 + n^2 R^2) \pi^2$$

$$H_n = K_n/R = n\pi = k_n \ell_1/R = k_n \ell_3$$

$$H_q = K_q/R = q\pi = k_q \ell_1/R = k_q \ell_3$$

$$a = 1 - MB_1/K = 1 - M\beta_1/k \quad (2.36)$$

Then we have

$$\sigma_{mnpq}^M + i\chi_{mnpq}^M = G' \int_{-\infty}^{\infty} \int_{-\infty}^{\infty} I'_{mp} I'_{nq} \frac{a^2 dB}{(B^2 - K^2 a^2)^{1/2}} \quad (2.37)$$

where $G' = i4R^3 K_{mnpq} \pi^2$

$$I'_{mp} = \frac{1 - (-1)^m \cos B_1}{(B_1^2 - K_m^2) (B_1^2 - K_p^2)}$$

$$I'_{nq} = \frac{1 - (-1)^n \cos (B_3/R)}{(B_3^2 - K_n^2) (B_3^2 - K_q^2)}$$

From this expression, we can see that to determine the non-dimensional modal radiation impedance, we need only to know the modal index numbers, m, n, p, q , the panel aspect ratio, R , the non-dimensional acoustic wave number, K , and the Mach number, M , a total of seven parameters.

It is desirable to make the following transformation of variables in order to make the expressions for $\sigma_{mnpq}^M + i\chi_{mnpq}^M$ more adaptable to the

numerical techniques discussed in the next chapter. In the transformation, we have

$$\begin{aligned}
 \tilde{K} &= K/\sqrt{1-M^2} \\
 \tilde{B}_1 &= \sqrt{1-M^2} B_1 + KM/\sqrt{1-M^2} \\
 \tilde{B}_3 &= B_3 \\
 \tilde{B}^2 &= \tilde{B}_1^2 + \tilde{B}_3^2 \\
 \theta &= \tan^{-1} (\tilde{B}_3/\tilde{B}_1) \\
 x &= \tilde{B}/\tilde{K} \\
 y &= \tilde{K}/\tilde{B} \\
 \tilde{a} &= 1 - M \tilde{B}_1/\tilde{K} = (1-M^2)a
 \end{aligned} \tag{2.38}$$

The equations in the new variables are

$$\sigma_{mnpq}^M = G \int_0^1 \int_0^\pi I_{mp} I_{nq} \frac{\tilde{a}^2 x dx d\theta}{\sqrt{1-x^2}} \tag{2.39}$$

$$\chi_{mnpq}^M = G \int_0^1 \int_0^\pi I_{mp} I_{nq} \frac{\tilde{a}^2 dy d\theta}{y^2 \sqrt{1-y^2}} \tag{2.40}$$

where

$$G = \frac{8 \tilde{K}^2 mnpq \pi^2}{R(1-M^2)^2} = \frac{8 K^2 mnpq \pi^2}{R(1-M^2)^3} \tag{2.41}$$

$$I_{mn} = I'_{mp} \quad (\text{see Eq. (2.37)})$$

$$I_{nq} = I'_{nq} R^4 = \frac{1 - (-1)^n \cos(B_3/R)}{[(B_3/R)^2 - H_n^2] [(B_3/R)^2 - H_q^2]}$$

For future reference, the following equality has been established

$$B^2 - (Ka)^2 = \tilde{B}^2 - \tilde{K}^2.$$

Typical values of the function

$$I_{mp} = \frac{1 - (-1)^m \cos B_1}{(B_1^2 - K_m^2)(B_1^2 - K_p^2)}$$

and shown in Figures 2.2 and 2.3. The function is such that

$$\int_0^\infty I_{mp} dB_1 = \frac{\pi}{4 K_m^2} \delta_{mp} \quad (2.42a)$$

$$\int_0^\infty I_{nq} dB_3 = \frac{R \pi}{4 H_n^2} \delta_{nq} \quad (2.42b)$$

Although the function I_{mm} has essentially similar characteristics for all large integers m , its character is somewhat modified when m is small. The modifications are particularly marked for $m = 1$ and 2 ; graphs of the functions for these cases are given in Figure 2.4. For

$m = 1$, the major peaks are merged into a single broad peak centered on $B_1 = 0$. For $m = 2$, there are no minor peaks between the major peaks.

To simplify matters, we will abbreviate σ_{mnmn}^M , χ_{mnmn}^M and R_{mnmp}^M by σ_{mn}^M , χ_{mn}^M and R_{mn}^M , and we will omit the superscript M , if $M = 0$, so long as no confusion will result.

3. NUMERICAL EVALUATION OF THE MODAL
COUPLING IMPEDANCE

Now that we have found the integral expressions for the modal coupling impedance, it would be desirable to evaluate the integral in a closed analytic form. Unfortunately, many such attempts have been made and no satisfactory results have been found.

Several investigators have tried to estimate the value of the modal radiation impedance at small acoustic wave numbers for no flow. For large wave numbers it is well known that the non-dimensional modal radiation resistance approaches 1, while the non-dimensional modal radiation reactance approaches 0. However, many applications require the knowledge of the modal radiation impedance in the intermediate wave number range and with flow.

Hence, this chapter is directed towards the development of an efficient computer program to evaluate numerically the modal radiation impedance with sufficient accuracy. A modified Gaussian-Chebyshev quadrature serves as the major ingredient in this numerical procedure. A number of people have worked on some of the special cases. Their results will be compared with the present work.

3.1 The General Approach

The difficulties encountered in evaluating the integral in Eq. (2.37) are primarily due to the following:

1. The integrand has a square root singularity in the denominator.

2. The integrand is a very complex function. Its magnitude fluctuates so rapidly that, to describe the integrand satisfactorily, we need to sample at a large number of abscissas, and at each abscissa we need to do a good many operations to evaluate the integrand.

3. The integral is an improper one with integration limits being $-\infty$ and $+\infty$, that is the whole two dimensional wave number space, β .

In view of these problems, we will formulate a Chebychev quadrature to handle the square root singularity. A comparison between the equations (2.37) and (2.39) reveals that we need to apply the Chebycher quadrature only once in polar coordinates instead of twice as required in rectangular coordinates. We will therefore base our numerical analysis on the form expressed in polar coordinates, Eqs. (2.39) and (2.40).

First, we use a Romberg quadrature to compute the inner integral in the θ -dimension. Due to

the complexity of the integrand, we adopt a quadrature which employs reusable abscissas. That is, each time the order of the quadrature increases, or, equivalently, when the number of abscissas increases, the abscissas used in the previous iteration are reused in the new, higher order quadrature. Romberg quadrature is one which employs reusable abscissas and converges very rapidly as the order of the quadrature increases.

Second, we will formulate a Chebychev quadrature which employs reusable abscissas to handle the square root singularity in the outer integral in x or in y . It should be noted that the Gaussian formulas (which include the Chebychev quadrature) achieve higher accuracy with the use of fewer abscissas than other numerical methods, say, the Newton-Cotes method. The arrangement of this Chebychev quadrature to employ reusable abscissas provides further savings in the amount of computation time required.

Third, in computing the non-dimensional modal radiation reactance, the integration limits are from 0 to 1 in y . A small y corresponds to a large \tilde{B} . Thus, when y is small, a large number of computations are involved in the Romberg quadrature in the θ -dimension. We will determine a upper bound for the truncation error

$$E = \int_0^1 \int_0^1 I_{mp} I_{nq} \frac{\tilde{a}^2 d\theta dy}{y^2 \sqrt{1-y^2}}.$$

This will enable us to set the integrand equal to zero when y is less than some small number while retaining satisfactory accuracy.

3.2 The Romberg Quadrature

The standard Romberg quadrature uses only the trapezoidal rule over subintervals repeatedly cut in half until two successive extrapolated estimates differ by less than a specified error allowance. It has been proved that Romberg quadrature will converge rapidly to the true value of the integral because it is a quadrature based upon the trapezoidal rule (see p. 121 of Reference [19]).

This present version of Romberg quadrature was derived from a Fortran II version dating from about 1966, written by Professor D. G. Anderson of the Harvard Computing Center. It is somewhat different from the standard version of the Romberg quadrature, and is based upon the following facts:

1. As the size of the subinterval, h , decreases, both the trapezoidal and the midpoint rules have errors proportional to h^2 .

2. For small h the midpoint and the trapezoidal rule produce errors of opposite signs. For the midpoint rule,

$$\int_0^h F(x)dx = hF(h/2) + h^2/24 F''(\xi)$$

where $\xi \in [0, h]$. For the trapezoidal rule,

$$\int_0^h F(x)dx = h/2 [F(0) + F(h)] - h^2/12 F''(\xi)$$

where $\xi \in [0, h]$.

Thus, if we have estimates of the integral for a sequence of decreasing values of h , we can extrapolate the estimates to a very small subinterval size. Furthermore, the difference between the two estimates gives a better error bound, since the errors are of opposite signs, and are of the same order of magnitude. Note that the standard Romberg quadrature is based upon the trapezoidal rule alone. Its error bound is the difference between two estimates of successive orders. With a better estimate of the error bound, our Romberg quadrature will converge sooner than the standard version.

3.3 The Chebychev Quadrature

The standard Chebychev quadrature is expressed in the following algorithm:

$$\int_{-1}^1 \frac{f(x)}{\sqrt{1-x^2}} dx = \frac{\pi}{n} \sum_{j=1}^n f(a_j) + E' \quad (3.1)$$

where $a_j = \cos \frac{2j-1}{2n} \pi$, $j = 1, 2, 3, \dots, n$,

$$E' = \frac{2\pi}{2^{2n}(2n)!} f^{(2n)}(\xi),$$

$$\xi \in [-1, 1],$$

and n is the order of the quadrature and the number of abscissas used. In this section we will discuss only the necessary and important modifications to make it a more efficient and powerful quadrature. For a detailed discussion on the standard Chebychev quadrature refer to p. 99 of Ralston's book [19].

First, we want a quadrature for an integral with integration limits from 0 to 1 instead of from -1 to 1. Note the fact that $a_j = -a_{n-j+1}$. Since the integration limit is only from 0 to 1, we can always imagine an extension of $f(x)$ from -1 to 0 such that $f(x)$ is an even function of x , that is $f(x) = f(-x)$. Then we will have

$$2 \int_0^1 \frac{f(x)}{\sqrt{1-x^2}} dx = \int_{-1}^1 \frac{f(x)}{\sqrt{1-x^2}} dx$$

$$= \begin{cases} \frac{\pi}{n} \left\{ 2 \sum_{j=1}^{\frac{n-1}{2}} f(a_j) + f(0) \right\} + E' & n = \text{odd} \\ \frac{\pi}{n} \left\{ 2 \sum_{j=1}^{\frac{n}{2}} f(a_j) \right\} + E' & n = \text{even}, \end{cases}$$

or

$$\int_0^1 \frac{f(x)}{\sqrt{1-x^2}} dx = \begin{cases} \frac{\pi}{n} \left\{ \sum_{j=1}^{\frac{n-1}{2}} f(a_j) + \frac{f(0)}{2} \right\} + \frac{E'}{2} & n = \text{odd} \\ \frac{\pi}{n} \sum_{j=1}^{\frac{n}{2}} f(a_j) + \frac{E'}{2} & n = \text{even} \end{cases} \quad (3.2)$$

Second, we know that the Chebychev quadrature does not have reusable abscissas. That is, if we increment the order of the quadrature n arbitrarily, we will have a completely different set of abscissas, a_j 's. The effort required to compute the functional values at these abscissas accounts for most of the computation time spent, especially if $f(x)$ is a very complex function. Thus, it is desirable to find a way to increment n such that the abscissas remain in the set of abscissas for the next n .

After a careful investigation, we have found such a way. That is, if we increment n by the following sequence,

$$n = 3^1, 3^2, 3^3, \dots, 3^{m-1}, 3^m, \dots, \text{etc.},$$

The abscissas for $n = 3^{m-1}$ remain the abscissas for $n = 3^m$, and we have only $2 \cdot 3^{m-1}$ out of the 3^m abscissas which are new. These $2 \cdot 3^{m-1}$ new abscissas are $b_i = \cos i/(2 \cdot 3^m)$ where $i = 1, 5, 7, 11, 13, \dots, (3^m - 2)$.

The resulting algorithm is

$$\int_0^1 \frac{f(x)}{\sqrt{1-x^2}} dx = \frac{\pi}{n} \cdot \text{SUM}(n) + \frac{f(0)}{2} + E; \quad (3.3)$$

$$n = 3, 9, 27, 81, \dots, 3^m, 3^{m+1}, \dots$$

$$\text{where } \text{SUM}(n) = \text{SUM}(n/3) + \sum_{i=1,5,7,11,13,\dots}^{n-2} f(b_i) \quad (3.4)$$

$$E = \frac{\pi}{2^{2n} (2n)!} f^{(2n)}(\xi), \quad (3.5)$$

$$\xi \in [0, 1].$$

This is an improved and more efficient version of Chebychev quadrature, especially, if $f(x)$ is a complicated transcendental function.

3.4 The Optimum Size of the Interval Over Which l'Hopital's Rule Should Be Applied

In evaluating the values of I_{mp} and I_{nq} (see Eq. (2.37) and Eq. (2.41)), there are places where I_{mp} and I_{nq} become indeterminate and l'Hopital's rule must be applied. In a digital computer, due to the finite number of significant digits available and the unavoidable roundoff errors we shall instead use a Taylor series expansion over an interval centered around the point of indeterminacy. A Taylor series expansion of more terms will be valid over a wider interval than a Taylor series expansion of fewer terms. However, for a prescribed error tolerance, it is not desirable to have the computer evaluate more terms than necessary in a Taylor series expansion. Neither is it desirable to apply the Taylor series expansion over too wide an interval such that unnecessary loss in accuracy is incurred.

Suppose the function we want to evaluate is $f(x)$, which is indeterminate at x_0 . Let $[x_0 - \Delta x, x_0 + \Delta x]$ be the interval over which the computer is to use the Taylor series expansion instead

of the formal expression for $f(x)$. Stored in a digital computer, there are scientific subroutines available to calculate the $f(x)$ in its formal expression. Due to practical limitations, these subroutines are not perfect. In many cases, the error bounds of these scientific subroutines, ϵ , are published by the software supplier. For example, $\epsilon = 1 \times 10^{-7}$ for $\sin x$ and $\cos x$ with $|x| \leq 3\pi$ in the IBM 370 computer.

Based on the knowledge of ϵ , we can find the error bound, $E(\epsilon)$, for the function $f(x)$. There is also the error bound, $E(T)$, due to the use of the Taylor's series expansion. We therefore recognize the following:

1. $E(\epsilon)$ is increasing with $|\Delta x|$ decreasing.
2. $E(T)$ is increasing with $|\Delta x|$ increasing.
3. The optimum choice of $|\Delta x|$ is the one with $E(\epsilon) = E(T)$, for the prescribed precision requirement.

In the present study, we found that only the first term of the Taylor series expansion was needed to compute I_{mp} and I_{nq} with errors less than 3×10^{-4} of the true value. A typical value of $\Delta x/x_0$ is 2.55×10^{-4} .

3.5 The Truncation Errors

The integral expressed in Eq. (2.37) is an improper one with integration limits intending to $\pm \infty$. After the integral is transformed into the polar coordinates as expressed in Eq. (2.40), a small y still corresponds to a very large \tilde{B} . When \tilde{B} is large, a large number of computations will be required in the Romberg quadrature over the θ -dimension. However, the integrand is diminishing rapidly as \tilde{B} increases. This prompted us to do the following analysis to find an upper bound for the quantity

$$\int_0^\epsilon \int_0^\pi I_{mp} I_{nq} \frac{\tilde{a}^2 d\theta dy}{y^2 \sqrt{1-y}} \quad (3.6)$$

which is the truncation error introduced if we integrate in the y -variable from ϵ to 1 rather than from 0 to 1.

We require ϵ be small enough so that

$$\tilde{B} \gg \sqrt{2}K_{mn}, \quad \tilde{B} \gg \sqrt{2}K_{pq} \quad \text{and} \quad \tilde{B} \gg \sqrt{2}K \quad (3.7)$$

With y being held constant, let us study the quantities

$$E'_{mnpq} = \int_0^{\frac{\pi}{4}} I_{mp} I_{nq} \tilde{a}^2 d\theta + \int_{\frac{3\pi}{4}}^{\pi} I_{mp} I_{nq} \tilde{a}^2 d\theta \quad (3.8a)$$

$$\text{and } E_{mnpq}'' = \int_{\frac{\pi}{4}}^{\frac{3\pi}{4}} I_{mp} I_{nq} \tilde{a}^2 d\theta. \quad (3.8b)$$

When $\theta = \pi/4$, we have $\tilde{B}_1 = \tilde{B}_3$. When $\theta = 3\pi/4$, we have $\tilde{B}_1 = -\tilde{B}_3$ (see Eq. (2.38)).

In the region $0 \leq \theta \leq \pi/4$,

$$d\theta = d \tan^{-1} \left(\frac{\tilde{B}_3}{\tilde{B}_1} \right) = \frac{d \left(\frac{\tilde{B}_3}{\tilde{B}_1} \right)}{1 + \left(\frac{\tilde{B}_3}{\tilde{B}_1} \right)^2} \leq d \left(\frac{\tilde{B}_3}{\tilde{B}_1} \right) \quad (3.9)$$

$$\text{Since } \frac{\tilde{B}}{\sqrt{2}} \leq \tilde{B}_1 \leq \tilde{B}, \quad (3.10)$$

$$\text{we have } d\theta \leq \frac{\sqrt{2}}{\tilde{B}} d\tilde{B}_3 = \frac{\sqrt{2}}{\tilde{B}} dB_3 \quad \text{in } 0 \leq \theta \leq \frac{\pi}{4}. \quad (3.11)$$

$$\text{Thus, } \int_0^{\frac{\pi}{4}} I_{mp} I_{nq} \tilde{a}^2 d\theta \leq \int_0^{\tilde{B}/\sqrt{2}} I_{mp} I_{nq} \tilde{a}^2 \frac{\sqrt{2}}{\tilde{B}} dB_3.$$

Here both y and \tilde{B} are still kept constant and $y = \tilde{K}/\tilde{B}$.

Similarly we obtain, in the region $3\pi/4 \leq \theta \leq \pi$,

$$\int_{\frac{3\pi}{4}}^{\pi} I_{mp} I_{nq} \tilde{a}^2 d\theta \leq \int_0^{\tilde{B}/\sqrt{2}} I_{mp} I_{nq} \tilde{a}^2 \frac{\sqrt{2}}{\tilde{B}} dB_3$$

From inequalities (3.7) and (3.10) we have, in these regions, $\tilde{B}_1 \gg K_m$ or K_p and $\tilde{B}_1 \gg K$.

$$\text{Since } \tilde{B}_1 = \sqrt{1-M^2} B_1 + M\tilde{K}, \quad (\text{Eq. (2.38)})$$

$$\text{we get } \tilde{B}_1 \simeq \sqrt{1-M^2} B_1,$$

or
$$B_1 = \frac{\tilde{B}_1}{\sqrt{1-M^2}} = \frac{\tilde{B}}{\sqrt{2(1-M^2)}}$$

and $B_1 \gg K_m \text{ or } K_p.$

Now we have

$$I_{mp} = \frac{1 - (-1)^m \cos B_1}{(B_1^2 - K_m^2)(B_1^2 - K_p^2)} \approx \frac{1 - (-1)^m \cos B_1}{B_1^4}$$

$$\leq \frac{8(1-M^2)^2}{\tilde{B}^4}$$

The above preparations will enable us to find an upper bound for the quantity in (3.6). The following is an example where $m=p$ and $n=q$.

$$E'_{mnmn} \leq 2 \int_0^{\tilde{B}} I_{mm} I_{nn} \tilde{a}^2 \frac{\sqrt{2}}{\tilde{B}} dB_3$$

$$\leq \frac{16\sqrt{2}(1-M^2)^2}{\tilde{B}^5} \left[1 + M^2 \frac{\tilde{B}^2}{K^2} \right] \int_0^\infty I_{nn} dB_3$$

$$\leq \frac{16\sqrt{2}(1-M^2)^2}{\tilde{B}^5} \left[1 + M^2 \frac{\tilde{B}^2}{K^2} \right] \frac{R\pi}{4H_n^2} \quad (\text{See Eq. (2.42b)})$$

$$\therefore E'_{mnmn} \leq b_1 \frac{Y^5}{\tilde{K}^5} [1 + M^2 Y^{-2}]$$

where $b_1 = 4\sqrt{2} (1-M^2)^2 R\pi H_n^{-2}.$

A similar process with the roles of B_1 and B_3 interchanged will lead us to

$$E''_{mnmn} \leq b_2 \frac{y^5}{\tilde{K}^5} [1 + 1/2 M^2 y^{-2}]$$

where $b_2 = 4\sqrt{2} R^4 \pi k_m^{-2}$

Finally, the quantity in (3.6) becomes

$$\begin{aligned} & \int_0^\epsilon (E'_{mnmn} + E''_{mnmn}) \frac{dy}{y^2 \sqrt{1-y^2}} \\ & \leq \int_0^\epsilon \frac{1}{\tilde{K}^5} [(b_1+b_2)y^3 + M^2(b_1+b_2/2)y] dy \\ & \leq \frac{1}{\tilde{K}^5} [(b_1+b_2) \frac{\epsilon^4}{4} + M^2(b_1 + b_2/2) \epsilon^2/2] \end{aligned}$$

3.6 The Numerical Procedures

A copy of the resulting numerical algorithm formulated by the author is included in Appendix II. This algorithm was formulated to compute the quantities expressed in Eqs. (2.32), (2.34) and (2.35), but not the ones expressed in Eq. (2.33). It has been used on a model M70 Interdata minicomputer with a memory of 24 Kilobytes. The same algorithm is readily used on the model 1130 and model 370 IBM computers.

Wallace [18] used a two-dimensional Gauss-type quadrature formula to evaluate numerically

the non-dimensional modal radiation resistance without flow, that is σ_{mn} (his S_{mn}). Our computer program gives data which coincide with his graphical data. To facilitate comparison we note that his b/a is the inverse of our aspect ratio, i.e. $1/R$, and that his γ equals K/K_{mn} in our notation.

Sandman [20] used an approximate formulation and obtained qualitatively similar results. It is noted that his estimates on σ_{11} and χ_{11} are 15 ~ 18% higher than both Wallace's and our data (see Figure 3.1). It can be shown that Sandman's formula is related to our formula in the following form

$$\sigma_{mnpq} = \frac{2}{\lambda_{\infty} \sigma \pi} Z_{mnpq}.$$

where all the quantities on the right hand side are those defined by Sandman.

3.7 An Upper Bound χ_{mn} at Large Acoustic Wave Numbers

To check the accuracy of our computer algorithm in computing χ_{mn} , we would like to find an upper bound for χ_{mn} at large K . We can use the same process demonstrated in finding an upper bound for the quantity

$$\int_0^\epsilon \int_0^\pi I_{mm} I_{nn} \frac{dy d\theta}{y^2 \sqrt{1-y^2}} \quad (3.12)$$

(See Section 3.5) by simply extending ϵ to 1.
We assumed that

$$K \gg \sqrt{2} K_{mn} \quad (3.13)$$

Since $B > K$, we have

$$B \gg \sqrt{2} K_{mn} \quad (3.14)$$

This is the first inequality assumed previously in (3.7). Note that $M = 0$ in the present case. Thus, the third inequality in (3.7) is not needed here (see lines following (3.11)). Now, we have

$$\begin{aligned} & \int_0^1 \int_0^\pi I_{mm} I_{nn} \frac{d\theta dy}{y^2 \sqrt{1-y^2}} \\ & \leq \sqrt{2} R (H_n^{-2} + R^3 K_m^{-2}) K^{-5} \end{aligned} \quad (3.15)$$

From Eq. (2.40) the corresponding upper bound for χ_{mn} is then

$$\chi_{mn} \leq 8\sqrt{2} mnpq \pi^3 (H_n^{-2} + R^3 K_m^{-2}) K^{-3} \quad (3.16)$$

Figure 3.3 shows digitally computed radiation reactances for a case where $m = 5$, $n = 1$, $R = 10.875$. Figure 3.3 also includes a straight line representing the upper bound found in (3.16). This upper bound appears to be a conservative one. The computed values of χ_{mn} tend to approach zero proportional to K^{-5} instead of K^{-3} .

3.8 The Behavior of χ_{mn}^M at Small Acoustic Wave Numbers

In Figure 3.3 the computed values of radiation reactances χ_{mn}^M and χ_{mn}^O approaches two extremes, ∞ and 0, respectively at small acoustic wave numbers. This behavior needs some attention.

Following Davies [15], and earlier Kraichnan [10] (his Eq. (5.5)), delta function approximations can be used in Eq. (2.37) in the form

$$I_{mm}' = \frac{\pi}{4K_m^2} [\delta(B_1 + K_m) + \delta(B_1 - K_m)] \quad (3.17)$$

$$I_{nn}' = \frac{\pi}{4H_m^2 R^3} [\delta(B_3 + K_n) + \delta(B_3 - K_n)] \quad (3.18)$$

Since $a = 1 - MB_1/K$, we have

$$\lim_{K \rightarrow 0} K^2 a^2 = \lim_{K \rightarrow 0} (K^2 + M^2 B_1^2 - 2MB_1 K) = M^2 B_1^2. \quad (3.19)$$

$$\text{and} \quad a^2 = 1 + \frac{M^2 B_1^2}{K^2} - 2M \frac{B_1}{K} \quad (3.20)$$

Substituting these quantities and approximations into

Eq. (2.37) (3.21)

$$\chi_{mn}^M = \text{Imaginary part of } \left[G' \int_{-\infty}^{\infty} \int_{-\infty}^{\infty} I'_{mn} I'_{mn} \frac{a^2 dB}{(B^2 - K^2 a^2)^{1/2}} \right]$$

we have

$$\lim_{K \rightarrow 0} \chi_{mn}^M = \frac{K[1 + M^2 K_m^2 / K^2]}{[K_{mn}^2 - M^2 K_m^2]^{1/2}} \quad (3.22)$$

$$= \begin{cases} K/K_{mn} & \text{if } M = 0 \end{cases} \quad (3.23)$$

$$= \begin{cases} \frac{M^2 K_m^2}{K(K_{mn}^2 - M^2 K_m^2)^{1/2}} & \text{if } M \neq 0 \end{cases} \quad (3.24)$$

Eq. (3.23) is identical to Davies' Eq. (3.20) in [15]. These equations confirm the numerically computed data in Figure 3.3. For the case where both K and M approach 0, the limit obviously depends on the relative rate of which they approach 0, and Eq. (3.22) shall be applied.

4. EXPERIMENTAL METHODS FOR MODAL RADIATION IMPEDANCE DETERMINATION

On a panel with widely separated modes we can determine experimentally the resonant frequency and the amount of damping for a specific mode. From the modal resonant frequency and the modal wave number, we can calculate the modal wave speed.

If we do the above experiments in a vacuum, we will find the *in vacuo* modal wave speed and the *in vacuo* modal damping. If we repeat the same experiment in fluid, we will find the modal wave speed decreased and the modal damping increased. The difference in modal wave speed is due to the added virtual mass. The difference in modal damping is due to the added radiation damping.

In this chapter, we are also interested in another mechanism which affects both the modal resonant frequencies and the modal damping values. That is the effect of the flow.

The author performed some experiments in a wind tunnel with one side of the panel subject to a flow at Mach numbers 0 and 0.23. These experimental results will be compared with analytic calculations.

4.1 Equipment and Procedures for Modal Resonant Frequency and Total Damping Measurements

The experimental setup used in the measurements of modal resonant frequencies and total damping values is shown in Figure 4.1. An acoustic driver with a small opening of 1.1 cm diameter was used to drive the membrane with a pure tone. The modal KD-38 Fotonic Sensor, manufactured by Mechanical Technology, Inc., served as a non-contact optical displacement gauge. Since the fixed Fotonic Sensor was positioned at the center of the membrane, only odd number modes were observed.

The exact nature of the excitation plays a critical part in these measurements. It is important to maximize the response of the mode to be measured while minimizing the response of all other modes. The first step in this process is to drive the membrane at the resonant frequency of the mode under consideration. The second step is to insure that the excitation is most nearly spatially matched with the desired mode and least well matched with the other modes. Therefore, the small acoustic driver was placed at one of the antinodes of the desired mode.

With this arrangement we slowly swept the sinewave oscillator driving the sound source over the

frequency range and observe the displacement amplitude with the Fotonic optical sensor. We recorded the frequency at which the peak value was reached. The Chladni pattern was observed by using a light dusting of fine sand to identify nodes.

Once the mode and its resonant frequency were found, the small acoustic driver was shut off so that the graphic level recorder would observe and record the decay rate. The reverberation time T_R is the time needed for the level of a transient signal to decay 60 dB. Its relation with the loss factor η_T is $T_R = 2.2/f\eta_T$. This η_T is the total loss factor which is the sum of the structural loss factor η_S and the radiation loss factor η_R .

In all measurements the displacement amplitude of membrane vibration was less than 0.025 mm which was about 1/8 of the membrane thickness.

4.2 Membrane Construction

The membrane was previously constructed by another investigator (see Martin and Leehey [21]) from a 71 cm diameter mylar bass drum head uniformly tensioned on a bass drum frame. A 1.9 cm thick plywood backing plate with a rectangular cut-out was cemented to one side of the drum head. The cut-out

was lined with plexiglas to sharply define the boundary for the rectangular membrane which had the following physical characteristics:

- a. Surface dimensions: $\ell_1 = 55.3 \text{ cm}$,
 $\ell_3 = 5.08 \text{ cm}$.
- b. Aspect ratio: $R = 10.875$.
- c. Thickness: $h = 0.2032 \text{ mm}$.
- d. Surface density: $m_p = 0.286 \text{ Kg/m}^2$.
(This is a slight change from the value reported by Martin and Leehey).

4.3 The Wind Tunnel Facility

The experiments were carried out using the facilities and equipment of the Acoustic and Vibration Laboratory at M.I.T. The measurements on the mean flow effect of the modal radiation impedance were made in the low-noise, low-turbulence wind tunnel. The basic characteristics of this wind tunnel have been described by Hanson [22]. For the present experimental program it was desirable to have a higher Mach number than was available with the original wind tunnel design, which had a $0.38 \text{ m} \times 0.38 \text{ m}$ square duct cross-section.

We constructed two box inserts, designated A & B in Figure 4.2, which brought the maximum available

Mach number up to 0.23. These inserts were made from masonite sheets supported by pine frames. Damping material was attached to the inner surfaces. The hollow spaces in the boxes were filled with fiberglass blankets.

Box A when inserted in the upstream square duct, formed a contraction region for the flow. The dimensions of the cross-section at its exhaust were 0.38 m x 0.17 m. The test membrane became part of the top wall of the duct, and the surface of the membrane was carefully positioned to be flush with the rest of the duct wall. The membrane was oriented to have its longitudinal dimension parallel to the flow direction. The bottom wall of the test section was removed to form an open jet 0.91 m long until it entered the collector. The collector was a 5° expansion region formed by Box B inserted in the downstream square duct.

A wire screen of 6.4 mm x 6.4 mm mesh size was placed at the exhaust end of the contraction. In the expansion region, we cut three pressure releasing vents 0.23 m downstream from the collector front end. Each vent had a size of 7.63 cm x 3.81 cm. The vents were stuffed with polyurethane foam to retard whistling or other acoustic resonances. It was found that 7 cm of the wire screen protruding into the flow, together with the vents, effectively damped out the noise created by the pulsating flow in the test section.

With the tunnel configuration as described above, tests were performed at both $M = 0$, and $M = 0.23$. Mach number $M = 0.23$ corresponds to a flow speed of 79 m/sec. Using a 1 mm diameter total head tube, mean flow velocity profiles were measured. A typical mean flow velocity profile is shown in Figure 4.3. From these velocity profiles values of displacement thickness δ^* and momentum thickness θ were computed, using data points out to 1.6 cm from the wall. By fitting these same data to law-of-the-wall format (Figure 4.4), it was also possible to calculate the friction velocity U_T .

4.4 The Measured Modal Radiation Damping of the Membrane

Modal damping measurements were made on selected modes of the rectangular membrane. Since the membrane had high aspect ratio, a large number of low order modes were well separated in frequency. The modes of interest were the (m, n) modes with $m = 5, 7, 9, \dots, 29$ and $n = 1$. These modes demonstrated distinct resonant peaks. At frequencies below the resonant frequency of the $(5, 1)$ mode, frame interaction effects obstructed good measurements. At frequencies above the resonant frequency of the $(29, 1)$ mode, the response was into the instrumentation noise floor.

All damping tests were made with the membrane mounted in the wind tunnel test section. The measured modal resonant frequencies, f_{mn} , are listed in Table 4.2. Experimentally determined loss factors, η_T , at these resonances with Mach numbers 0.0 and 0.23 are listed in Table 4.1. The total loss factor η_T is the sum of the radiation loss factor, η_R , and the structural loss factor, η_S , that is

$$\eta_T = \eta_S + \eta_R \quad (4.1)$$

From the basic definitions we can show that the radiation loss factor η_R is related to the modal radiation resistance in the following form, remembering that there was flow on only one side of the panel,

$$\eta_R(M) = \frac{\rho c}{\omega m_p} \left[\sigma_{mn}^O + \sigma_{mn}^M \right] \quad (4.2)$$

and that

$$\eta_R(M=0) = \frac{2\rho c}{\omega m_p} \sigma_{mn}^O \quad (4.3)$$

(see Table 4.1). Digitally computed modal radiation resistances at measured resonant frequencies are listed in Table 4.2. Figure 4.5 shows digitally computed radiation resistances for the (5,1) mode over a wide wave number range.

The structural damping in a thin vibrating panel is mainly due to losses at the boundaries, either because of transfer of energy to other parts of the system or because of, say, viscous dissipation in the support mechanism. Thus, the structural damping is related to the group velocity for propagating waves in the panel. In the present experimental setup, there were no pressure differences across the membrane greater than 0.2 cm of water at Mach number $M = 0.23$. It can be shown that, with this amount of pressure difference, there will be negligible increase in the membrane tension and hence no effect on the membrane damping.

Therefore, we are justified in assuming that the structural damping, η_S , is a constant independent of the flow speed, that is,

$$\eta_S(M = 0) = \eta_S(M = 0.23) \quad (4.4)$$

Eqs. (4.1) and (4.2) lead us to

$$\eta_T(M=0.23) - \eta_T(M=0) = \eta_R(M=0.23) - \eta_R(M=0) \quad (4.5)$$

On the left hand side of the equation, there are two quantities which can be experimentally determined. On the right hand side of the equation, there are two quantities which can be numerically determined. Table 4.1 illustrates the comparisons.

The comparisons are not significant except for the (5,1) mode. Note that both the left hand side and the right hand side of the Eq. (4.5) are differences of two large and nearly equal numbers in most of the cases. For the (5,1) mode, however, the differences are 39% or more of the total loss factor η_T at $M = 0.23$. Therefore, the result for this mode gives a significant comparison.

It is to be noted that the acoustic radiation accounts for a significant part of the total damping, at least for the lower order modes. This contradicts the assumption usually made in the past that $\eta_T \simeq \eta_S$ at $M = 0$ even for the first fundamental mode (e.g. [23]).

4.5 The Measured Added Mass Surface Density

For an ideal membrane the *in vacuo* membrane wave speed is

$$C = \left(\frac{T}{m_p} \right)^{1/2}. \quad (4.6)$$

The added mass surface density manifests itself as a change in the membrane wave speed

$$c_{mn}^M = \left(\frac{T}{m_p + m_{mn}^M} \right)^{1/2} \quad (4.7)$$

Since the added mass surface density is proportional to the inverse of the frequency, the membrane wave speed c_{mn}^M approaches asymptotically the *in vacuo* membrane wave speed C at high frequencies. c_{mn}^M can be determined by the measurements on f_{mn}^M and the knowledge of k_{mn} . Previous workers used graphs similar to those plotted in Figure 4.6 to select this asymptotic value C , and determine the membrane tension T . Martin and Leehey [21] followed this practice for the no flow case and determined the *in vacuo* membrane wave speed C as 134 m/sec, and therefrom, the effective modal mass surface densities, i.e. $(m_p + m_{mn})$, for the same membrane used in the present study (Figure 4.7). Knowing $m_p = 0.286 \text{ kg/m}^2$, we can find the added mass surface density m_{mn} . And, since $m_{mn} = (\rho c / \omega) 2\chi_{mn}$, the non-dimensional radiation reactance χ_{mn} is readily available. These data are compared with the values obtained through numerical calculations in Table 4.3. The comparison shows large discrepancies. Before discussing these discrepancies, let us study another case.

The data shown in Figure 4.6 was experimentally determined by Sledjeski [14] on a mylar membrane with the following physical characteristics:

- a. Surface dimensions $\ell_1 = .3048 \text{ m}$
 $\ell_3 = .2032 \text{ m}$

- b. Aspect ratio: $R = 1.5$
- c. Thickness: $h = 0.2599 \text{ mm}$
- d. Surface density: $m_p = 0.36 \text{ kg/m}^2$.

It was manufactured the same way as our present membrane. However, Sledjeski's membrane, compared to ours, had an aspect ratio closer to 1 and was larger in size. If we assume the *in vacuo* membrane wave speed, C , is 100 m/sec for the data shown in Figure 4.6, the modal radiation reactance χ_{mn} can be calculated. These data are compared with the values obtained through numerical computations in Table 4.4. The closer agreement shown in Table 4.4 as compared to Table 4.3 is at least partially due to the smaller bending stresses introduced in Sledjeski's membrane, since the modes he studied had lower modal wave numbers. The higher bending stresses in the present membrane probably explain why, in Figure 4.7, the membrane wave speed increases almost linearly with respect to frequency from the (15,1) mode up, rather than approaching an asymptotic value. Figure 4.7 also includes the analytical *in vacuo* membrane wave speed

$$C_{mn} = c_{mn} (1 + 2\rho c \chi_{mn}/\omega m_p)^{1/2} \quad (4.8)$$

with χ_{mn} being digitally computed.

5. THE EXPERIMENTAL PROGRAM FOR THE RADIATION
RESISTANCE MEASUREMENTS OF A RECTANGULAR
STEEL PLATE

For a large thin panel the structural modal density is high. It is difficult to identify each individual mode. Instead, we made radiated sound power level and panel vibration level measurements in several frequency bands. From these measurements we determined the averaged radiation resistance for the resonant modes within each of the frequency bands. These results were then compared with our analytical predictions.

Davies [3] made similar measurements and estimates. However, he was concerned with the sound power radiated on the side away from the flow for panels excited by turbulent boundary layer pressure fluctuations. We measured the sound power radiated into the flow from a panel excited by an electromagnetic transducer. In addition, we made measurements up to Mach number 0.23.

5.1 Equipment and Procedures for the Radiation
Resistance Measurements

The experimental setup used in the radiation resistance measurements is shown in Figure 5.1. The stainless steel plate was flush-mounted on the top wall of the wind tunnel. The lower surface of the panel was exposed to the flow, and the upper surface

was enclosed by a 2 cm thick plywood box with inner dimensions of 61 cm x 80 cm x 38 cm. The pressure differential across the test plate was maintained at less than 5 mm of water even at Mach number 0.23 by providing four 3 mm diameter pressure releasing holes on the top wall of the box. According to Davies and Sowayel [12], this pressure differential causes no significant increase in the in-plane tension and, hence, no effect on panel damping. To absorb the radiation from the non-flow side of the panel, fiberglass material was stuffed into the box except in the small space over the panel provided for the transducers described in the next two paragraphs. To further retard radiation into the reverberant chamber, heavy damping material was applied to all of the box walls. With these arrangements the insertion loss of the box was between 13 and 16 dB for acoustic transmission in the frequency range of interest. We assumed the radiation from the no flow side of the panel is not greater than the radiation from the side exposed to the flow. The insertion loss of the enclosing box assured that there would be an appreciable contribution to the measured radiation from the no flow side of the steel plate. All other portions of the tunnel ducting were of double wall construction with 5.1 cm sand between the walls.

The stainless steel test panel was electro-magnetically excited at its center by a 3.5 cm diameter solenoid. The solenoid was activated with a current composed of both a.c. and d.c. components. The a.c. component was bandpassed white noise. The filters used were a 1/3-octave filter for the non-flow case and a 50-Hz wide filter for the Mach number equals 0.23 case. The d.c. component acted as a bias so that most of the panel vibration induced was proportional to the a.c. excitation signal rather than to its square. The deflections of the plate due to the bias were small and, according to Davies and Sowayel [12], they should not induce appreciable in-plane tension and additional damping.

The panel displacement levels were observed through two Fotonics fiber-optic sensors. The signals from these sensors were passed through filters having the same frequency band settings as the ones in the excitation circuit described above. The difference between the displacement level measured with the test panel excited by the solenoid and the background displacement level measured with the solenoid inactivated was much greater than 10 dB.

The test section was operated in the open jet mode as described in the previous Chapter. It was enclosed in a 2 m x 3 m x 4 m reverberant room. In the 50 Hz band centered on 400 Hz, the lowest frequency band measured, 54 room modes were excited. Three one inch B & K microphones in the reverberant field in the room were used to measure the sound pressure levels. The chamber calibration to give radiated power estimates from sound pressure estimates was determined from measurements of the decay time of a noise signal in the chamber. The reverberation times measured using a 1/3-octave filter and a 50 Hz filter were nearly the same. These times are listed in Table 5.1. A minimum difference of 10 dB between the sound pressure level measured with the test panel excited by the solenoid and the background noise level measured with the solenoid inactivated determined the range of the acceptable values of the sound power measurements for all test situations including the $M = 0.23$ case.

The absorption α is related to the reverberation time T_R , the acoustic wave speed c and the volume of the chamber V through the following expression (see Morse and Ingard [16], p. 579).

$$\alpha = 55.3 V/c T_R.$$

For the longest reverberation time we had an absorption $\alpha = 2.7 \text{ m}^2$ which was still much larger than 0.13 m^2 , the total area of the openings connecting the chamber through the ducts to the out side. Therefore, it seems reasonable to neglect the effect of duct flow on the reverberation time of the room.

In a latter section we will describe how to apply these measured data to find the radiation resistance of the resonantly excited plate modes.

5.2 Plate Construction

The panel was made of stainless steel shim stock marketed by Harbor Tool Supply Co., Boston, Massachusetts. It was attached to a rectangular aluminum frame using a commercial Ecco Bond epoxy (see Figure 5.2). The frame consisted of four $1.2 \text{ cm} \times 1.91 \text{ cm}$ rectangular bars 28 or 33 cm long having torsional resonant frequencies at about 2.3 kHz. The surface of the panel was carefully positioned to be flush with the rest of the duct wall. The panel was oriented to have its shorter dimension parallel to the flow direction. The result of these preparations was a rectangular steel panel with the following physical characteristics:

- a. Surface dimension, $\ell_1 = 27.9 \text{ cm}$, $\ell_3 = 33 \text{ cm}$

- b. Aspect ratio, $R = 0.8455$.
- c. Thickness, $h = 0.152$ mm.
- d. Acoustic critical frequency, $f_c = 85.4$ kHz.
- e. Frequency modal density, $(f) = 0.208$ Hz⁻¹.
- f. Surface density, $m_p = 1.17$ kg/m².
- g. Flexural rigidity, $D = 5.78 \times 10^{-2}$ kg m²/sec².

5.3 Experimentally Determined Panel Radiation Resistance

The plate was excited by a source located at its geometric center. Many structural modes were excited and contributed to the acoustic radiation. These structural modes could be grouped into the following three categories:

a. The resonantly excited modes which were inefficient radiators, since their resonant frequencies were far below the critical frequency of the panel $f_c = 85.4$ kHz. We will call these the resonant modes.

b. The particular lower order modes which were excited at frequencies substantially above their resonances such that their wave speeds were supersonic. Hence, they became efficient radiators. We will call them the supersonic modes.

c. All the other modes which were non-resonantly driven and were inefficient radiators.

The ensuing analysis will reveal to us what kind of information can be derived from the measured panel vibration and radiation data. The effect of added mass is negligible compared to the plate mass surface density.

Let us assume that the rectangular steel panel has modes which can be represented by the orthogonal characteristic functions

$$\psi_{ij}(\underline{x}) = 2 \sin(i\pi x_1/\ell_1) \sin(j\pi x_2/\ell_2)$$

Due to the orthogonality, $\langle \psi_{ij} \psi_{kl} \rangle_{\underline{x}} = \delta_{ik} \delta_{jl}$, where $\langle \dots \rangle_{\underline{x}}$ denotes spatial average of the function inside the bracket over the surface of the panel.

From here on, we denote \bar{V}_{mn} , V_{pq} , and V_{rs} as the modal velocities for the resonant, the supersonic and the other modes, respectively. Hence, the spatial average of the square of the panel velocity V can be expressed in the form

$$\begin{aligned} \langle V^2 \rangle_{\underline{x}} &= \langle (\sum_{ij} V_{ij} \psi_{ij})^2 \rangle_{\underline{x}} \\ &= \sum_{ij} V_{ij}^2 \\ &= \sum_{mn} \bar{V}_{mn}^2 + \sum_{pq} V_{pq}^2 + \sum_{rs} V_{rs}^2 \end{aligned} \quad (5.1)$$

where \sum_{mn} represents a summation over the resonant modes, \sum_{pq} over the supersonic modes, and \sum_{rs} over the other modes.

We further assume small structural damping, such that the resonant modes will dominate the response, i.e.

$$\langle v^2 \rangle_x \approx \sum_{mn} \bar{v}_{mn}^2 \quad (5.2)$$

If the forcing function is band-passed white noise with band width $\Delta\omega$, there are then $N = n(\omega)\Delta\omega$ modes resonantly excited in $\Delta\omega$, with $n(\omega)$ being the plate modal density.

The equation of motion for the plate being excited at \underline{x}_s by a concentrated force is

$$[\kappa c_\ell^4 - \omega^2(1-i\eta)]y = \frac{Fe^{-i\omega t}}{m_p} \delta(\underline{x} - \underline{x}_s) \quad (5.3)$$

where κ = radius of gyration
 c_ℓ = bending wave speed
 η = total loss factor
 m_p = plate mass area density
 F = force amplitude

After expanding the displacement and the excitation in terms of the eigenfunctions, Eq. (5.3) will lead us to

$$[-\omega_{ij}^2 + \omega^2(1-i\eta)]y_{ij} = \frac{F}{Am_p} \psi_{ij}(\underline{x}_s) \quad (5.4)$$

where $y_{ij} = \langle y \psi_{ij} \rangle_{\underline{x}}$ is the modal displacement. The modal velocity

$$v_{ij} = \frac{d}{dt} y_{ij} = -i\omega y_{ij} \quad (5.5a)$$

can be expressed as

$$v_{ij} = \frac{-i\omega F \psi_{ij}(\underline{x}_s)}{A m_p [\omega^2 - \omega_{ij}^2 - i\eta\omega^2]} \quad (5.5b)$$

For the resonant modes, Eq. (5.5b) becomes

$$\bar{v}_{mn} \approx \frac{F \psi_{mn}(\underline{x}_s)}{\eta\omega A m_p} \quad (5.6)$$

For the supersonic modes we have

$$v_{pq} \approx -i \frac{F \psi_{pq}(\underline{x}_s)}{\omega A m_p}, \quad (5.7)$$

since $\omega \gg \omega_{pq}$ and $1 \gg \eta$.

Eqs. (5.2) and (5.6) will then give

$$\langle v^2 \rangle_{\underline{x}} + N \left(\frac{F}{\eta\omega A m_p} \right)^2 \langle \psi_{mn}^2(\underline{x}_s) \rangle_{mn} \quad (5.8)$$

where $\langle \psi_{mn}^2(\underline{x}_s) \rangle_{mn} \equiv [\sum_{mn} \psi_{mn}^2(\underline{x}_s)]/N$, and

$N \approx n(\omega)\Delta\omega$ is the number of resonant modes in the frequency band of interest, $\Delta\omega$, with $n(\omega)$ being the plate modal density in ω . For $\underline{x}_s = (\ell_1/2, \ell_3/2)$, $\psi_{mn}^2(\underline{x}_s)$ is equally likely to assume any one of the following values,

depending on whether m and n are even or odd

$\psi_{mn}^2(\underline{x}_s)$	4	0	0	0
m	odd	odd	even	even
n	odd	even	odd	even

If the number of modes N within $\Delta\omega$ is large enough,

$\langle \psi_{mn}^2(\underline{x}_s) \rangle_{mn} \approx 1$. Therefore,

$$F^2 = \frac{(\eta\omega A m_p)^2}{N} \langle V^2 \rangle_{\underline{x}} \quad (5.9)$$

From Eqs. (5.7) and (5.9), we have

$$|V_{pq}|^2 = V_{pq} V_{pq}^* = \frac{\eta^2}{N} \psi_{pq}^2(\underline{x}_s) \langle V^2 \rangle_{\underline{x}} \quad (5.10)$$

This gives an estimate for the modal velocity magnitudes of the supersonic modes, based on measured panel vibration levels and loss factors. Actually, in the experiments, we measured the spatial average of the square of the panel displacement y. That is,

$$\langle y^2 \rangle_{\underline{x}} = \sum_{ij} y_{ij}^2.$$

Applying Eq. (5.5a), within a narrow frequency band, will lead us to

$$\langle V^2 \rangle_{\underline{x}} = \omega^2 \langle y^2 \rangle_{\underline{x}}.$$

The total radiated acoustic power π_T may be decomposed into three parts, i.e.

$$\pi_T = \sum_{mn} R_{mn}^M \bar{V}_{mn}^2 + \sum_{pq} R_{pq}^M V_{pq}^2 + \sum_{rs} R_{rs}^M V_{rs}^2 \quad (5.11)$$

where R_{ij}^M is the modal radiation resistance for the (i,j) mode, the superscript M stands for Mach number.

The average radiation resistance for the panel modes resonantly excited is defined by

$$\langle R_{mn}^M \rangle_{mn} \equiv (\sum_{mn} R_{mn}^M \bar{V}_{mn}^2) / (\sum_{mn} \bar{V}_{mn}^2). \quad (5.12)$$

Note that $\sum_{rs} R_{rs}^M V_{rs}^2$ is negligible, since these mode are neither well excited nor efficiently radiating. We will also assume that, for the supersonic modes, $R_{pq}^M = \rho c A$.

Thus Eq. (5.11) becomes

$$\pi_T \approx \sum_{mn} R_{mn}^M \bar{V}_{mn}^2 + \rho c A \sum_{pq} V_{pq}^2 \quad (5.13)$$

From Eq. (5.2) and Eq. (5.10) we have

$$\langle R_{mn}^M \rangle_{mn} \approx \frac{\pi_T}{\langle V^2 \rangle_x} - \frac{\rho c A \eta^2}{N} \left[\sum_{pq} \psi_{pq}^2 (\underline{x}_s) \right] \quad (5.14)$$

The measured plate loss factors are listed in Table 5.2. The (1,1) mode becomes supersonic at 807 Hz without flow. With flow at Mach number 0.23, only 5 modes become supersonic at 1413 Hz, the upper limiting

frequency of the 1/3 octave filter centered at 1250 Hz.

In all of our experimental cases, the contribution from the supersonic modes, $\rho c A \eta^2 [\sum_{pq} \psi_{pq}^2(\underline{x}_s)]/N$, is less than 5×10^{-4} of the total acoustic radiation.

Thus the resonant modes dominate both the panel vibration and panel radiation. From measured panel vibration and radiation levels, we can determine the average radiation resistance for the modes resonantly excited within $\Delta\omega$. Thus, from Eq. (5.14) we get

$$\frac{1}{\rho c A} \langle R_{mn}^M \rangle_{mn} = \frac{\pi T}{\langle V^2 \rangle_x \rho c A} \quad (5.15)$$

If we assume an equipartition of energy takes place among the resonantly excited modes owing to the many modal interactions caused by coupling to the acoustic field (see Lyon and Maidanik [25]), definition (5.12) becomes

$$\begin{aligned} \frac{1}{\rho c A} \langle R_{mn}^M \rangle_{mn} &= \frac{\sum_{mn} R_{mn}^M}{N \rho c A} \\ &\equiv \frac{1}{N} \sum_{mn} \sigma_{mn}^M. \end{aligned} \quad (5.16)$$

remembering that only one side of the panel was radiating to the reverberant chamber in this experiment.

The experimentally determined and digitally computed values of $\langle R_{mn}^M \rangle_{mn} / \rho c A$ as represented by Eqs. (5.15) and (5.16), respectively, are shown in Figures 5.3, 5.4 and 5.5. It is to be noted that, in the digital computation, we assumed rectangular shaped filters 50 Hz or 1/3 octave wide. All the 1/3 octave filters used had bandwidths wider than 50 Hz. In a 50 Hz bandwidth, there were 11 modes which constitutes a large enough population to offer good statistical averages.

5.4 Discussion

In general, the following observations can be made:

- a. For both the $M = 0.0$ and $M = 0.23$ cases the computed data agree with the measured data within 3 dB at the intermediate frequencies, 630, 800, and 1000 Hz. The roll-off of the measured data at high frequency was possible partially due to interactions with the torsional resonances of the aluminum frame at about 2.3 kHz. The large discrepancies between the measured and the computed data at 400 Hz are not understood.
- b. Digitally computed data show only one dB increase in the radiation resistance from $M = 0.0$ to

$M = 0.23$ (see Figure 5.5), while measured data shows larger (2 to 5 dB) increases and are vibration amplitude dependent (Figure 5.4). It is possible that the ratio of the panel displacement amplitude to some characteristic length of the flow may explain the various excess increases in the measured radiation resistance.

This ratio can be varied by:

1. Adjusting the exciting source strength level and thus the plate displacement amplitude y .
2. Changing the flow speed and hence the boundary layer thickness.
3. Thickening the boundary layer with a polyurethane foam placed over the upper half of the wind tunnel inlet. The resulting boundary layer velocity profiles obtained are shown in Figure 5.6.

The panel displacement amplitude y can be non-dimensionalized by the boundary layer viscous length, that is,

$$y^+ = y u_\tau / \nu \quad (5.17)$$

where u_τ is the friction velocity and ν is the kinematic viscosity of air. Other boundary layer characteristic lengths could have been used in place of ν/u_τ , the

viscous length. However, the percentage changes in those other characteristic lengths, e.g. δ^* and θ , are small and similar to the change in v/u_τ , hence it would not have been possible to distinguish between the influence of outer and inner boundary layer scales on the basis of the tests conducted.

We measured the radiation resistance at three different experimental conditions:

1. $y^+ = 128$, $y = 0.61$ mm, $u_\tau = 3.13$ m/sec;
2. $y^+ = 176$, $y = 0.61$ mm, $u_\tau = 4.26$ m/sec;
3. $y^+ = 375$, $y = 1.30$ mm, $u_\tau = 4.26$ m/sec.

where y is the plate displacement amplitude. The thickness of the plate h is 0.1524 mm. Case 2 was the standard condition with no foam covering the wind tunnel inlet. Case 1 was with the upper half of the wind tunnel inlet covered by a polyurethane foam and with the same excitation level as in Case 2. In Case 3, the plate was excited at a higher level, and there was no foam covering the wind tunnel inlet.

In Figure 5.4, we can observe the following:

1. From Case 1 to Case 2, the boundary layer was made thinner. There were no significant changes in the radiation resistance measurements, in spite of a 36% increase in the friction velocity u_τ .

2. From Case 2 to Case 3, the excitation level was increased. The displacement amplitude was increased 113%. There were 1.5 to 3 dB increases in measured radiation resistance. Compared to Case 1, the increase at 800 Hz was almost 5 dB.

It appears that excess displacement amplitude indeed affects the measured radiation resistance. To properly study the effect of boundary layer thickness, we need a facility which offers a larger variation in boundary layer thickness and flow speeds.

6. CONCLUSIONS AND RECOMMENDATIONS

6.1 Conclusions Regarding the Computer Program for the Radiation Impedance

The computer program attached in Appendix II was developed to compute the radiation impedance expressed in Eq. (2.32). It will give zero values for the cases expressed in Eqs. (2.34), and (2.35) without computation. This computer program will not compute the case expressed in Eq. (2.33). However, there will not be much difficulty in extending the capability of the present numerical procedure to include the computation of Eq. (2.33)

The accuracy of this computer program is assured by these facts:

1. Our computed data agree with Wallace's results for σ_{mn} , although Wallace used different numerical techniques and had a different expression for σ_{mn} .
2. The computed values of χ_{mn}^O and χ_{mn}^M indeed follow the trends found in Eqs. (3.23), and (3.24).

This computer program was formulated to give a cumulative error of less than 2%.

6.2 Conclusions Regarding the Modal Virtual Mass Surface Density

Previous workers determined the added mass experimentally from resonant response measurements

according to

$$m_{mn} = m_p \left(\frac{C^2}{c_{mn}^2} - 1 \right)$$

where C , the *in vacuo* membrane wave speed, is taken from the asymptotic value of c_{mn} at high frequency. The resulted data are sensitive to experimental errors because of the subtractions of 1 from C^2/c_{mn}^2 which are nearly equal 1. We also observed that, at high frequency, the bending stresses due to large modal wave numbers of the higher order modes upset the selection of an asymptotic value from the graphic data of c_{mn} . In one case, the added masses determined experimentally agree with the theoretical prediction for small membrane wave numbers. This further demonstrate the need of a computer program to compute χ_{mn} rather than rely on the experimental methods in determining χ_{mn} experimentally.

6.3 Conclusion Regarding the Modal Radiation Resistance

Since we were only able to measure the increases in total loss factors for the membrane, the comparisons between most of the experimental and the computed results were not significant. This is due to the involvement of subtraction of two large and nearly

equal numbers. Where the increase is large, e.g. for the (5,1) mode of the membrane, the comparison was fairly good.

In the tests on the steel plate, the modal density was high. We were only able to determine the average radiation resistance for the resonantly excited modes. Except at the lowest frequency tested, the agreement between the measurement and the computation was fair.

6.4 Recommendations

The experiments performed by the author at least qualitatively confirmed the increases in modal added mass and modal radiation resistance due to flow. More precise experimental efforts are needed to make better quantitative comparisons with the computer results.

1. A higher flow speed, say $M = 0.5$, will probably reveal more increases in modal radiation impedances in more structural modes.

2. The added mass effect may be larger and clearer, if the tests are performed under water on a thin plate. If experiments are to be performed on a membrane, precise knowledges of its tension and Young's modulus are important. The use of strain gauges on a mylar membrane is not possible, since they can not measure strain on a thin material of low modulus.

The amplitude-dependant increases in the average radiation resistance for the steel plate we tested may be due to either or both of the following:

1. Excess excitation level which would increase the resonant frequencies of the structure modes. This effect will cause lower order modes to be shift into a given frequency band with consequent increase in radiation efficiency.

2. The interaction of flow and structure which is a non-linear effect. There have not been many studies in this direction yet [24]. And our wind tunnel facility was not able to offer a sufficiently large variation in boundary layer thickness and at a higher flow speed which are required to study the presence of such a phenomenon.

Unfortunately, we did not perform these tests at no-flow condition which could at least partially help us to answer these questions.

Node (m,n)	Measured $\eta_T (M = .23)$ $-\eta_T (M=0)$	Computed $\eta_R (M = .23)$ $-\eta_R (M=0)$	M = 0		M = .23	
			η_T	η_R	η_T	η_R
5,1	.024	.0258	.038	.0171	.062	.0429
7,1	.001	.00080	0.20	.0087	.021	.0095
9,1	.001	.00095	.013	.0052	.014	.0061
11,1	.001	.00086	.010	.0032	.011	.0040
13,1	.0006	.00038	.0080	.0026	.0086	.0030
15,1	.0004	.00034	.0072	.0023	.0076	.0026
17,1	.0000	.00024	.0076	.0018	.0076	.0020
19,1	.0002	.00029	.0060	.0015	.0062	.0018
21,1	.0001	.00017	.0060	.0014	.0063	.0016
23,1	.0004	.00017	.0052	.0012	.0056	.0013
25,1	.0001	.00019	.0050	.0011	.0051	.0012
27,1	.0000	.00009	.0051	.0011	.0051	.0012
29,1	.0000	.00012	.0048	.0009	.0048	.0010

TABLE 4.1 Comparison of Measured and Computed Changes in Loss Factors Due to Flow.
 η_T , measured total loss factor.
 η_R , computed radiation loss factor.

Mode (m,n)	M = 0.0		M = 0.23	
	f_{mn}	σ_{mn}	f_{mn}	σ_{mn}
5,1	1186	.0447	1172	.1774
7,1	1325	.0253	1317	.0298
9,1	1477	.0169	1472	.0230
11,1	1647	.0116	1645	.0178
13,1	1838	.0104	1835	.0135
15,1	2028	.0102	2027	.0132
17,1	2237	.0087	2236	.0111
19,1	2440	.0080	2439	.0111
21,1	2651	.0083	2652	.0103
23,1	2867	.0074	2867	.00953
25,1	3095	.0072	3093	.00977
27,1	3319	.0079	3319	.00926
29,1	3548	.0069	3547	.00881

TABLE 4.2 Digitally Computed Non-Dimensional Modal Radiation Resistances for the Membrane Modes at Their Measured Resonant Frequencies.

Mode (m, n)	Experimental			Analytical	
	f_{mn}	c_{mn}	χ_{mn}	χ_{mn}	C_{mn}
5,1	1186	109.6	1.400	.585	121.2
7,1	1325	113.3	1.258	.480	122.2
9,1	1477	115.7	1.185	.435	123.1
11,1	1647	117.8	1.144	.415	124.4
13,1	1838	119.9	1.106	.405	125.8
15,1	2028	121.1	1.127	.395	126.2
17,1	2237	122.6	1.070	.397	127.4
19,1	2440	123.3	1.111	.391	127.7
21,1	2651	124.0	1.125	.390	128.0
23,1	2867	124.6	1.128	.391	128.4
25,1	3095	125.6	1.122	.392	129.1
27,1	3319	126.1	1.101	.391	129.4
29,1	3548	126.7	1.095	.389	129.8

TABLE 4.3 Comparison of Measured and Calculated Values of Modal Radiation Reactance χ_{mn} for the Present Membrane (see [21] and Figure 4.7).

f_{mn} = measured modal resonant frequency

c_{mn} = membrane wave speed ($= \omega_{mn}/k_{mn}$),

C_{mn} = analytical *in vacuo* membrane wave speed.

Mode (m, n)	Experimental			Analytical	
	f_{mn} (Hz)	c_{mn} (m/sec)	χ_{mn}	χ_{mn}	C_{mn} (m/sec)
3, 1	500	90.0	.325	.325	99.97
1, 3	706	93.3	.293	.327	100.8
5, 1	797	93.8	.305	.321	100.4
7, 1	1133	95.8	.281	.327	100.6
9, 1	1466	97.3	.228	.317	101.0
11, 1	1803	97.7	.238	.312	100.7

TABLE 4.4 Comparison of Experimentally and Analytically Determined Modal Radiation Reactance χ_{mn} for Sledjeski's Membrane (see [14] and Figure 4.6).

f_{mn} = modal resonant frequency measured by Sledjeski,

c_{mn} = membrane wave speed,

C_{mn} = analytical *in vacuo* membrane wave speed.

Filter Center Freq. (Hz)	T_R (sec) measured by	
	1/3-octave Filter	50 Hz wide Filter
400	1.52	1.32
500	1.52	1.22
630	1.16	1.12
800	1.22	1.15
1000	1.15	1.06
1250	1.19	1.20

TABLE 5.1 Reverberation Time T_R Measurements for the Reverberant Chamber Enclosing the Test Section.

Filter Center Freq. (Hz)	$10^2 \times \eta$ measured by	
	1/3-octave Filter	50 Hz wide Filter
400	0.408	0.373
500	0.410	0.371
630	0.400	0.381
800	0.382	0.383
1000	0.417	0.388
1250	0.383	0.396

TABLE 5.2 Measured Plate Loss Factors η .

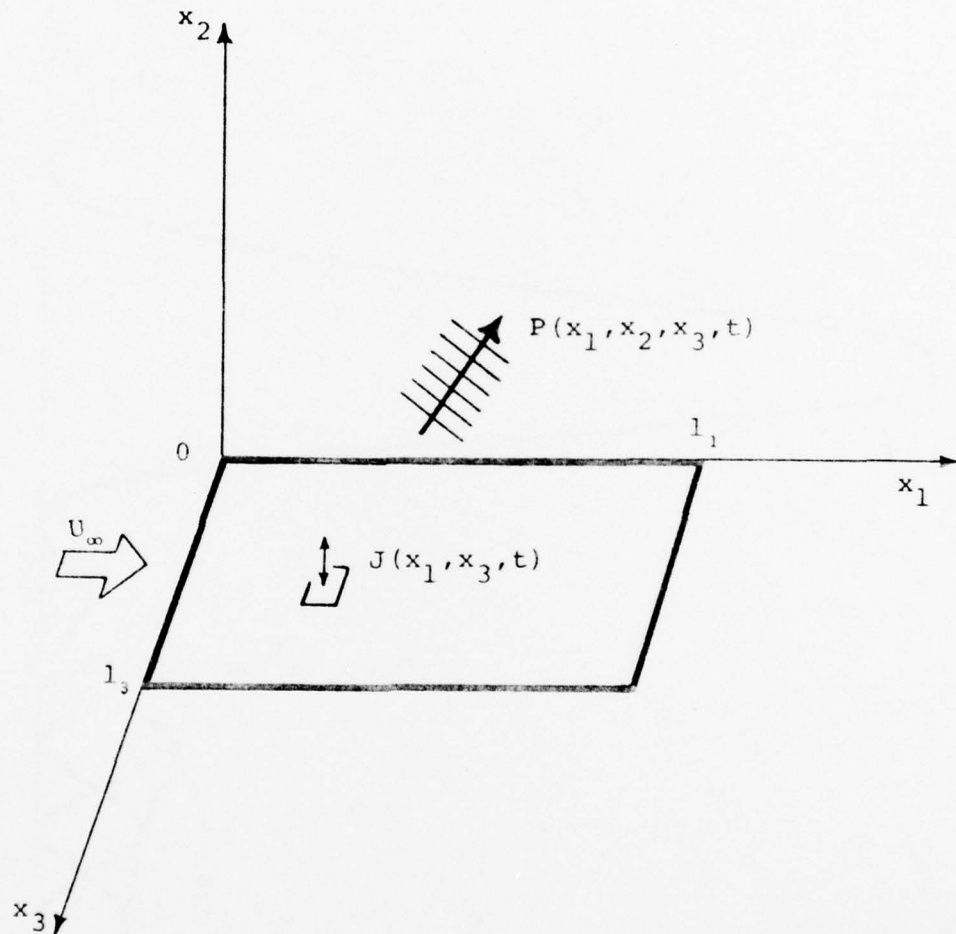


Figure 2.1 Panel with Coordinate system.

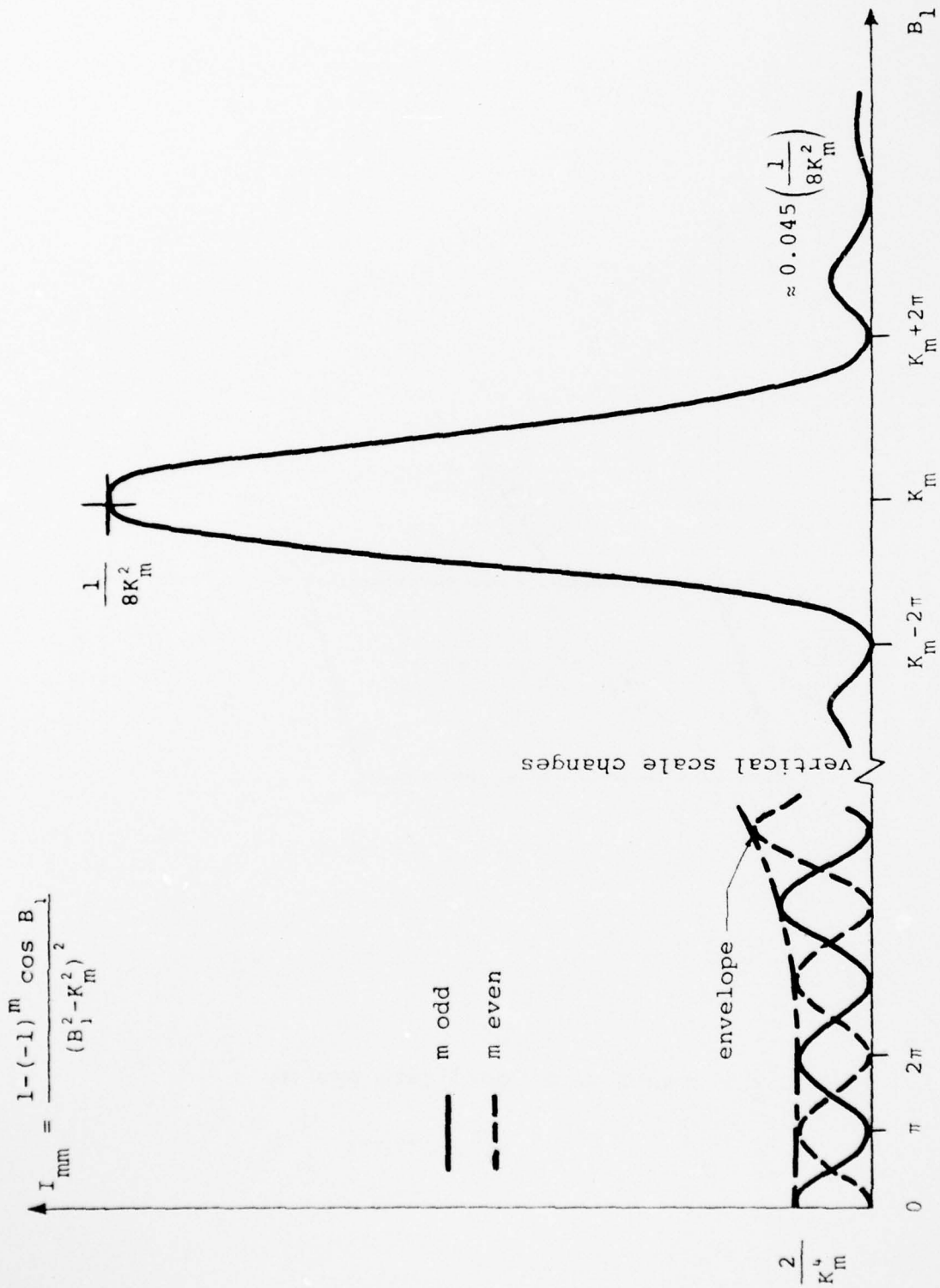


Figure 2.2 Sketch of I_{nm} for large modal numbers m .

AD-A041 268 MASSACHUSETTS INST OF TECH CAMBRIDGE ACOUSTICS AND V--ETC F/G 20/11
THE MEAN FLOW EFFECT ON THE ACOUSTIC IMPEDANCE OF A RECTANGULAR--ETC(U)
FEB 77 Y M CHANG N00014-75-C-0509
UNCLASSIFIED A/V-82464-1 NL

MASSACHUSETTS INST OF TECH CAMBRIDGE ACOUSTICS AND V--ETC F/G 20/11
THE MEAN FLOW EFFECT ON THE ACOUSTIC IMPEDANCE OF A RECTANGULAR--ETC(U)
FEB 77 Y M CHANG N00014-75-C-0509
A/V-82464-1 NL

UNCLASSIFIED

2 OF 2
ADA
041268

END

DATE
FILMED
7-77

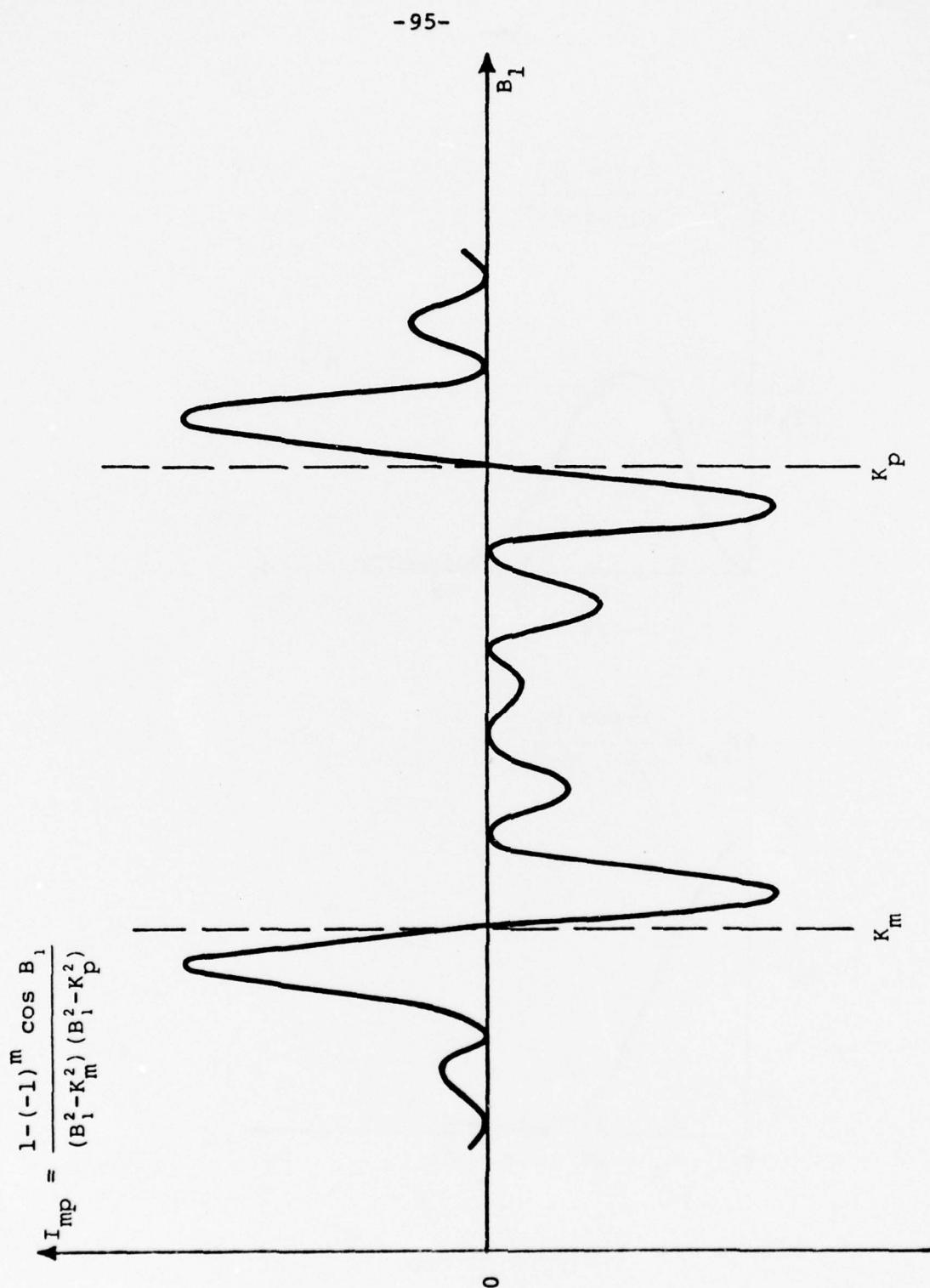


Figure 2.3 A Typical Sketch of I_{mp}

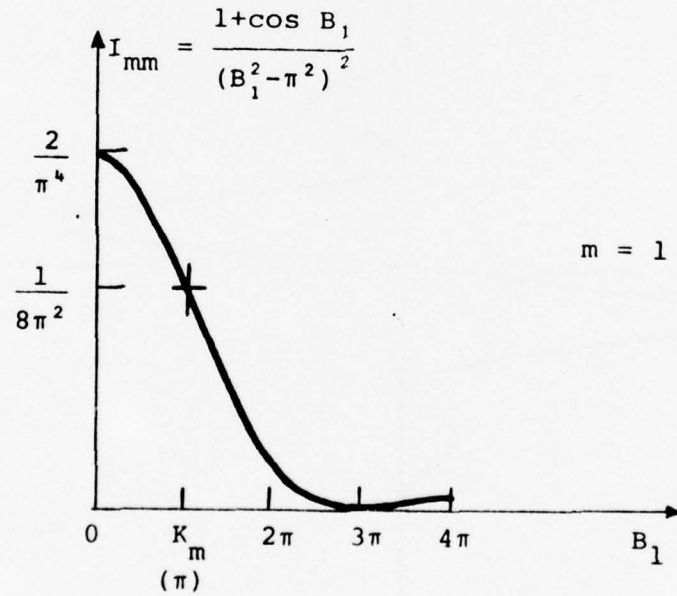
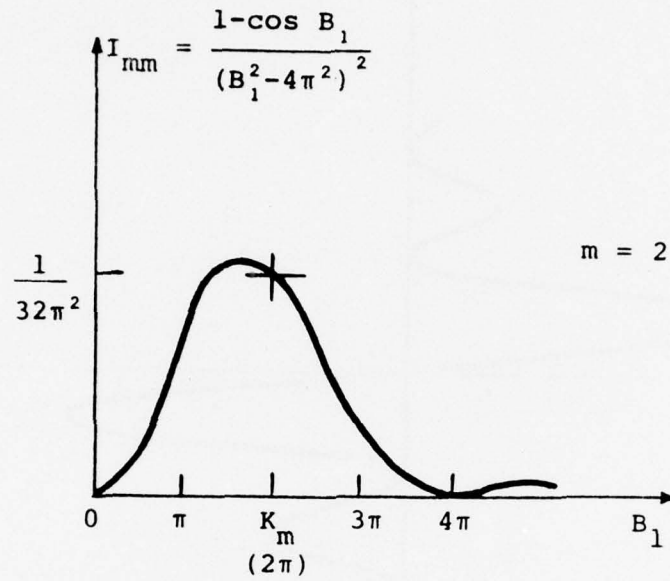


Figure 2.4 Sketches of I_{mm} for $m = 1, 2$.

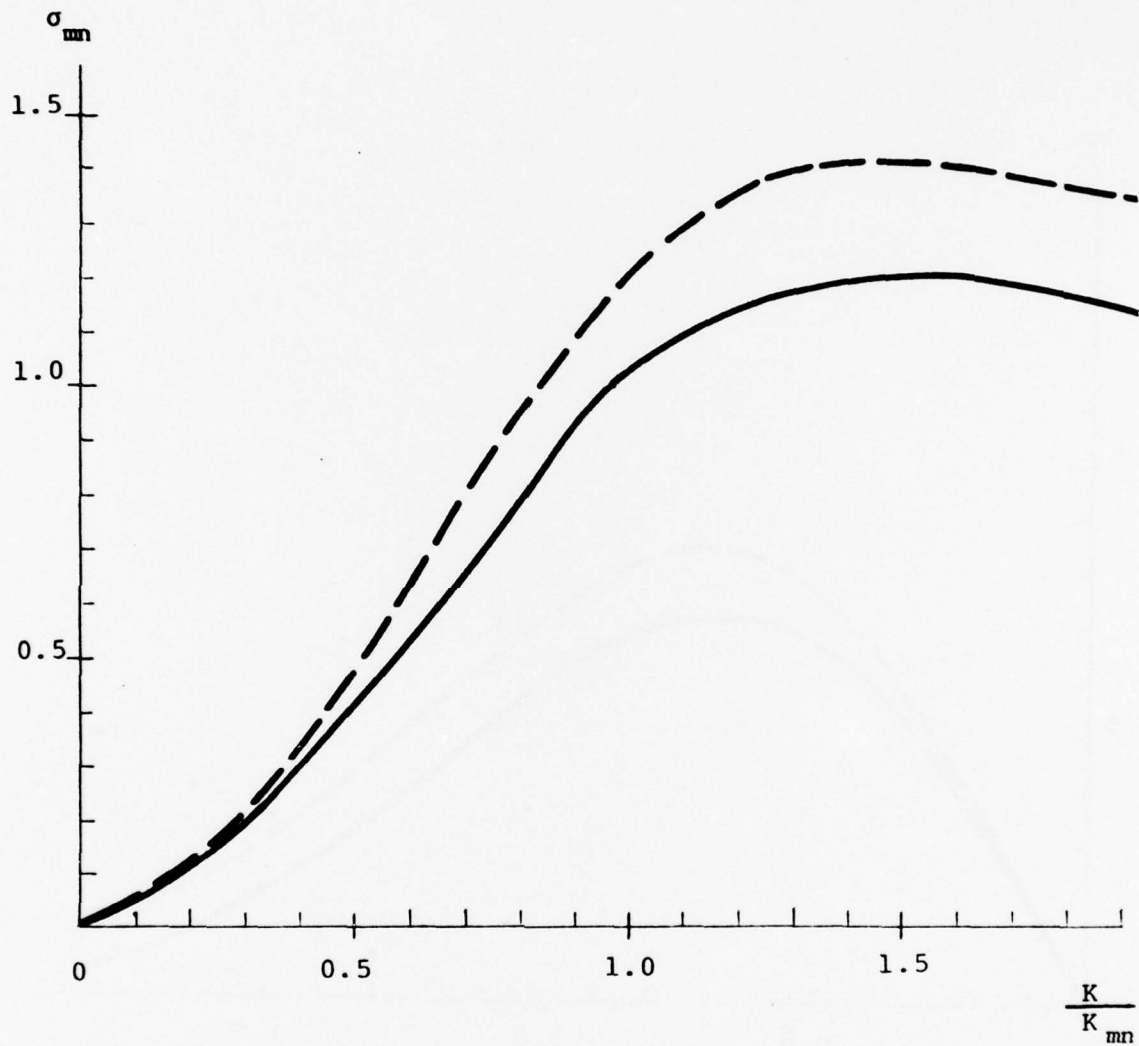


Figure 3.1 The Modal Radiation Resistance for the Fundamental (1,1) Mode of a Square Panel at $M = 0$.
--- Computed by Sandman.
— Computed by Wallace and this author.

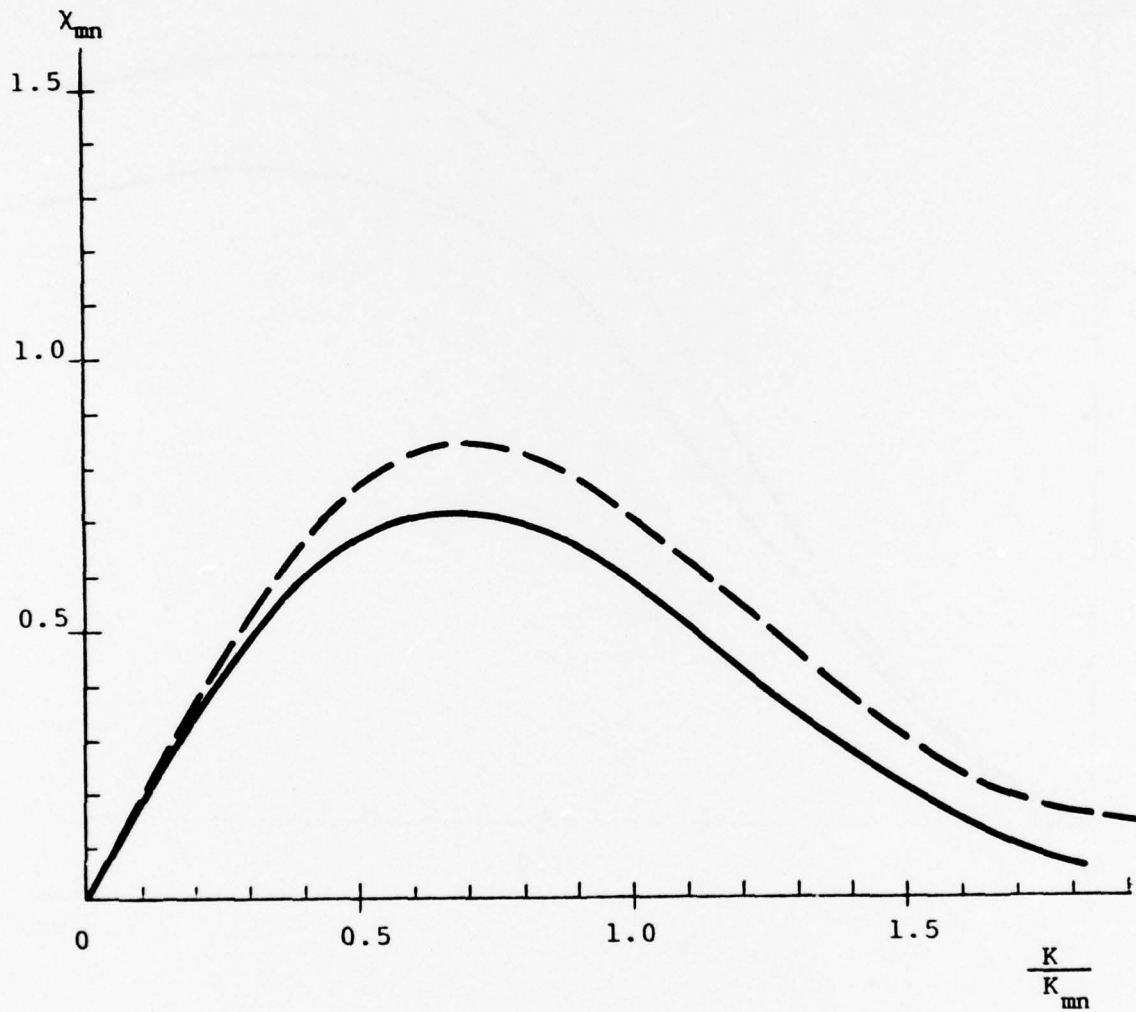


Figure 3.2 The Modal Radiation Reactance for the Fundamental (1,1) Mode of a Square Panel at $M = 0$.
--- Computed by Sandman.
— Computed by this author.

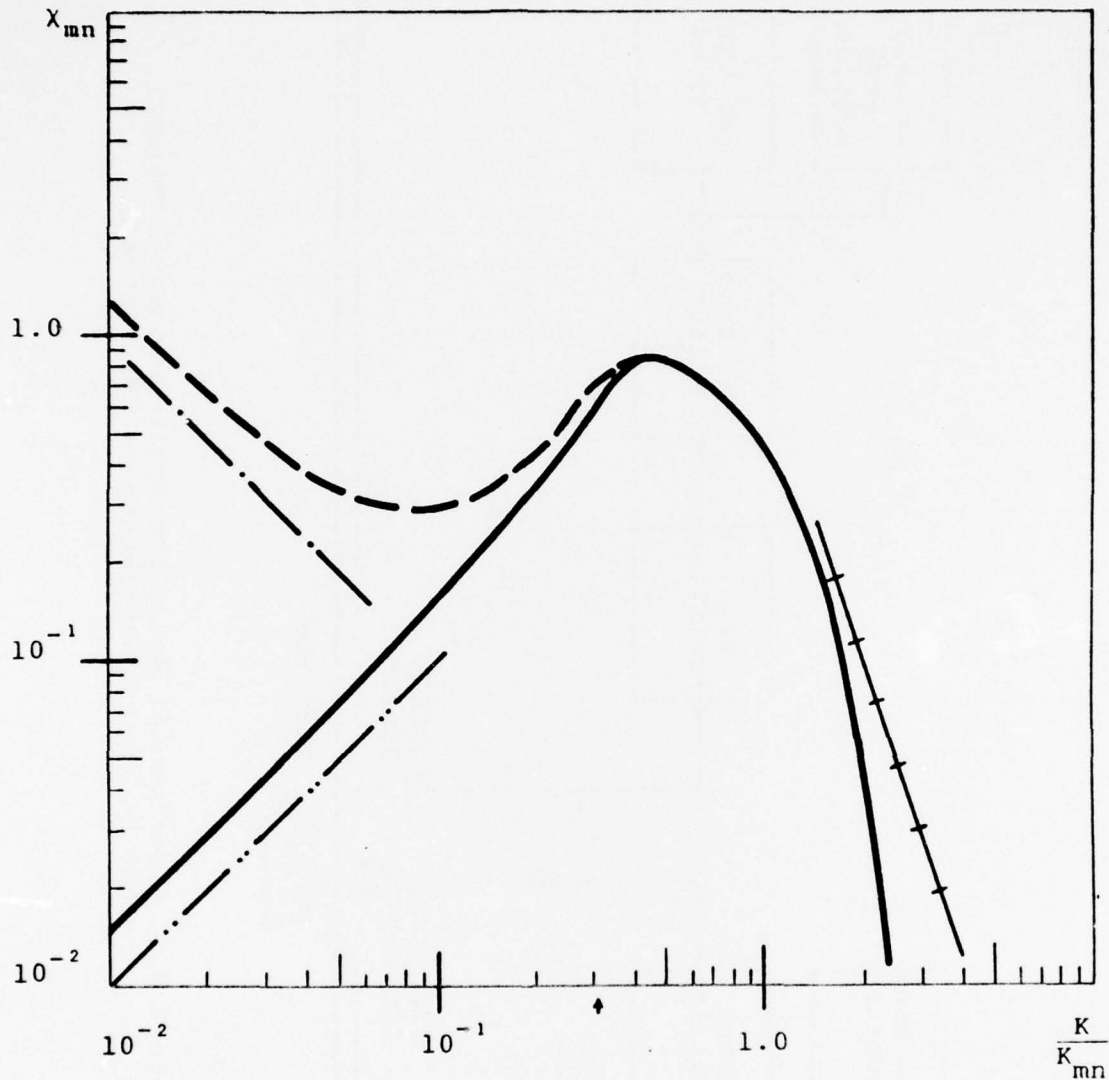


Figure 3.3 Digitally Computed Non-Dimensional Modal Radiation Reactance for a (5,1) Mode with an Aspect Ratio $R = 10.875$.

— $M = 0$. --- $M = 0.23$
 -.- Eq. (4.15) ··· Eq. (4.16)
 +++ Eq. (3.16)

♦ Where the (5,1) mode of our membrane was resonantly excited.

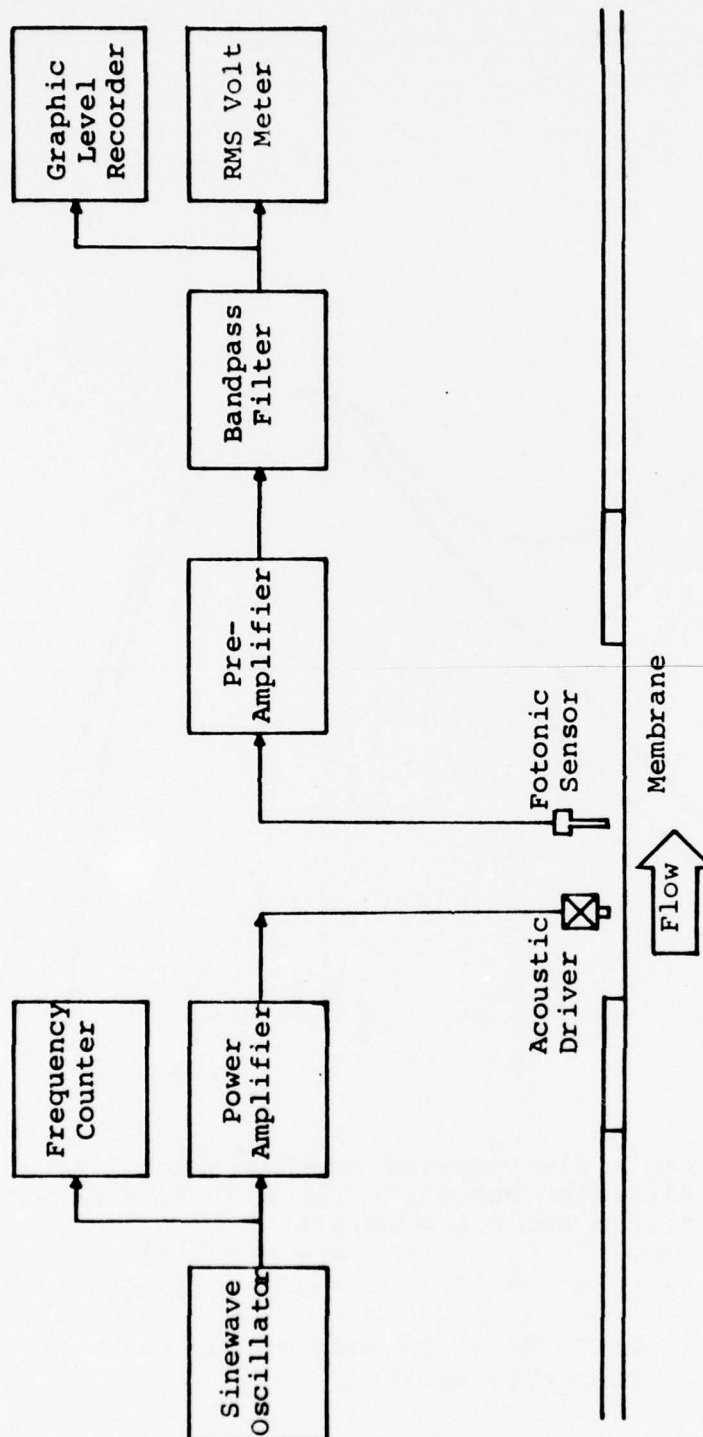


Figure 4.1 Experimental Setup for Modal Resonant Frequency and Damping Measurements on the Membrane.

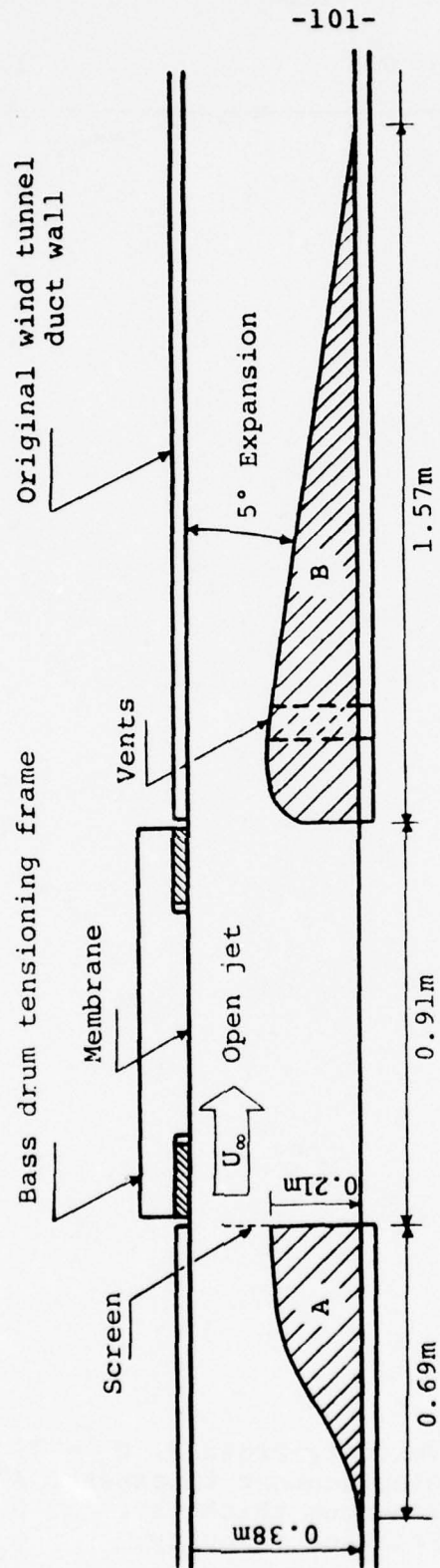


Figure 4.2 The Test Section Box Inserts in the Wind Tunnel

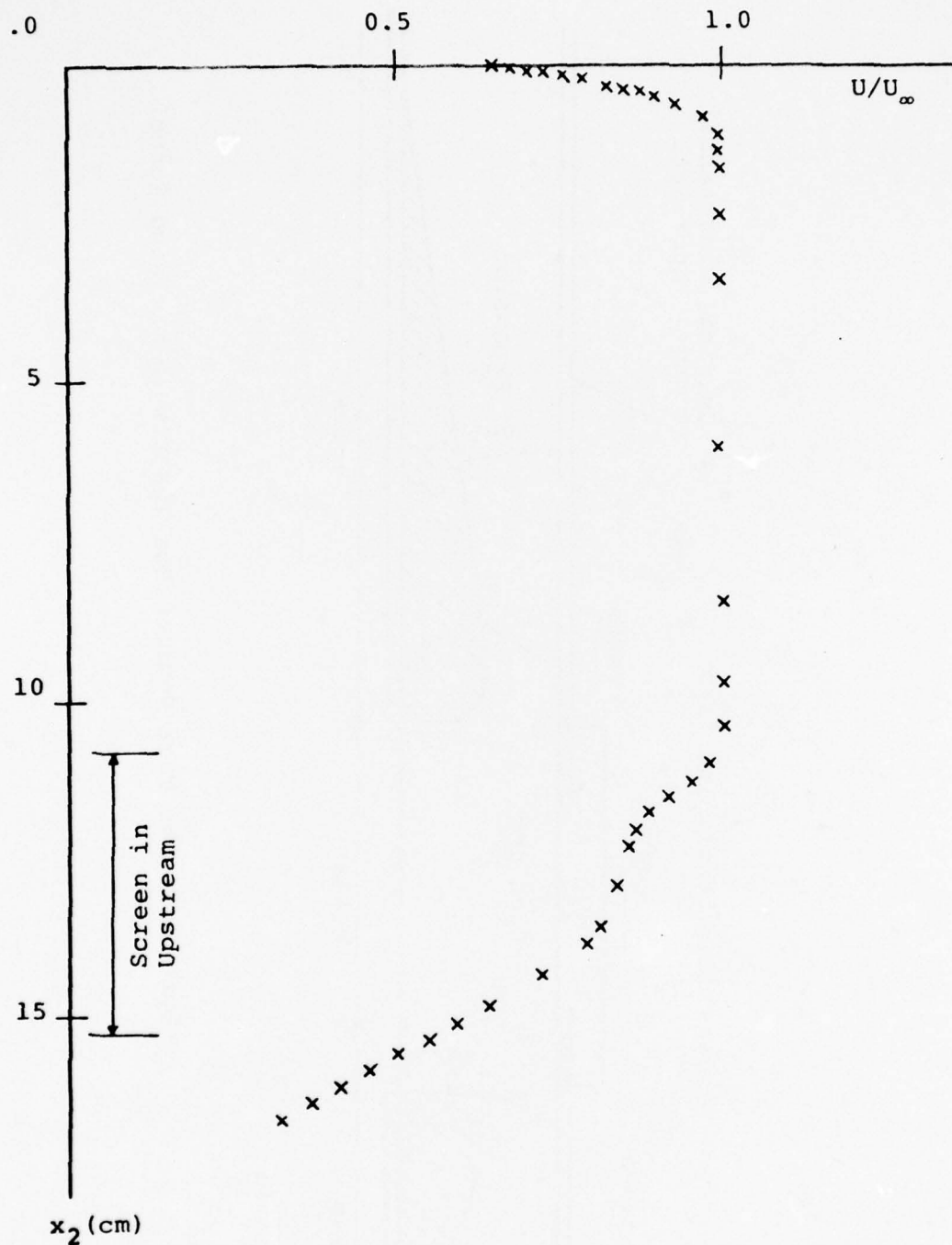


Figure 4.3 Velocity Profile, $U_\infty = 79$ m/sec.
 Displacement thickness, $\delta^* = 1.39$ mm.
 Momentum thickness, $\theta = 1.09$ mm.
 Friction velocity, $u_\tau = 4.26$ m/sec.

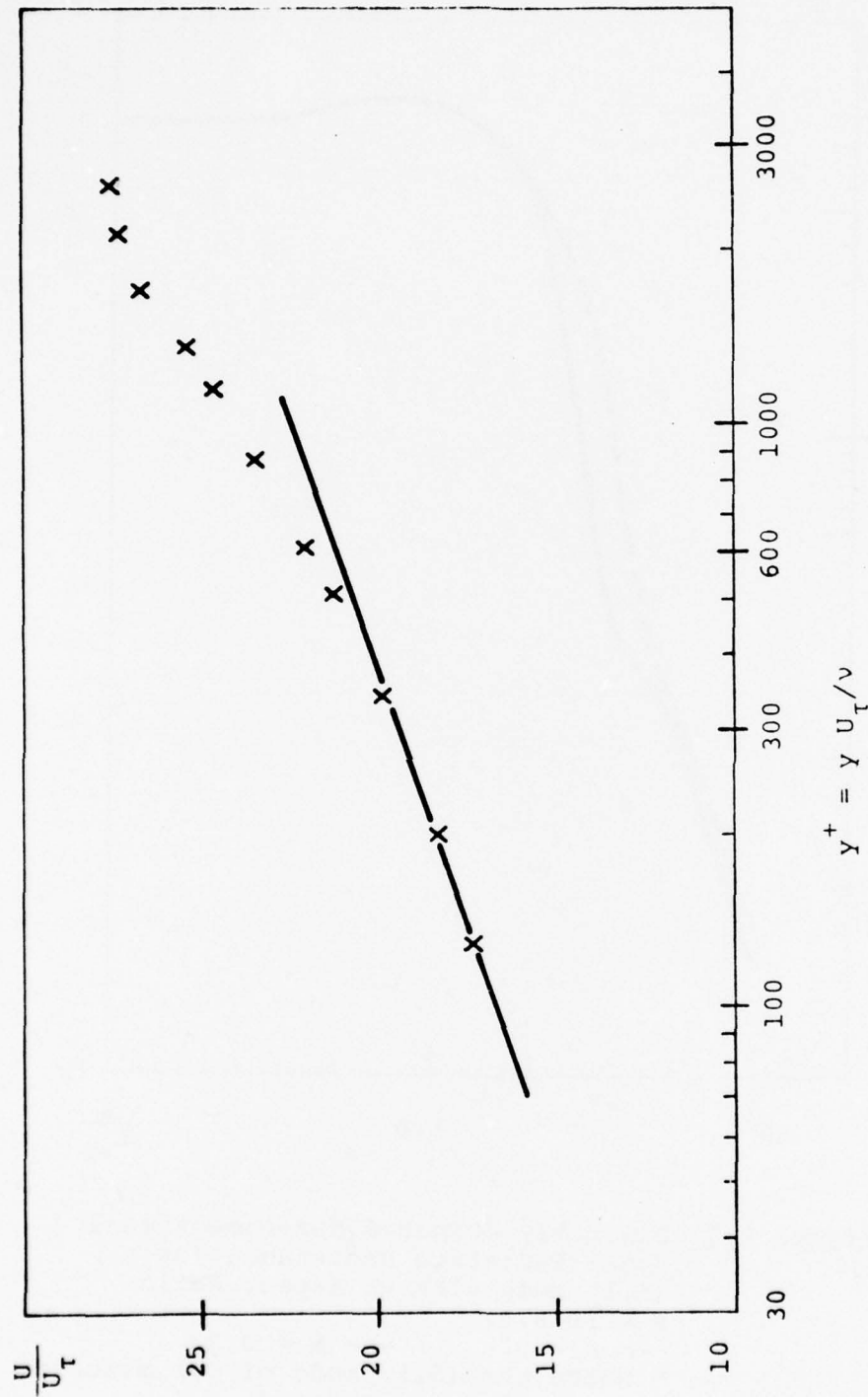


Figure 4.4 The Law of the Wall, $U_\infty = 79$ m/sec, $M = 0.23$.
 $\frac{U}{U_\tau} = 5.75 \log y^+ + 5.5$.

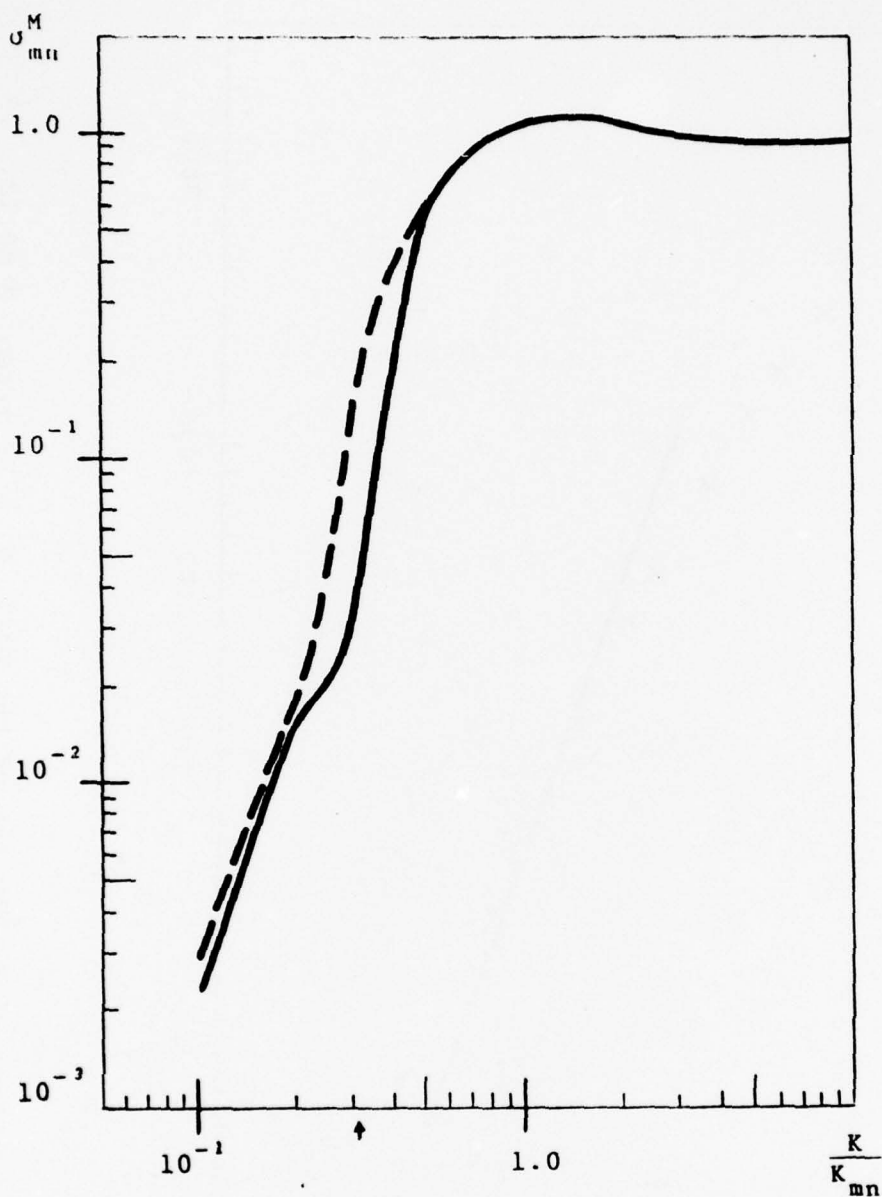


Figure 4.5 Digitally Computed Non-Dimensional Modal Radiation Resistance for a (5,1) Mode with an Aspect Ratio $R = 10.875$.
 — $M = 0$. --- $M = 0.23$
 † Where the (5,1) mode of our membrane was resonantly excited..

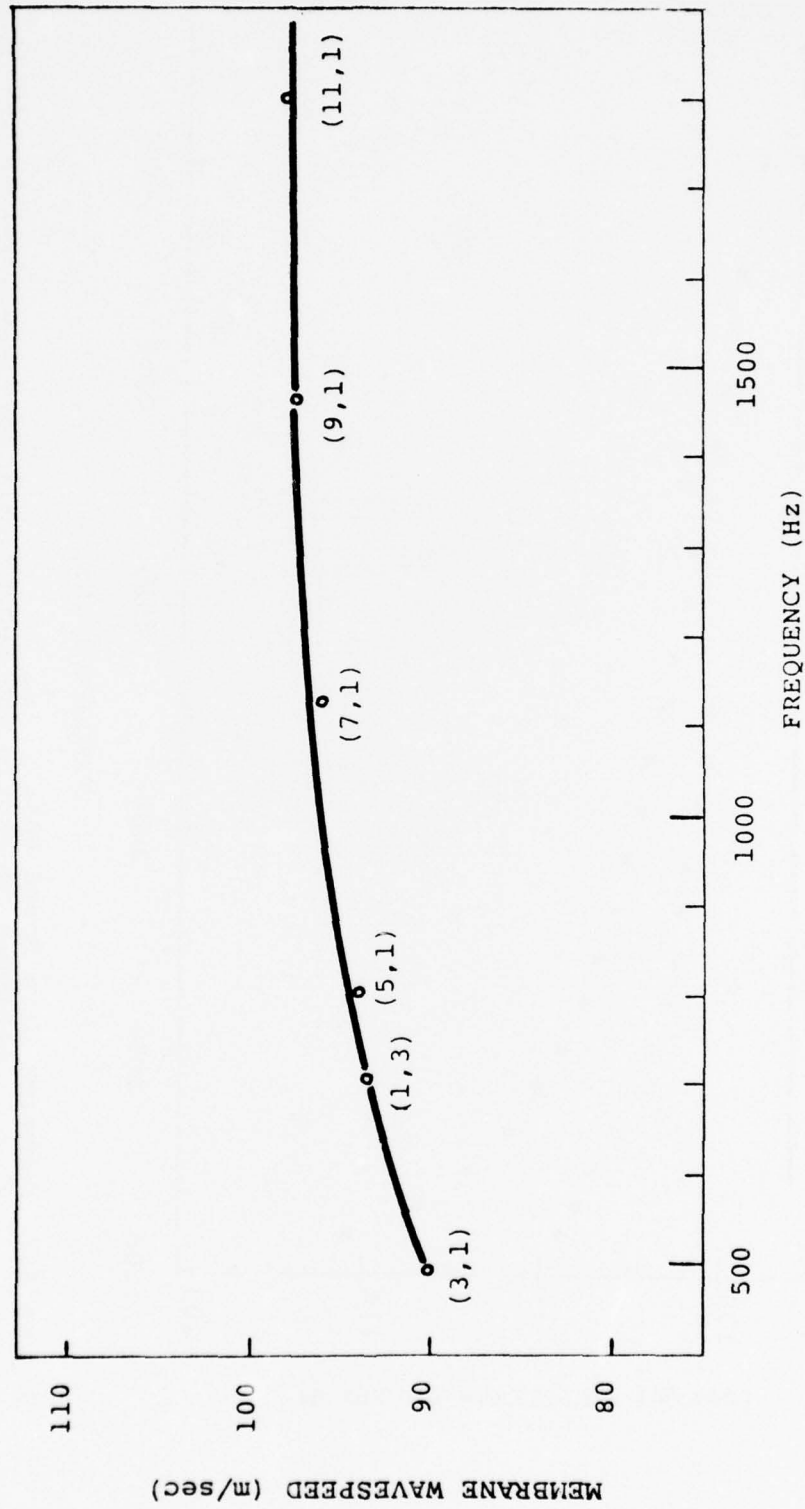


Figure 4.6 Wave Speed Data of Sledjeski's membrane [14] .

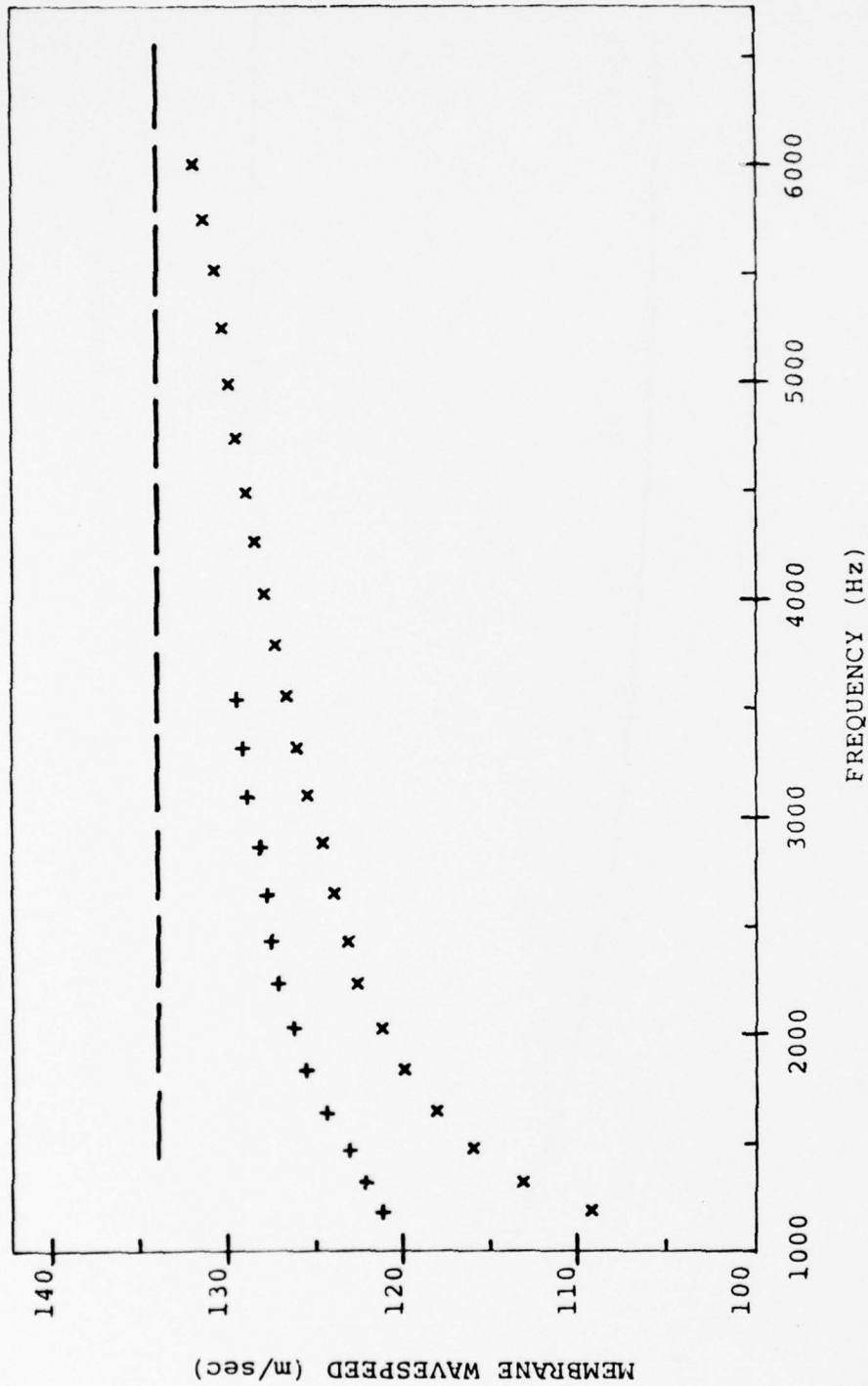


Figure 4.7 Membrane Wave Speed Data.
 x C_{mn} , measured by Martin and Leehey [21] from the (5,1) to (49,1) mode, and by this author from the (5,1) to (29,1) mode.
 + C_{mn} , theoretical in vacuo membrane wave speed.
 --- asymptotic value, 134 m/sec, selected by Martin and Leehey.

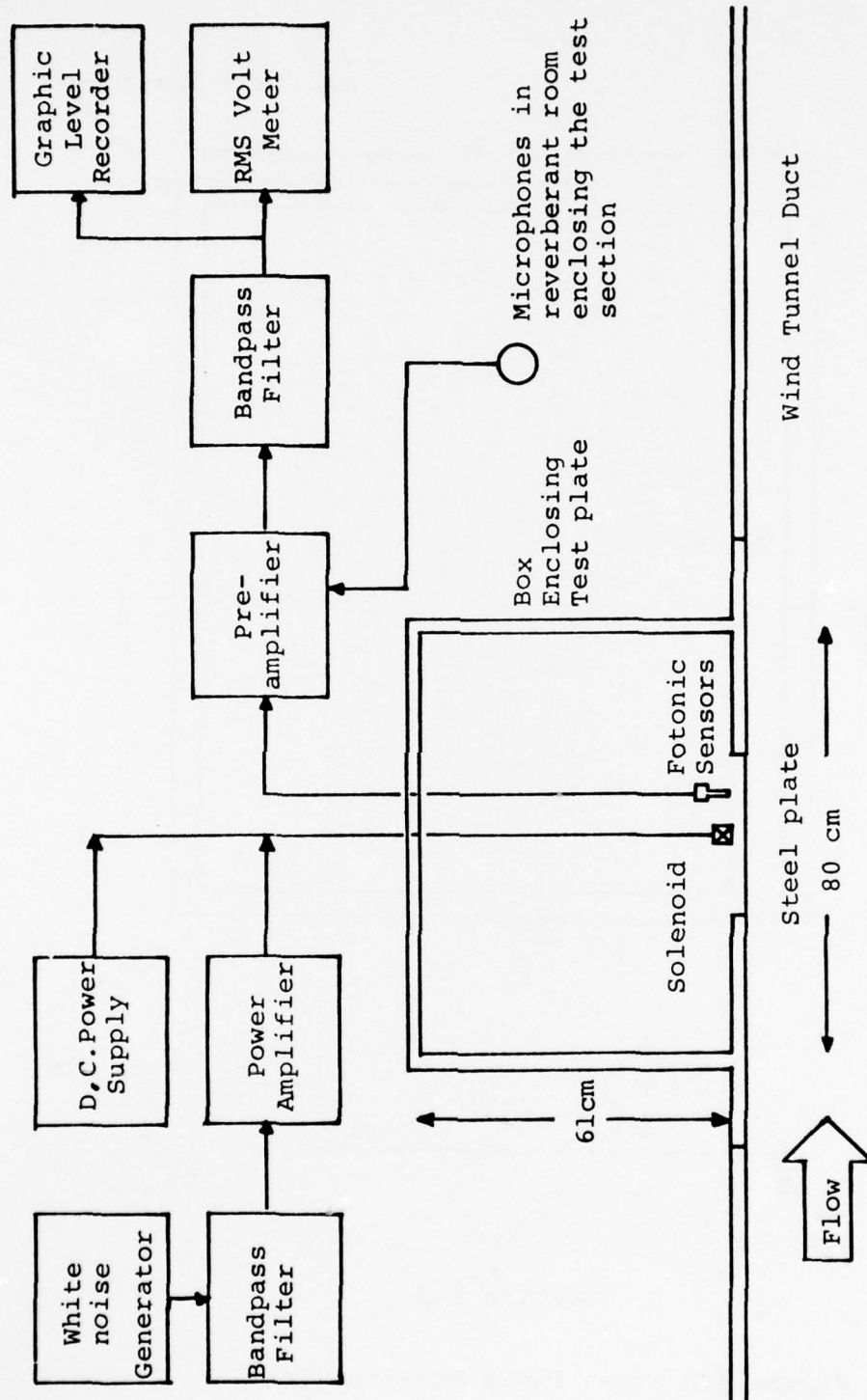
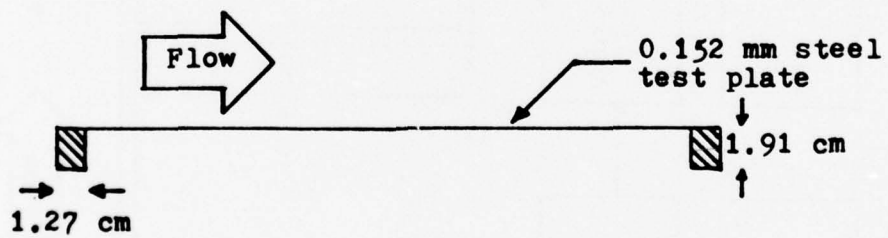
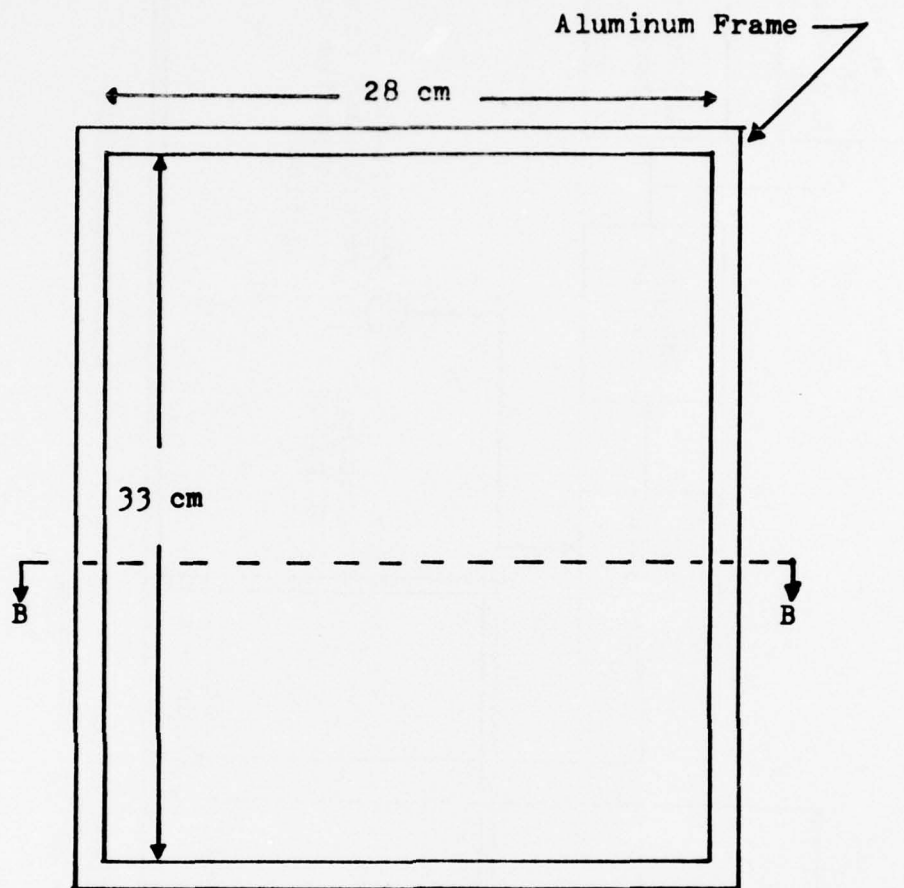


Figure 5.1 Experimental setup for panel vibration and radiation measurements.



Section B-B

Figure 5.2 Steel Plate Construction.

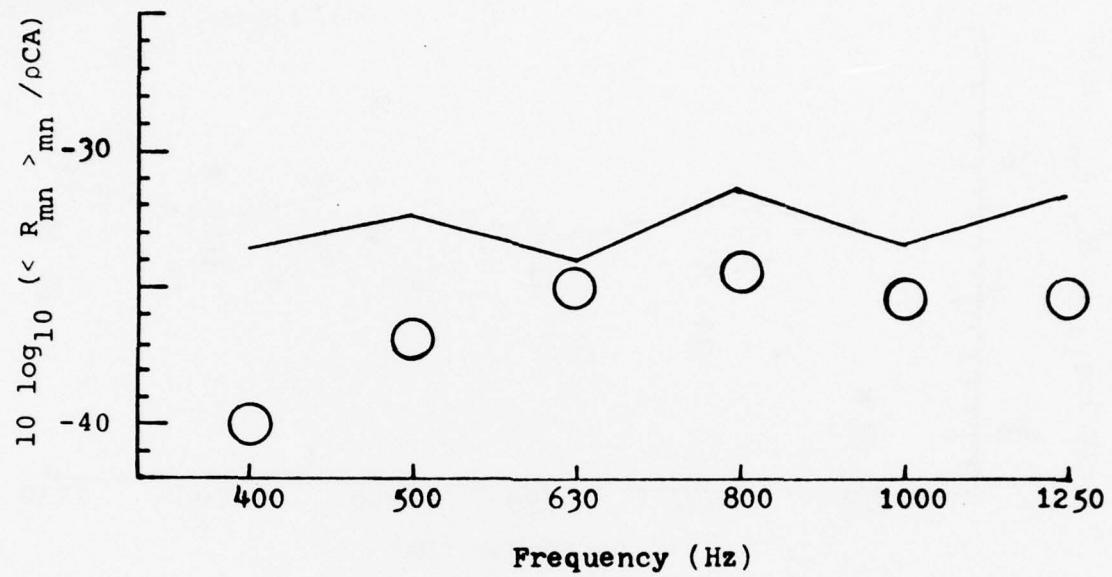


Figure 5.3 Average Radiation Resistance for Resonantly Excited Plate Modes at $M = 0$.
— computed.
O measured.

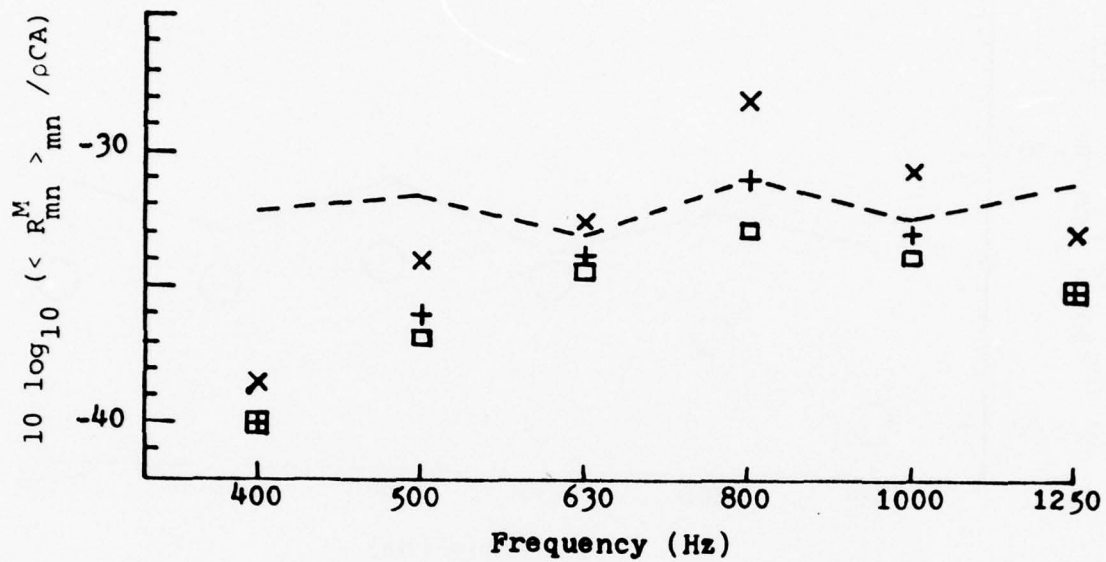


Figure 5.4 Average radiation resistance for resonantly excited plate modes at $M = 0.23$.

Computed : ---

Measured :

Symbol	□	+	x
y^+	128	176	375
y (mm)	0.61	0.61	1.30
u_τ (m/sec)	3.13	4.26	4.26

($y^+ = y u_\tau / v$, see Eq. (5.17))

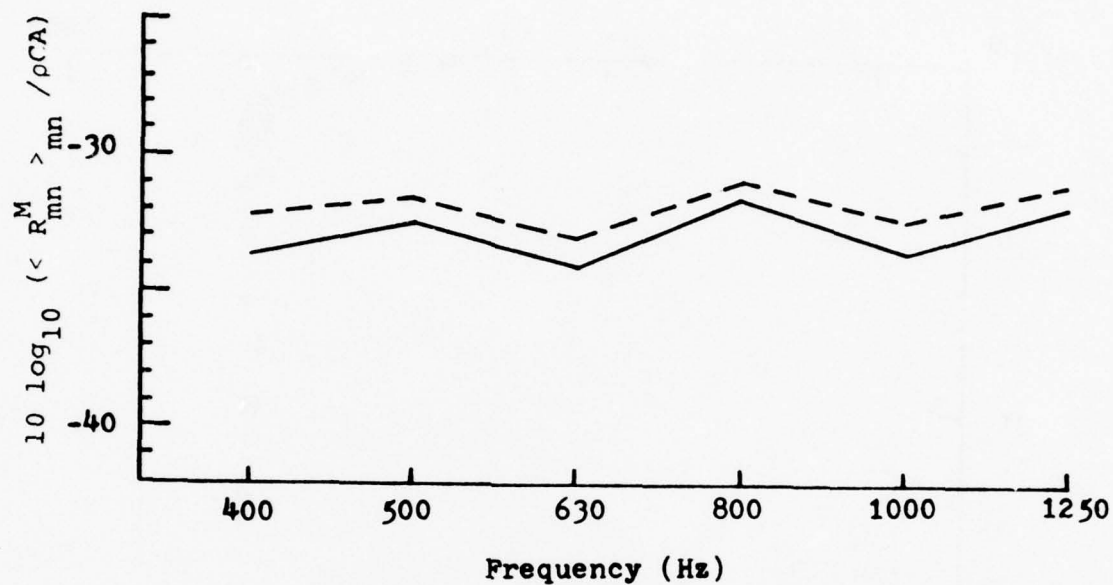


Figure 5.5 Computed Average Radiation Resistance for Resonantly Excited Plate Modes.
 $M = 0.0$: —,
 $M = 0.23$: ---.

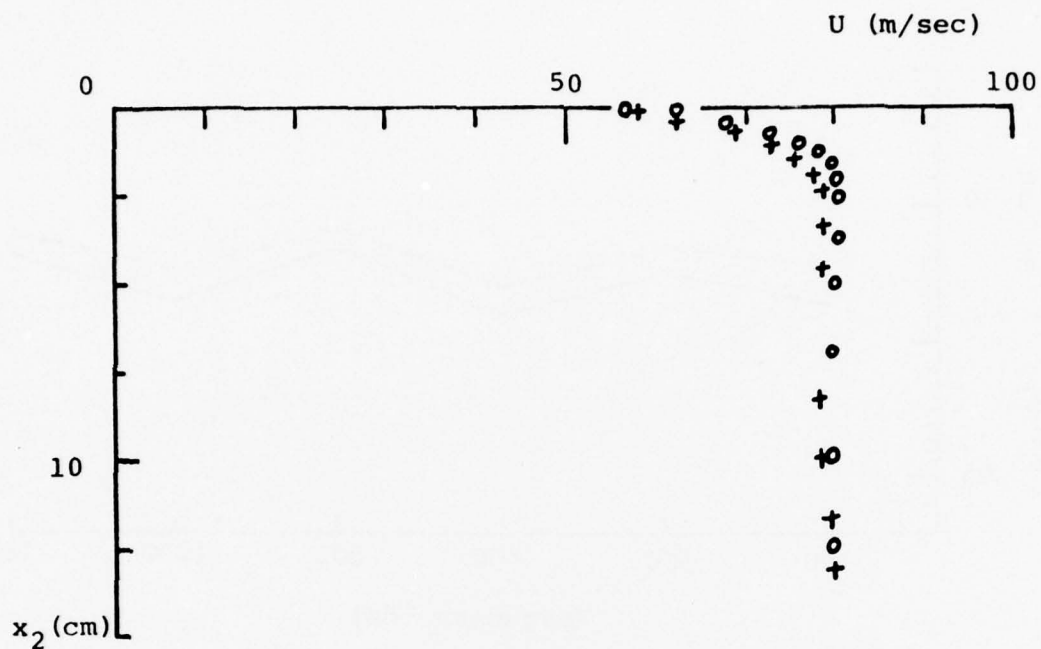


Figure 5.6 Velocity profiles

- 0 : No flow resistance at the inlet of the wind tunnel $u_\tau = 4.26$ m/sec
- + : Polyurethane foam covering the upper half of the wind tunnel inlet. $u_\tau = 3.13$ m/sec

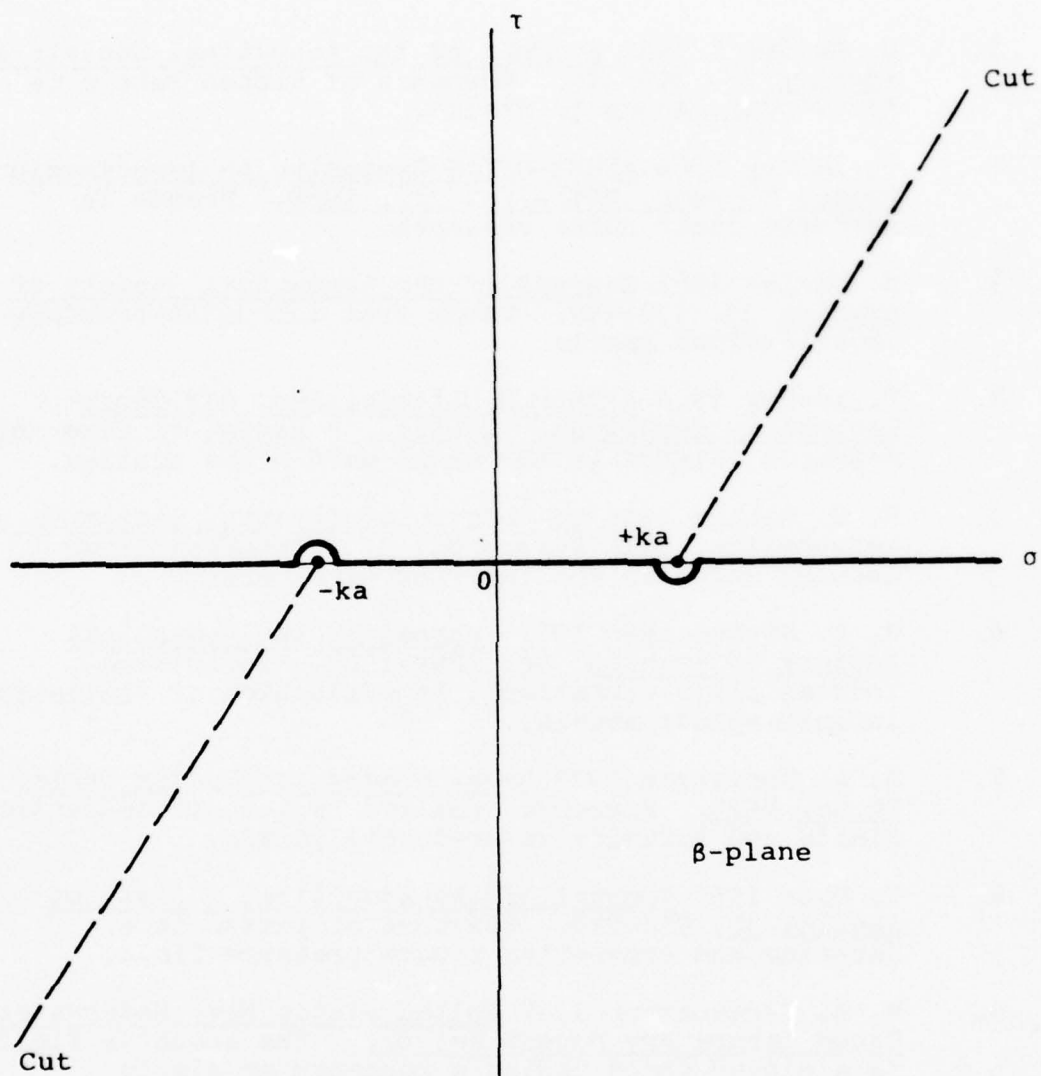


Figure I.1 The Branch Cuts on the β -Plane.

REFERENCES

1. G. Maidanik 1962 Journal of the Acoustical Society of America 34, 809-826. Response of Ribbed Panels to Reverberant Acoustic Fields.
2. P. Leehey 1968 AFOSR-UTIAS Symposium on Aerodynamic Noise, Toronto, 20th-21st May, 1968. Trends in boundary layer noise research.
3. H. Davies 1963 Journal of the Acoustical Society of America 35, 192-199. Sound from turbulent-boundary-layer-excited panels.
4. P. Leehey 1966 Arthur D. Little, Inc. ASW Sonar Technology Report No. 4110366. A review of flow noise research related to the sonar self noise problem.
5. H. S. Ribner 1956 University of Toronto, Institute of Aerophysics, UTIA Report No. 37. Boundary layer induced noise in the interior of aircraft.
6. W. A. Strawderman 1969 Journal of the Acoustical Society of America 46, 1294-1307. Turbulence-induced plate vibrations: An evaluation of finite-and infinite-plate models.
7. R. A. Christman 1973 Naval Underwater System Center, TR No. 4573. Pressure radiated by turbulence-excited finite and infinite water-loaded panels.
8. I. Dyer 1959 Journal of the Acoustical Society of America 31, 922-928. Response of plates to a decaying and convecting random pressure field.
9. W. A. Strawderman 1967 United States Navy Underwater Sound Laboratory Report No. 827. The acoustic field in a closed space behind a rectangular simply supported plate excited by boundary layer turbulence.
10. R. H. Kraichnan 1957 Journal of the Acoustical Society of America 29, 65-80. Noise transmission from boundary layer pressure fluctuations.

11. J. E. Ffowcs Williams and R. H. Lyon 1963 Bolt, Beranek & Newman, Inc. Report No. 1054. The sound radiated from turbulent flows near flexible boundaries.
12. H. Davies and S. Sowayal 1973 Journal of the Acoustical Society of America 54, 1035-1044. Vibration of statically deformed beams and plates.
13. R. Lyon 1956 Journal of the Acoustical Society of America 28, 391-398. Response of a string to random noise fields.
14. L. Sledjeski 1973 Massachusetts Institute of Technology Master Thesis, Department of Ocean Engineering. Sound transmission through a rectangular membrane.
15. H. Davies 1969 Massachusetts Institute of Technology Acoustics & Vibration Laboratory Report No. 71476-1. Acoustic radiation from fluid loaded rectangular plates.
16. P. Morse and K. Ingard 1968 Theoretical Acoustics. The McGraw-Hill, Inc.
17. B. Noble 1958 Methods Based on the Wiener-Hopf Technique. Pergamon Press.
18. C. E. Wallace 1972 Journal of the Acoustical Society of America 51, 946-952. Radiation resistance of a rectangular panel.
19. A. Ralston 1965 A First Course in Numerical Analysis. McGraw-Hill, Inc.
20. B. E. Sandman 1975 Journal of the Acoustical Society of America 57, 1097-1107. Motion of a three-layered elastic-viscoelastic plate under fluid loading.
21. N. C. Martin and P. Leehey 1976 To Be Published. Low wavenumber wall pressure measurements using a rectangular membrane as a spatial filter.

22. C. Hanson 1969 Massachusetts Institute of Technology Acoustics and Vibration Laboratory Report No. 79611-1. The design and construction of a low-noise low-turbulence wind tunnel.
23. W. J. Chyu and M. K. Au-Yang 1973 AIAA Aero-Acoustics Conference, Seattle, Washington. Response of panels to turbulence induced, surface-pressure fluctuations and resulting acoustic radiation to the flow fields.
24. F. Obermeier 1971 Massachusetts Institute of Technology Acoustics and Vibration Laboratory Report No. 70208-6. On the response of elastic plates backed by enclosed cavities to turbulent flow excitations.
25. R. H. Lyon and G. Maidanik 1962 Journal of the Acoustical Society of America 34, 623-639. Power flow between linearly coupled oscillators.

APPENDIX 1

The content of this appendix derives from Noble's book [17]. It is included here for the sake of completeness.

From Eq. (2.12)

$$\frac{\partial^2}{\partial x_2^2} P(\beta, x_2, \omega) - (\beta^2 - k^2 a^2) P(\beta, x_2, \omega) = 0 \quad (2.12)$$

$$P = P_1 e^{-\lambda x_2} + P_2 e^{\lambda x_2}, \quad \lambda = (\beta^2 - k^2 a^2)^{1/2}. \quad (I.1)$$

In this solution there are branch points at $\lambda = \pm ka$. How should the cuts be arranged in the β -plane so that Eq. (I.1) represents a solution of Eq. (2.12) which can be inverted to give $P(x, x_2, \omega)$?

We have already implicitly assumed:

(a) For any given x_2 , $P(\beta, x_2, \omega)$ exists in a certain strip $c < \tau < d$, $-\infty < \sigma < \infty$ of the β -plane.

We make the further assumption:

(b) $P(\beta, x_2, \omega)$ is bounded as $x_2 \rightarrow \infty$ for all β in the strip $c < \tau < d$.

If we cut the β -plane by straight lines from $\beta = \pm ka$ to infinity, both of the straight lines going to infinity in the lower half-plane, then it will be necessary to invert Eq. (I.1) for a value of τ , say τ_0 , such that $\tau_0 < k_2$. But in this case it

can be proved by analytic continuation that if we choose the branch of λ such that $\lambda \rightarrow |\beta|$ as $\sigma \rightarrow \infty$, $\beta = \sigma + i\tau_0$, then $\lambda \rightarrow -|\beta|$ as $\beta \rightarrow -\infty$. Thus, in Eq. (I.1) it will not be possible to choose P_1 and P_2 such that $P(\beta, x_2, \omega)$ is bounded as $x_2 \rightarrow \infty$ for all β on the line $\beta = \sigma + i\tau_0$. A similar argument holds if we cut the plane by two lines both of which go to infinity in the upper half-plane or if we cut the plane by a straight line joining $+ka$ to $-ka$. The only remaining possibility is to cut the β -plane by a line from $+ka$ to infinity in the upper half-plane and $-ka$ to infinity in the lower half-plane as in Figure I.1. By analytic continuation we have that $\lambda \rightarrow +|\beta|$ as $\sigma \rightarrow +\infty$ so that Eq. (I.1) represents a solution satisfying condition (b) if we take $P_2 = 0$. This is

$$P(\beta, x_2, \omega) = P_1 e^{-\lambda x_2} \quad (2.13)$$

With these specified branches, we see that

$$(ka - \beta)^{1/2} = i \sqrt{\beta - ka}$$

$$(-ka - \beta)^{1/2} = -i \sqrt{\beta + ka}$$

everywhere in the cut plane, and that

$$\gamma = \begin{cases} + \sqrt{\sigma^2 - k^2 a^2} & \sigma > ka \\ - i \sqrt{k^2 a^2 - \sigma^2} & -ka < \sigma < ka \\ + \sqrt{\sigma^2 - k^2 a^2} & \sigma < -ka \end{cases}$$

on the real axis in the β -plane.

APPENDIX II

Subroutine SIGCHI (see listing at end of Appendix)

Purpose

SIGCHI computes the radiation impedance expressed in Eq. (2.32).

Usage

CALL SIGCHI (M,N,P,Q,IMAREA,R,VMACH,K,RADIMP,IER1,IER2,NO)

M,N,P,Q, Modal numbers for the modes (m,n) and (p,q).

M = m, N = n, P = p, Q = q,

IMAREA Given option for selection of operation

= 1, compute the non-dimensional modal coupling resistance, σ_{mnpq}^M .

= -1, compute the non-dimensional modal coupling reactance, χ_{mnpq}^M .

R Aspect ratio = ℓ_1/ℓ_3 ,

ℓ_1, ℓ_3 are panel dimensions with ℓ_1 being parallel to the flow direction.

VMACH Mach number of mean flow.

K Non-dimensional acoustic wave number = $k\ell_1$.

RADIMP Resultant data, σ_{mnpq}^M or χ_{mnpq}^M depending upon the value of IMAREA.

IER1,IER2 Resultant Romberg quadrature error parameters.

IER1 = The number of times when it is impossible to reach the required accuracy because of rounding errors.

IER2 = The number of times when the required accuracy could not be reached within (NROMB-1) steps, NROMB should be increased.

Required accuracy ROMB = 1×10^{-4} can be varied on Card RADC0073.

NROMB = 15 can be varied on Card RADC0074.

NO Order of the Chebychev quadrature.

If NO = 3 x NCHEB, it is possible that the required accuracy was not achieved.

NCHEB should be increased.

Required accuracy CHEB = 1×10^{-2} can be varied on Card RADC0071.

NCHEB = 729 can be varied on Card RADC0072.

SIGC0001
SIGC0002
SIGC0003
SIGC0004
SIGC0005
SIGC0006
SIGC0007
SIGC0008
SIGC0009
SIGC0010
SIGC0011
SIGC0012
SIGC0013
SIGC0014
SIGC0015
SIGC0016
SIGC0017
SIGC0018
SIGC0019
SIGC0020
SIGC0021
SIGC0022
SIGC0023

C
C
1 SUBROUTINE SIGCHI (M1,N1,P1,Q1,IMARE1,R1,VHACH,K1,RADIMP,
IERA,IERB,NO1)
REAL K,K1
INTEGER F,Q,P1,Q1
COMMON /ECHAIN/K,M,N,P,C,IER1,IER2,IMAREA/RAHAIN/NO/EGHAIN/R
K=K1
N=N1
N=N1
P=P1
C=Q1
R=R1
IMAREA=IMARE1
IER1=0
IER2=0
CALL RADCOF (M,N,P,Q,R,VHACH,K,IMAREA,RADIMP)
NC1=NO
IERA=IER1
IERB=IER2
RETURN
END
C

RADC0001
RADC0002
RADC0003
RADC0004
RADC0005
RADC0006
RADC0007
RADC0008
RADC0009
RADC0010
RADC0011
RADC0012
RADC0013
RADC0014
RADC0015
RADC0016
RADC0017
RADC0018
RADC0019
RADC0020
RADC0021
RADC0022
RADC0023
RADC0024
RADC0025
RADC0026
RADC0027
RADC0028
RADC0029
RADC0030
RADC0031
RADC0032
RADC0033
RADC0034
RADC0035
RADC0036

```

C      M,N,P,Q ARE MODAL NUMBERS. M,P ARE IN X1 DIRECTION. P,Q IN X3.
C      R=L1/L3. RADIMP IS THE RADIATION IMPEDANCE ( REAL PART OR
C      IMAGINARY PART) TO BE COMPUTED FOR THE MODES (M,N) AND (P,Q).
C      IMAREA=+1 MEANS REAL PART OF RADIATION IMPEDANCE WILL BE COMPUTED
C      IMAREA=-1 MEANS IMAGINARY OF RADIATION IMPEDANCE WILL BE COMPUTED
C      K IS THE ACOUSTIC WAVE NUMBER/L1. IER1 & IER2 ARE ERROR MESSAGE
C      FOR ROMBERG SUBROUTINE.
C      ALSO NOTE: KMN=KM**2+KN**2=PI*(M**2+(N*R)**2)**.5
C
C      SUBROUTINE RADCOF(M,N,P,Q,R,VMACH,K,IMAREA,RADIMP)
C
C      INTEGER P,Q,P1,Q1
C      REAL KM,KMSQ,KP,KPSQ,KN,KNSQ,KQ,KQSQ,HN,HNSQ,HQ,HQSQ,K,KSQ,HALFPI
C
C      COMMON /ERAD/KNSQ,BA,BOBB,NRCMB,D,R4DK,TLK
C      COMMON /GRAD/M1,N1,KPSQ,HNSQ,HQSQ,CMHTLK,OMACHR,TLKM
C      COMMON /EAMAIN/NO
C      COMMON /EGRAD/KMSQ
C
C      DATA PI/3.14159265/
C      DATA HALFPI/1.5707963/
C
C      IMAREA HAS TO BE EITHER 1 OR -1.
C      IF (IMAREA.EQ.-1.OR.IMAREA.EQ.+1) GO TO 66
C      RADIMP=-.12345E67
C      RETURN
C
C      PARITY CHECK: COMPUTE ONLY IF (M+P) AND (N+Q) ARE EVEN. OTHERWISE,
C      RADIMP(M,N,P,Q)=0
C
C      M1=MOD(M,2)
66

```

RADC0037
RADC0038
RADC0039
RADC0040
RADC0041
RADC0042
RADC0043
RADC0044
RADC0045
RADC0046
RADC0047
RADC0048
RADC0049
RADC0050
RADC0051
RADC0052
RADC0053
RADC0054
RADC0055
RADC0056
RADC0057
RADC0058
RADC0059
RADC0060
RADC0061
RADC0062
RADC0063
RADC0064
RADC0065
RADC0066
RADC0067
RADC0068
RADC0069
RADC0070
RADC0071
RADC0072

P1=MOD(E,2)
N1=MOD(N,2)
Q1=MOD(Q,2)
IF (M1.NE.P1.OR.N1.NE.Q1) GC TC 999

C
C
C
C

EVALUATE SOME FREQUENTLY USED CONSTANTS.

KH=N
KH=KH*PI
KMSQ=KH**2

C

KP=P
KP=KP*PI
KPSQ=KP**2

C

HN=N
HN=HN*PI
HMSQ=HN**2
KN=HN**R
KNSQ=KN**2

C

HQ=Q
HQ=HQ*PI
HQSQ=HQ**2
KQ=HQ**R
KQSQ=KQ**2
CMACH2=1.-VMACH**2
CMACHR=SQRT(CMACH2)
TLK=K/ONACHR
CHHTLK=VMACH/TLK
TLKN=TLK*VMACH

C
C

CH2B,RCMB: ERROR TOLERANCE. NCHEB,NROMB: ORDER OF QUADRATURES.
CHEB=1.E-2
NCHEB=729


```

ROMB=1.E-4
NROMB=15
507 CONTINUE
C
KSQ=K**2
FACTOR=H**N**P*Q
FACTOR=FACTOR*KSQ*315.828/R/CMACH2**3
C
E4DK=R**4/TLK
EA=TLK**2.
BA=AMAX1(KM,KN,KP,KQ,EA)*2.E0
C
C
C TO INTEGRATE INTEGRAL WITH SQUARE ROOT SINGULARITY, 1/(1-X**2)**.5,
C BY CHEBYCHEV GAUSS QUADRATURE ( SEE A. RALSTON, P98.)
C
SUN=E(0.0)/2.0
D=SUN
NC=1
C
C
1 NO=NO*3
DNO=NO
DNO=DNO/HALFPI
C
C
DO 9 JP=1,NO,2
IF (MOD(JP,3).EQ.0) GO TO 9
C
DJP=JP
AJP=COS(DJP/DNO)
SUM=SUM+E(AJP)
9 CONTINUE
C
C

```

RADC0073
RADC0074
RADC0075
RADC0076
RADC0077
RADC0078
RADC0079
RADC0080
RADC0081
RADC0082
RADC0083
RADC0084
RADC0085
RADC0086
RADC0087
RADC0088
RADC0089
RADC0090
RADC0091
RADC0092
RADC0093
RADC0094
RADC0095
RADC0096
RADC0097
RADC0098
RADC0099
RADC0100
RADC0101
RADC0102
RADC0103
RADC0104
RADC0105
RADC0106
RADC0107
RADC0108

RADC0109
RADC0110
RADC0111
RADC0112
RADC0113
RADC0114
RADC0115
RADC0116
RADC0117
RADC0118
RADC0119
RADC0120
RADC0121

```

          LCID=L
          D=SUN/DNO*2.0
          IF (ABS(1.E0-DOLD/D) .LT. CHEB.OR.NO.GT. NCHEB) GO TO 10
C
          GO TO 1
C
          10 CCNTINUE
          RADIMP=D*FACTOR
          RETURN
          RADIMP=0.0
          RETURN
          END
C
          999

```

E, DEFINED BELOW, DEVIDEC BY (1-AJP**2)**.5 IS THE INTEGRAND.

FUNCTION E (AJP)

REAL HALPPI,K,KMSQ,KMSQ
INTEGER I,Q

EXTERNAL GCT

DIMENSION AUX (15), BOX (15)

COMMON /BMAIN/K,M,N,P,Q,IER1,IER2,IMAREA
COMMON /ERAD/KNSQ,BA,5OMB,NOMB,I,R4LK,TLK
COMMON /EGMAIN/R
COMMON /EGRAD/KMSQ
COMMON /EGCT/TLB

DATA PI/3.14159265/
DATA HALFPI/1.5707963/

```

IF (AJP.EQ.0.F0) GO TO 2
IF (IMAREA .GT. 0) GO TC 3
TLB=TLK/AJP
IF (TLB.LT.BA) GO TO 1
B4=.5E0/TLB**4
E7=.4E0/TLB**7
IF (N.EQ.F) COMPAR=B4/KESQ
IF (N.NE.P) COMPAR=B7
IF (N.EQ.Q) COMPAR=B4/KESQ+CMPARF
IF (N.NE.Q) COMPAR=B7+CMPAR
COMPAR=ABS(D/COMPAR/R4DK)

```

E0000037
E0000038
E0000039
E0000040
E0000041
E0000042
E0000043
E0000044
E0000045
E0000046
E0000047
E0000048
E0000049
E0000050
E0000051
E0000052
E0000053
E0000054

```

C      IF (CCHPAE.GT.1.E04) GO TO 2
1      CALL ROMBG(0.E0,PI,ROMB,NROMB,GCT,E,IER,AUX,BUX)
      E=E/AJP**2
      IF (IER.EQ.1) IER1=IER1+1
      IF (IER.EQ.2) IER2=IER2+1
      RETURN
C
2      E=0.E0
      RETURN
C
3      TLB=TLK*AJP
      CALL ROMBG(0.E0,PI,RCHE,NROMB,GCT,E,IER,AUX,BUX)
      E=E*AJP
      IF (IER.EQ.1) IER1=IER1+1
      IF (IER.EQ.2) IER2=IER2+1
      RETURN
      END

```

```

C
C
SUBROUTINE ROMBG (XL, XU, EPS, NDIM, PCT, Y, IER, AUX, BUX)
REAL H, HH, HD
DIMENSION AUX(1), BUX(1)

C
C
PREPARATIONS OF ROMBERG-LOOP
AUX(1) = .5E0 * (PCT(XL) + PCT(XU))
BUX(1) = PCT((XL+XU)/2.E0)
YNEW = (AUX(1) + BUX(1)) / 2.E0
H = XU - XL
IF (NDIM-1) 8, 8, 1
1 IF (H) 2, 10, 2
C
C
NDIM IS GREATER THAN 1 AND H IS NOT EQUAL TO 0.
2 HH = H/2.E0
DELT2 = 0.
P = 1.E0
JJ = 2
DO 7 I = 2, NDIM
Y = YNEW
DELT1 = DELT2
HD = HH
HH = .5E0 * HH
AUX(I) = .5E0 * (AUX(I-1) + BUX(I-1))
P = .5E0 * P
X = XL + HH
BUX(I) = 0.E0
LC 3 J = 1, JJ
EUX(I) = EUX(I) + PCT(X)
3 X = X + HD
EUX(I) = EUX(I) * P
A NEW APPROXIMATION OF INTEGRAL VALUE IS COMPUTED BY MEANS OF
TRAPEZOIDAL RULE.
C
C
START OF ROMBERGS EXTRAECIATION METHCD.
C

```

ROMB0001
ROMB0002
ROMB0003
ROMB0004
ROMB0005
ROMB0006
ROMB0007
ROMB0008
ROMB0009
ROMB0010
ROMB0011
ROMB0012
ROMB0013
ROMB0014
ROMB0015
ROMB0016
ROMB0017
ROMB0018
ROMB0019
ROMB0020
ROMB0021
ROMB0022
ROMB0023
ROMB0024
ROMB0025
ROMB0026
ROMB0027
ROMB0028
ROMB0029
ROMB0030
ROMB0031
ROMB0032
ROMB0033
ROMB0034
ROMB0035
ROMB0036

ROMB0037
ROMB0038
ROMB0039
ROMB0040
ROMB0041
ROMB0042
ROMB0043
ROMB0044
ROMB0045
ROMB0046
ROMB0047
ROMB0048
ROMB0049
ROMB0050
ROMB0051
ROMB0052
ROMB0053
ROMB0054
ROMB0055
ROMB0056
ROMB0057
ROMB0058
ROMB0059
ROMB0060
ROMB0061

```

Q=1.E0
JI=I-1
DO 4 J=1,JI
  II=I-J
  Q=Q+Q
  Q=Q+Q
  BUX(II)=BUX(II+1)+(BUX(II+1)-BUX(II))/(Q-1.E0)
  4 AUX(II)=AUX(II+1)+(AUX(II+1)-AUX(II))/(Q-1.E0)
  END OF ROMBERG-STEP
C
C
  YNEW=(AUX(1)+BUX(1))/2.E0
  DELT2=ABS(Y-YNEW)
  IF(I-5) 7,5,5
  5 IF(DELT2/ABS(Y)-EPS) 10,10,6
  6 IF(DELT2-DELT1) 7,11,11
  7 JJ=JJ+JJ
  8 IER=2
  9 Y=H*YNEW
  RETURN
10 IER=0
  GC TO 9
11 IER=1
  Y=H*Y
  RETURN
  END

```

C C C

```
FUNCTION GCT(TH)
  REAL KMSQ,KPSQ,HNSQ,HQSQ
  COMMON /GRAD/M1,M1,KPSQ,HNSQ,HQSQ,OMHTLK,OMACHR,TLKM
  COMMON /EGMAIN/R
  COMMON /EGRAD/KMSQ
  COMMON /EGCT/TLB
  TLB1=TLB*COS(TH)
  E1=(TLB1-TLKM)/OMACHR
  B3=TLB*SIN(TH)/R
  GCT=PCN(M1,B1,KMSQ,KPSQ)*PCN(N1,B3,HNSQ,HQSQ)*(1.-TLB1*OMHTLK)**2
  RETURN
END
```

GCT00001
GCT00002
GCT00003
GCT00004
GCT00005
GCT00006
GCT00007
GCT00008
GCT00009
GCT00010
GCT00011
GCT00012
GCT00013
GCT00014
GCT00015

[illegible]

RETURN

PCN= (2.020-ABSB/K1) / 16.CEO/K1SQ

RETURN

END

PCN000037
PCN000038
PCN000039
PCN000040
PCN000041
PCN000042

BIOGRAPHIC NOTES

Yi Mason Chang, born in Shantong, China in 1948, was raised in Taiwan. He attended undergraduate school at Cheng Kung University, Tainan, Taiwan, receiving a Bachelor of Science in Engineering in June 1969. From 1970 to 1972 he studied electrical and oceanographic sciences at the State University of New York at Stony Brook and earned a Master Degree in Electrical Sciences in August 1971. From 1972 to 1976 he attended the Ocean Engineering Department at M.I.T. in September 1972 receiving a Master Degree in February 1974. His thesis was in the area of the response of panels to turbulent boundary layer pressure fluctuations.

M.I.T., A & V Report 82464-1

The Mean Flow Effect on the Acoustic Impedance of a Rectangular Panel, by Yi Mason Chang, February 1977, 136 pgs., illustrated. UNCLASSIFIED

In better understanding the coupling between a vibrating panel and its surrounding acoustic medium, a precise knowledge of both the real and the imaginary parts of the radiation impedance is of critical value.

The modal radiation impedance of a rectangular panel simply supported in an infinite baffle in the presence of an inviscid, uniform, subsonic flow is studied. The analysis is based on an expansion in normal modes of the transverse vibration displacement field of the panel and the use of the wave number frequency transforms. These are used to formulate the expressions for the modal radiation impedance, and the cross modal coupling impedance.

A computer program was formulated to evaluate the modal radiation impedances. A modified Chebychev quadrature served as a major ingredient. Experiments performed were compared with the analytical results. Some experiments showed larger increases in the panel radiation resistance due to flow speed than would be predicted by the present linear theory.

Panel
Vibration

Acoustic
Radiation

Added
Mass

M.I.T., A & V Report 82464-1

The Mean Flow Effect on the Acoustic Impedance of a Rectangular Panel, by Yi Mason Chang, February 1977, 136 pgs., illustrated. UNCLASSIFIED

In better understanding the coupling between a vibrating panel and its surrounding acoustic medium, a precise knowledge of both the real and the imaginary parts of the radiation impedance is of critical value.

The modal radiation impedance of a rectangular panel simply supported in an infinite baffle in the presence of an inviscid, uniform, subsonic flow is studied. The analysis is based on an expansion in normal modes of the transverse vibration displacement field of the panel and the use of the wave number frequency transforms. These are used to formulate the expressions for the modal radiation impedance, and the cross modal coupling impedance.

A computer program was formulated to evaluate the modal radiation impedances. A modified Chebychev quadrature served as a major ingredient. Experiments performed were compared with the analytical results. Some experiments showed larger increases in the panel radiation resistance due to flow speed than would be predicted by the present linear theory.

Panel
Vibration

Acoustic
Radiation

Added
Mass

M.I.T., A & V Report 82464-1

The Mean Flow Effect on the Acoustic Impedance of a Rectangular Panel, by Yi Mason Chang, February 1977, 136 pgs., illustrated. UNCLASSIFIED

In better understanding the coupling between a vibrating panel and its surrounding acoustic medium, a precise knowledge of both the real and the imaginary parts of the radiation impedance is of critical value.

The modal radiation impedance of a rectangular panel simply supported in an infinite baffle in the presence of an inviscid, uniform, subsonic flow is studied. The analysis is based on an expansion in normal modes of the transverse vibration displacement field of the panel and the use of the wave number frequency transforms. These are used to formulate the expressions for the modal radiation impedance, and the cross modal coupling impedance.

A computer program was formulated to evaluate the modal radiation impedances. A modified Chebychev quadrature served as a major ingredient. Experiments performed were compared with the analytical results. Some experiments showed larger increases in the panel radiation resistance due to flow speed than would be predicted by the present linear theory.

Panel
Vibration

Acoustic
Radiation

Added
Mass

M.I.T., A & V Report 82464-1

The Mean Flow Effect on the Acoustic Impedance of a Rectangular Panel, by Yi Mason Chang, February 1977, 136 pgs., illustrated. UNCLASSIFIED

In better understanding the coupling between a vibrating panel and its surrounding acoustic medium, a precise knowledge of both the real and the imaginary parts of the radiation impedance is of critical value.

The modal radiation impedance of a rectangular panel simply supported in an infinite baffle in the presence of an inviscid, uniform, subsonic flow is studied. The analysis is based on an expansion in normal modes of the transverse vibration displacement field of the panel and the use of the wave number frequency transforms. These are used to formulate the expressions for the modal radiation impedance, and the cross modal coupling impedance.

A computer program was formulated to evaluate the modal radiation impedances. A modified Chebychev quadrature served as a major ingredient. Experiments performed were compared with the analytical results. Some experiments showed larger increases in the panel radiation resistance due to flow speed than would be predicted by the present linear theory.

Panel
Vibration

Acoustic
Radiation

Added
Mass

DISTRIBUTION LIST

- 7 Commander
Naval Ship Research & Development
Center
Washington, D.C. 20034
ATTN: Mr. Gerald J. Franz, Code 149
Dr. Gideon Maidanik, Code 1902
Dr. W. B. Morgan, Code 154
Dr. Frank B. Peterson, Code 1552
Dr. John T. C. Shen, Code 1942
Dr. Murray Strasberg, Code 1901
Dr. William K. Blake, Code 1942
- 1 Officer-in-Charge
Annapolis Laboratory
Naval Ship Research and
Development Center
Annapolis, Maryland 21402
ATTN: Code 522.3 (Library)
- 7 Commander
Naval Sea Systems Command
Washington, D.C. 20362
ATTN: SEA 09G32 (3 copies)
SEA 03512 (Peirce)
SEA 037
SEA 0322
SEA 033
- 12 Director
Defense Documentation Center
5010 Duke Street
Alexandria, Virginia 22314
- 3 Office of Naval Research
800 North Quincy Street
Arlington, Virginia 22217
ATTN: Mr. R. D. Cooper, Code 438
Mr. H. M. Fitzpatrick, Code 222 (2 copies)
- 1 Office of Naval Research
Branch Office
492 Summer Street
Boston, Massachusetts 02210
- 1 Office of Naval Research
Branch Office (493)
536 South Clark Street
Chicago, Illinois 60605
- 1 Chief Scientist
Office of Naval Research
Branch Office
1030 East Green Street
Pasadena, California 91106

- 1 Office of Naval Research
Resident Representative
715 Broadway (5th floor)
New York, New York 10003
- 1 Office of Naval Research
San Francisco Area Office
760 Market Street
Room 447
San Francisco, California 94102
- 2 Director
Naval Research Laboratory
Washington, D.C. 20390
ATTN: Code 2027
Code 2629 (ONRL)
- 1 Commander
Naval Facilities Engineering
Command (Code 032C)
Washington, D.C. 20390
- 1 Library of Congress
Science and Technical Division
Washington, D.C. 20540
- 1 Professor S. A. Elder
Division of Mathematics and Science
U.S. Naval Academy
Annapolis, Maryland 21402
- 1 National Science Foundation
Engineering Division Library
1800 G Street, N.W.
Washington, D.C. 20550
- 8 Commander
Naval Ship Engineering Center
Center Building
Prince Georges Center
Hyattsville, Maryland 20782
ATTN: SEC 6034B
SEC 6110
SEC 6114H
SEC 6120
SEC 6136
SEC 6144G
SEC 6140B
SEC 6148
- 2 Stanford University
Stanford, California 94305
ATTN: Engineering Library
Dr. R. Street
- 1 Library (Code 1640)
Naval Oceanographic Office
Washington, D.C. 20390

- 1 Technical Library
Naval Proving Ground
Dehlgren, Virginia 22448
- 1 Commander (ADL)
Naval Air Development Center
Warminster, Pennsylvania 18974
- 3 Commander
Naval Undersea Research &
Development
San Diego, California 92137
ATTN: Dr. Andrew G. Fabula, Code 4007
Dr. Tibor G. Horwath, Code 6002
Mr. Howard V. L. Patrick, Code 6005
- 3 Officer in Charge
Pasadena Laboratory
Naval Undersea Research &
Development Center
3202 East Foothill Boulevard
Pasadena, California 91107
ATTN: Mr. James M. Caraher, Code 2542
Dr. Jack W. Hoyt, Code 2501
Mr. Arnold O. Musolf, Code 2541
- 1 Director
Naval Research Laboratory
Underwater Sound Reference Division
P.O. Box 8337
Orlando, Florida 32806
- 3 Commander
Naval Underwater Systems Center
Newport, Rhode Island 02840
ATTN: Mr. J. F. Brady, Code TB
Mr. R. M. Dunlop, Code PA1
Mr. R. H. Nadolink, Code TB141
- 1 Commanding Officer
Naval Torpedo Station
Keyport, Washington 98354
ATTN: Dr. W. A. Middleton, Code 702
- 2 Commander
Naval Ordnance Laboratory
White Oak
Silver Spring, Maryland 20901
ATTN: Mr. Robert B. Knowles, Code 053
Mr. Charles B. Leslie, Code 221
- 1 Library
Naval Underwater Systems Center
Newport, Rhode Island 02840

- 2 National Bureau of Standards
Washington, D.C. 20234
ATTN: P. S. Klebanoff (FM-105)
Chief, Aerodynamics Division
K. D. Tidstrom
- 1 AFOSR/NAM
1400 Wilson Boulevard
Arlington, Virginia 22209
- 1 AFFOL/FYS (J. Olsen)
Wright Patterson AFB
Dayton, Ohio 45433
- 1 Department of Transportation
Library TAD-491.1
400 7th Street, S.W.
Washington, D.C. 20590
- 1 Charleston Naval Shipyard
Technical Library
Naval Base
Charleston, South Carolina 29408
- 1 Norfolk Naval Shipyard
Technical Library
Portsmouth, Virginia 23709
- 1 Philadelphia Naval Shipyard
Philadelphia, Pennsylvania 19112
ATTN: Code 240
- 1 Portsmouth Naval Shipyard
Technical Library
Portsmouth, New Hampshire 03801
- 1 Puget Sound Naval Shipyard
Engineering Library
Bremerton, Washington 98314
- 1 Long Beach Naval Shipyard
Technical Library 246LO
Long Beach, California 90801
- 1 Hunters Point Naval Shipyard
Technical Library (Code 202.3)
San Francisco, California 94135
- 1 Pearl Harbor Naval Shipyard
Code 202.32
Box 400, FPO
San Francisco, California 96610
- 1 Mare Island Naval Shipyard
Shipyard Technical Library
Code 202.3
Vallejo, California 94592

- 1 Assistant Chief, Design Engineering
for Naval Architecture
Code 250
Mare Island Naval Shipyard
Vallejo, California 94592
- 3 U.S. Naval Academy
Annapolis, Maryland 21402
ATTN: Technical Library
Dr. Bruce Johnson
Prof. P. Van Mater, Jr.
- 3 Naval Postgraduate School
Monterey, California 93940
ATTN: Library, Code 2124
Dr. T. Sarpkaya
Prof. J. Miller
- 2 The Pennsylvania State University
Applied Research Laboratory
P.O. Box 30
State College, Pennsylvania 16801
ATTN: Library
Dr. E. J. Skudrzyk
- 1 Bolt Beranek and Newman
1501 Wilson Boulevard
Arlington, Virginia 22209
ATTN: Dr. F. Jackson
- 1 University of Minnesota
Minneapolis, Minnesota 55455
ATTN: Prof. R. F. Lambert
- 1 Cambridge Acoustical Associates, Inc.
1033 Massachusetts Avenue
Cambridge, Massachusetts 02138
ATTN: Dr. M. Junger
- 1 Mr. V. Boatwright, Jr.
R & D Manager
Electric Boat Division
General Dynamics Corporation
Groton, Connecticut 06340
- 1 Professor E. L. Mollo-Christensen
Department of Meteorology
Room 54-1715
Massachusetts Institute of Technology
Cambridge, Massachusetts 02139
- 1 Gibbs and Cox, Inc.
21 West Street
New York, New York 10006
ATTN: Technical Information Control

- 1 Hydronautics, Inc.
Pindell School Road
Howard County
Laurel, Maryland 20810
ATTN: Library
- 2 McDonnell Douglas Aircraft Co.
3855 Lakewood Boulevard
Long Beach, California 90801
ATTN: J. Hess
T. Cebeci
- 1 Lockheed Missiles & Space Co.
P.O. Box 504
Sunnyvale, California 94088
ATTN: Mr. R. L. Waid
Dept. 57-74
Bldg. 150
Facility 1
- 1 Newport News Shipbuilding and
Dry Dock Company
4101 Washington Avenue
Newport News, Virginia 23607
ATTN: Technical Library
- 1 North American Aviation, Inc.
Space and Information Systems Division
12214 Lakewood Boulevard
Downey, California 90241
ATTN: Mr. B. Ujihara (SL-20)
- 1 Oceanics, Inc.
Technical Industrial Park
Plainview, L.I., New York 11803
- 1 Society of Naval Architects and
Marine Engineers
74 Trinity Place
New York, New York 10006
ATTN: Technical Library
- 1 Sperry Systems Management Division
Sperry Rand Corporation
Great Neck, New York 11020
ATTN: Technical Library
- 1 Applied Research Laboratory Library
University of Texas
P.O. Box 8029
Austin, Texas 78712
- 1 Stanford Research Institute
Menlo Park, California 94025
ATTN: Library G-021

- 2 Southwest Research Institute
P.O. Drawer 28510
San Antonio, Texas 79294
ATTN: Applied Mechanics Review
Dr. H. Abramson
- 1 Tracor, Inc.
6500 Tracor Lane
Austin, Texas 78721
- 1 Ocean Engineering Department
Woods Hole Oceanographic Institution
Woods Hole, Massachusetts 02543
- 1 Worcester Polytechnic Institute
Alden Research Laboratories
Worcester, Massachusetts 01609
ATTN: Technical Library
- 1 University of Bridgeport
Bridgeport, Connecticut 06602
ATTN: Dr. E. Uram
- 1 Applied Physics Laboratory
University of Washington
1013 N.E. 40th Street
Seattle, Washington 98105
ATTN: Technical Library
- 1 Cornell University
Graduate School of Aerospace Engineering
Ithaca, New York 14850
ATTN: Prof. W. R. Sears
- 4 University of California
College of Engineering
Berkeley, California 94720
ATTN: Library
Prof. J. Wehausen
Prof. W. Webster
Prof. J. Paulling
- 4 California Institute of Technology
Pasadena, California 91109
ATTN: Aeronautics Library
Dr. T. Y. Wu
Dr. A. J. Acosta
Dr. F. Marble
- 1 Docs/Repts/Trans Section
Scripts Institute of Oceanography Library
University of California, San Diego
P.O. Box 2369
La Jolla, California 92037

- 1 Catholic University of America
Washington, D.C. 20017
ATTN: Dr. A. B. Magrab
Department of Civil and
Mechanical Engineering
- 1 Colorado State University
Foothills Campus
Fort Collins, Colorado 80521
ATTN: Reading Room, Engineering Research
Center
- 2 University of California at San Diego
La Jolla, California 92038
ATTN: Dr. A. T. Ellis
Dr. J. W. Miles
- 1 Harvard University
Pierce Hall
Cambridge, Massachusetts 02139
ATTN: Library
- 3 Institute of Hydraulic Research
The University of Iowa
Iowa City, Iowa 52240
ATTN: Library
Dr. L. Landweber
Dr. J. Kennedy
- 2 College of Engineering
University of Notre Dame
Notre Dame, Indiana 46556
ATTN: Engineering Library
Dr. Strandhagen
- 2 Parsons Laboratory
Massachusetts Institute of Technology
Cambridge, Massachusetts 02139
ATTN: C. C. Mei
- 1 St. Anthony Falls Hydraulic Laboratory
University of Minnesota
Minneapolis, Minnesota 55414
- 2 Department of Naval Architecture and
Marine Engineering
University of Michigan
Ann Arbor, Michigan 48104
ATTN: Library
Dr. T. F. Ogilvie
- 2 Massachusetts Institute of Technology
Department of Mechanical Engineering
Cambridge, Massachusetts 02139
ATTN: Prof. R. H. Lyon, Room 3-364
Prof. S. H. Crandall, Room 3-362

- 2 New York University
University of Heights
Bronx, New York 10453
ATTN: Prof. W. Pierson, Jr.
- 2 Department of Aerospace and Mechanical Sciences
Princeton University
Princeton, New Jersey 08540
ATTN: Prof. G. Mellor
Prof. E. H. Dowell
- 3 Davidson Laboratory
Stevens Institute of Technology
711 Hudson Street
Hoboken, New Jersey 07030
ATTN: Library
Prof. J. Breslin
Dr. S. Tsakonas
- 1 Department of Mathematics
St. John's University
Jamaica, New York 11432
- 3 Webb Institute of Naval Architecture
Crescent Beach, L.I., New York 11542
ATTN: Library
Prof. E. V. Lewis
Prof. L. W. Ward
- 1 University of Connecticut
Box U-37
Storrs, Connecticut 06268
ATTN: Dr. V. Scottrom
Hydraulic Research Laboratory
- 1 Dr. Michael E. McCormick
Naval Systems Engineering Department
U.S. Naval Academy
Annapolis, Maryland 21402
- 1 Dr. Douglas E. Humphreys
(Code 712)
Naval Coastal Systems Laboratory
Panama City, Florida 32401
- 1 Division of Engineering and Applied Sciences
324 Pierce Hall
Harvard University
Cambridge, Massachusetts 02138
ATTN: Prof. R. E. Kronauer
- 1 University of Illinois
Department of Aero. & Astro. Eng.
Urbana, Illinois 61801
ATTN: Prof. Y. K. Lin

- 2 NASA, Langley Research Center
Hampton, Virginia 23665
ATTN: D. J. Maglieri
Head, Aircraft Noise Control Section
Lucio Maestrello
- 1 Boeing Scientific Research Laboratory
P.O. Box 3981
Seattle, Washington 98124
- 1 University of California
Department of Engineering
Los Angeles, California
ATTN: Prof. W. C. Meehan, Mechanical Engineering
- 2 United Aircraft Research Laboratory
East Hartford, Connecticut 06108
ATTN: Dr. R. W. Paterson
Dr. R. K. Amiet
- 1 Stanford University
Department of Mechanical Engineering
Stanford, California 94305
ATTN: Prof. W. C. Reynolds
- 1 Dr. Thomas E. Burton
General Atomic, 15-234D
P.O. Box 81608
San Diego, California 92138
- 1 Lockheed-Georgia Company
Acoustics & Propulsion Performance Group
Department 72-47, Zone 455
Marietta, Georgia 30063
ATTN: Dr. G. Swift
- 1 G. K. Patterson
Chemical Engineering Department
University of Missouri
Rolla, Missouri 65401
- 2 Bolt Beranek and Newman
21120 Vanowen Street
Canoga Park, California 91303
ATTN: J. F. Wilby
Dr. P. H. White
- 1 Naval Underwater Systems Center
Headquarters
Newport, Rhode Island 02840
ATTN: Mr. G. Christoph

- 4 Naval Underwater System Center
New London Laboratory
New London, Connecticut 06320
ATTN: Dr. H. Schloemer
Dr. H. Bakewell
Dr. W. Strawderman
Mr. R. T. Menton
- 6 Bolt Beranek and Newman
50 Moulton Street
Cambridge, Massachusetts 02138
ATTN: Dr. D. Chase
Mr. P. Jameson
Mr. L. A. Sledjeski
Dr. N. C. Martin
Dr. K. L. Chandiramani
Library
- 1 Department of Aero Engineering
University of Southern California
Los Angeles, California 90007
ATTN: Prof. J. Laufer
Prof. R. E. Kaplan
Prof. R. Blackwelder
- 2 Johns Hopkins University
Department of Mechanics
Baltimore, Maryland 21218
ATTN: Prof. L. S. G. Kovasznay
Prof. O. Phillips
- 2 University of Michigan
Aerospace Engineering
Gas Dynamics Laboratories
North Campus
Ann Arbor, Michigan 48105
ATTN: Prof. W. W. Willmarth
Prof. V. Kibens
- 1 Professor M. V. Morkovin
Department of Mechanics and Mechanical &
Aero Engineering
Illinois Institute of Technology
Chicago, Illinois 60616
- 1 Dr. Joseph Clark
Acoustics Program
Pangborn Hall
Catholic University
Michigan Avenue
Washington, D.C. 20017
- 1 Georgia Institute of Technology
Atlanta, Georgia 30332
ATTN: Prof. A. Pierce

- 1 Applied Research Laboratory
P.O. Box 30
State College, Pennsylvania 16801
ATTN: Prof. B. R. Parkin, Director
Garfield Thomas Water Tunnel
- 1 Professor S. J. Kline
Stanford University
Stanford, California 94305
- 1 Dr. Y. Mason Chang
EPA Noise Enforcement Facility
P.O. Box 2089
Sandusky, Ohio 44870
- 1 Dr. Dale C. Houser
ORD-5411A2
Naval Ordnance Systems Command
Washington, D.C. 20360
- 1 Mr. W. J. Jobst
ORD-034B2
Naval Ordnance Systems Command
Washington, D.C. 20360
- 1 Dr. E. J. McKinney
ORD-034A
Naval Ordnance Systems Command
Washington, D.C. 20360
- 1 Dr. T. E. Peirce
ORD 0358
Naval Ordnance Systems Command
Washington, D.C. 20360
- 1 Mr. R. D. Cooper
Code 438
Office of Naval Research
Arlington, Virginia 22217
- 1 Mr. Hugh M. Fitzpatrick
Code 458
Office of Naval Research
Arlington, Virginia 22217
- 1 Mr. Anthony R. Paladino
NSHP 0372
Naval Ship Systems Command
Washington, D.C. 20360
- 1 Dr. Les Cronvich
Applied Physics Laboratory
Johns Hopkins University
8621 Georgia Avenue
Silver Spring, Maryland 20910

- 1 Dr. Steven J. Barker
MS 301-46
California Institute of Technology
Pasadena, California 91109
- 1 Professor J. M. Killen
St. Anthony Falls Hydraulic Laboratory
University of Minnesota
Minneapolis, Minnesota 55414
- 1 Professor W. P. Cunningham
Physics Department
Naval Postgraduate School
Monterey, California 93940
- 1 Professor Bruce Johnson
Naval Systems Engineering Department
U.S. Naval Academy
Annapolis, Maryland 21402
- 1 Dr. J. M. Lawther
Applied Research Laboratory
Pennsylvania State University
State College, Pennsylvania 16801
- 1 Professor T. Kowalski
Department of Mechanical and Ocean Engineering
University of Rhode Island
Kingston, Rhode Island 02881
- 1 Professor F. M. White
Department of Mechanical and Ocean Engineering
University of Rhode Island
Kingston, Rhode Island 02881
- 1 Mr. T. Lambert
Department 6151
Aerojet Electro-Systems Co.
1100 West Hollyvale
Azusa, California 90702
- 1 Dr. C. S. Wells, Jr.
Manager, Fluid Mechanics
Advanced Technology Center, Inc.
P.O. Box 6144
Dallas, Texas 75222
- 1 Mr. B. Frank Sterling, Jr.
Automation Industries, Inc.
Vitro Laboratories Division
14000 Georgia Avenue
Silver Spring, Maryland 20910
- 1 Mr. J. A. Merrill
Bendix, Electrodynamics Division
15825 Roxford Street
Sylmar, California 91342

- 1 Mr. S. Gardner
Binary Systems, Inc.
2588 Sunnyside Boulevard
Plainview, New York 11803
- 1 Dr. J. E. Barger
Bolt Beranek & Newman, Inc.
50 Moulton Street 02138
- 1 Dr. Leonard Meyerhoff
Eastern Research Group
120 Wall Street
New York, New York 10005
- 1 Mr. David Ghen
Department 413
General Dynamics, Electric Boat Division
Eastern Point Road
Groton, Connecticut 06340
- 1 Mr. Robert Gorman
Department 411
General Dynamics, Electric Boat Division
Eastern Point Road
Groton, Connecticut 06340
- 1 Mr. Robert W. Race
General Electric Ordnance Systems
1 Plastics Avenue
Pittsfield, Massachusetts 01201
- 1 Dr. Kenneth F. Loje
General Physics
Banneker Road
Columbia, Maryland 21043
- 1 Mr. John A. Pitrone
Department 461, Plant D
Defense Systems Division
Goodyear Aerospace Corp.
1210 Massillon Road
Akron, Ohio 44315
- 1 Mr. Donald A. Murphy
Building 604, MS D152
Hughes Aircraft Co.
P.O. Box 3310
Fullerton, California 92634
- 1 Dr. Joshua E. Greenspon
JG Engineering Research Assoc.
3831 Menlo Drive
Baltimore, Maryland 21215

- 1 Mr. Virgil Johnson
Hydronautics, Inc.
Pindell School Road, Howard County
Laurel, Maryland 20810
- 1 Mr. Les Bonde
Hydrospace Research Corp.
2150 Field Road
Rockville, Maryland 20850
- 1 Mr. Charles R. Campbell
Engineering Department
Arthur D. Little, Inc.
Cambridge, Massachusetts 02140
- 1 Mr. J. C. Preble
Marine Systems Center
Honeywell, Inc.
5303 Shilshole Avenue, N.W.
Seattle, Washington 98107
- 1 Mr. Stephen Sopczak
Honeywell Ordnance Division
600 Second Street, North
Hopkins, Minnesota 55343
- 1 Mr. W. S. Burdie
Department 243-061, Mail Code DF45
Autonetics Division
North American Rockwell Corp.
3370 Miraloma Avenue
Anaheim, California 92803
- 1 Mr. August F. Lehman
Oceanics, Inc.
Technical Industrial Park
Plainview, L.I., New York 11803
- 1 Mr. Bernard W. Abrahms
Ocean Systems Division
Gould, Inc.
18901 Euclid Avenue
Cleveland, Ohio 44117
- 1 Mr. Dan Suchman
Ocean Systems Division
Gould, Inc.
18901 Euclid Avenue
Cleveland, Ohio 44117
- 1 Dr. Paul F. Weyers
Paragon Systems Engineering, Inc.
1341 Rosecrans Street
San Diego, California 92106

- 1 Dr. R. L. Chapkis
Tetra Tech, Inc.
630 North Rosemead Avenue
Pasadena, California 91107
- 1 Dr. William Moyer
Tracor, Inc.
6500 Tracor Land
Austin, Texas 78721
- 1 Mr. S. Steven Kushner
Westinghouse Ordnance Department
1405 Parker Road
Box 2157, MS 2030
Baltimore, Maryland 21203
- 1 Mr. H. H. Vogel
Presearch, Inc.
8720 Georgia Avenue
Silver Spring, Maryland 20910